Biophysical Insights into the Role of Amyloid-Beta Misfolding in Alzheimer's Disease Pathogenesis

by

Samuel A. Kotler

A dissertation submitted in partial fulfillment
of the requirements for the degree of
Doctor of Philosophy
(Biophysics)
in the University of Michigan
2015

Doctoral Committee:

Professor Ayyalusamy Ramamoorthy, Chair
Professor Carol A. Fierke
Professor Nicholas Kotov
Professor Sarah L. Veatch

Acknowledgements

First and foremost, I would like to thank my adviser, Professor Ayyalusamy Ramamoorthy, for his dedication and support throughout my time at the University of Michigan. I am incredibly lucky to have had the guidance and mentorship while working in his group, and it is because of these experiences that I developed into the researcher I am today. I appreciate his trust in me at a very early point as a PhD student, allowing me the freedom to pursue the work I enjoyed the most.

I would also like to acknowledge my committee Professors Carol Fierke, Nicolas Kotov, and Sarah Veatch. Carol was willing step in as a committee member following the untimely move of another. Additionally, from our very first interaction she showed great interest in my work and provided meaningful advice. Nick challenged me to ask the questions that brought my work to a broader focus. Last, but not least, of my committee members, Sarah was one of the first professors I interacted with in the Biophysics program, allowed me to rotate in her lab, taught me in class, and was a mentor to me throughout my time as a PhD Student.

I would additionally like to thank past and present members of the Ramamoorthy group that have provided support and plentiful insights throughout my time at UM. Special thanks to the RAMyloid team: Dr. Patrick Walsh, Amit Pithadia, Kyle Korshavn, Dr. Jeffrey Brender, Dr. Janarthanan Krishnamoorthy, Dr. Anirban Bhunia, and Jennifer Chen. Additional thanks to Dr. Kamal Mroue, Dr. Kazutoshi, Dr. Dongkuk Lee, Dr. Anirban, and Dr. Manoj Pandey who have in particular contributed to my success.

Finally, I would like to thank my family and friends for their unconditional support and inspiration. I feel incredibly grateful to my fellow Biophysics graduate students, particularly Carter Swanson and David Rowland who have been there with me from the start. I also want to particularly thank Dr. Ricardo Capone for his continued encouragement, mentorship, and friendship without which I would not be where I am today. I cannot express enough gratitude towards my parents, brother, and sister who will always be my number one fans. And of course, I want to give a very special acknowledgement to the person who supports me on a daily basis, my girlfriend, Anna. Thank you for everything.

Table of Contents

List of Figures

List of Appendices

Abstract

Amyloids are protein aggregates that build up as plaques in various tissues in the body and are associated with a number of diseases. Of the amyloidoses, Alzheimer's disease (AD) is the most known and socially distressing. Amyloid-beta (Abeta) is the amyloidogenic protein associated with AD and is implicated in the etiology of the disease. Abeta aggregation is highly heterogeneuos, giving rise to a number of possible aggregation pathways and intermediate oligomeric structures. The mechanism of Abeta aggregation was studied here in the presence and absence of a model cell membranes employing fluorescence spectrosopy, light scattering, atomic force microscopy, and NMR spectroscopy.

First, Abeta aggregation is investigated in the presence of a lipid bilayer, exploring the particular role of lipid composition on the mechanism of membrane disruption. It was shown that membrane disruption by Abeta occurs by a two-step process: (i) intial formation of ion-selective pores followed by (ii) non-specific fragmentation of the lipid membrane during amyloid fiber formation. Moreover, the presence of gangliosides enhances pore formation and is necessary for fiber-dependent membrane fragmentation.

Next, magic angle spinning (MAS) NMR is used to gain structural insights on an Abeta oligomer, providing atomic-level characterization on a non-fibrillar product of Abeta. Importantly, it is demonstrated that MAS NMR and ^{1}H-^{1}H dipolar interactions can be used as a spectral filter to detect Abeta oligomers without a purification procedure. In comparison to other solid-state NMR techniques, the experiment is extraordinarily selective and sensitive, as it can resolve spectra on a small population of oligomers (7% of the total Abeta concentration). Using

this method, it was shown that a stable, primarily disordered Abeta oligomer forms and coexists with amyloid fibers.

Finally, a real-time 2D NMR method is implemented to study the mechanism of Abeta fiber elongation. It is demonstrated that monomeric Abeta undergoes a conformational conversion after binding to the fiber surface to complete the elongation step, with the strongest interaction occurring in the central region of the peptide (residues Phe19- Glu22). To our knowledge, this is the first high-resolution account of the fiber elongation process and provides residue-specific details of amyloid fiber polymorphism.

Chapter 1: Introduction

Portions of this chapter have been adapted from the following publication:

Kotler, S.A., Walsh, P., Brender, J.R., and Ramamoorthy, A. (2014) Differences between amyloid-β aggregation in solution and on the membrane: elucidating mechanistic insights into Alzheimer's disease. *Chemical Society Reviews*. **43**, 6692-6700.

1.1 Introduction

Amyloid deposits characterize more than twenty different clinical syndromes, each of which is associated with a distinct amyloid-forming protein. Neurodegenerative diseases such as Alzheimer's, Parkinson's, and Huntington's diseases, in addition to localized diseases such as Type II Diabetes, are associated with the aggregation and misfolding of amyloidogenic peptides/proteins. Of these amyloid-related diseases, Alzheimer's disease (AD) is the most known, affecting 5.2 million people in the United States and more than 24 million people worldwide (1). AD is clinically characterized by the presence of intracellular neurofibrillary tangles and extracellular senile plaques (2). The plaques consist of insoluble amyloid deposits composed primarily of aggregates of amyloid-β (Aβ) in their fibril form. The Aβ peptide is produced through proteolytic cleavage of the amyloid precursor protein (APP) by the β- and γ-secretases (3). The predominant Aβ species formed are the Aβ40 and Aβ42 peptides (consisting of 40 and 42 residues, respectively); with the Aβ42 variant being an indicator of a progressive AD state (Fig. 1.1) (4). The accumulation of Aβ40 and Aβ42 into long, unbranched fibrils is a hallmark of the disease, as is the loss of neurons due to cell death in parallel with the Aβ aggregation process (2, 5). Amyloid fibrils of Aβ40 and Aβ42 form a parallel, in-register cross β-

sheet structure that binds to fibril-specific dyes such as congo red and thioflavin-T (ThT) (6). Prior to fibril formation, Aβ forms a myriad of structures in the monomeric and oligomeric states, all of which result in similar fibril structures (3). Neurotoxicity by Aβ is convoluted as it is unknown which misfolded species causes cell death, in addition to the mechanism by which a particular misfolded state causes toxicity. This data has been correlated with brain samples from patients with and without AD, and, to this day, the Aβ fibrils define and confirm the diagnosis of AD patients' post-mortem (4).

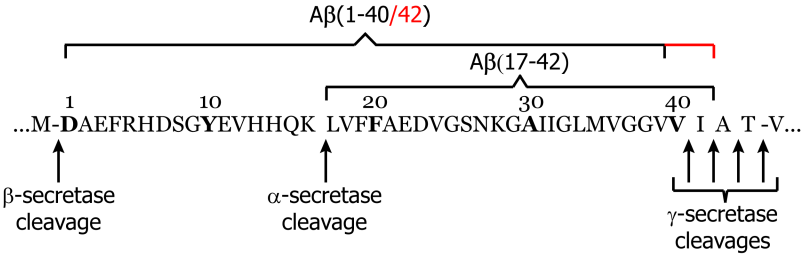

Figure 1.1 Aβ peptides derive from the proteolytic cleavage of the amyloid precursor protein (APP). The β- and γ-secretases cleave APP to form the full length, amyloidogenic peptide Aβ peptide that ranges in length from 38-43 residues. When APP is processed by α-secretase, the non-amyloidogenic fragment Aβ(17-42) is formed (also known as the p3 fragment).

Early AD research pointed to Aβ fibrils specifically as the neurotoxic agent leading to cellular death, memory loss, and other AD characteristics (7). Over the last two decades, further investigation has suggested that the fully-matured fibrils are no longer considered to be the main toxic agent; rather, oligomeric, prefibrillar species of the Aβ peptide have been shown to be most damaging to neuronal cells (3, 5, 8–10). There are several hypotheses regarding the mode of Aβ toxicity and they include the generation of reactive oxygen species, interaction with cell receptors, interactions with metals and direct disruption of cellular membranes (Fig. 1.2) (5). One widely accepted theory, called the amyloid hypothesis, deals with the notion that misfolded

intermediate states are responsible for cell death (3). Therefore, it is important to establish the relationship between misfolded entities, their structural properties, and how they confer toxicity.

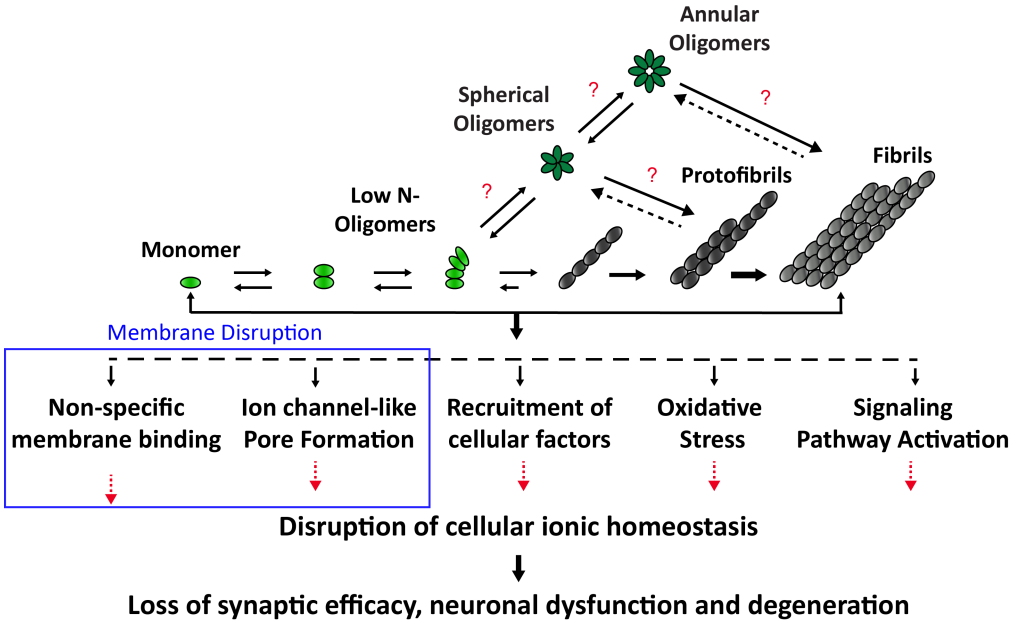

Figure 1.2 The amyloid hypothesis for Alzheimer's disease.
The aggregation of amyloid-β is highly diverse and poorly understood. Mounting evidence points to oligomers as being the most toxic agent in Alzheimer's disease; however, intermediate structures are transient and heterogeneous. Additionally, the mechanism by which Aβ can be neurotoxic has not been fully elucidated. One prevailing hypothesis suggests that Aβ can be toxic through a membrane disruption mechanism.

1.2 Structurally dissimilar Aβ oligomers give rise to varied neuronal toxicity

While the toxicity of Aβ is under constant debate, the amyloid hypothesis has been supported by bodies of work suggesting that amyloid oligomers are the toxic amyloid species (11). The toxicity of soluble amyloid oligomers is not only relevant to AD, but to other amyloid diseases as well such as Parkinson's disease and Type-II Diabetes where α-synuclein and human islet amyloid polypeptide (hIAPP) are indicated as the aggregative proteins, respectively (5, 12). In the case of Aβ, it is known that amyloid oligomers are toxic in vitro (13), with further evidence identifying oligomers as the culprit for in vivo toxicity (14). The problem herein arises

due to the fact that oligomers ranging in size and structural morphology have exhibited cytotoxicity (15).

A wealth of structural data exists for the relatively benign fibrils of Aβ (6); however, intermediate structures such as structured monomers and oligomers have remained relatively unexplored, largely due to their transient nature. In this regard, the inability to crystallize and/or trap a pure (single state) sample has presented much of the difficulty in performing structural studies of oligomeric species. Relatively low-resolution methods, such as AFM, hydrogen-deuterium exchange mass spectrometry, and circular dichroism (CD) have shown the wide size distribution of oligomers and variance in secondary structure. To further complicate matters, increasing the concentration to levels that are more amenable to atomic-resolution structural experiments can affect the aggregation time, decreasing the longevity of the oligomeric sample. Consequently, the sensitivity of aggregation results from a multitude of factors generating heterogeneous samples and hampering structural studies by techniques like nuclear magnetic resonance (NMR) and X-ray crystallography.

The larger oligomers of Aβ have been mostly described as spherical, although studies have shown that circular, annular oligomers are producible in vitro (16, 17). One interesting aspect of Aβ oligomers and amyloid oligomers in general, is their ability to bind a common antibody regardless of structure. This ability to bind the A11 antibody indicates that amyloid oligomers across diseases and protein sequences share a common structure (16). This common β-sheet-containing structure is fascinating, especially given structural evidence that Aβ40 forms a 310 helix in solution (Fig. 2a), meaning a helix-to-β-sheet transition may occur (18). That being said, secondary structure-dependent toxicity has been the source of some debate. While most of the oligomers studied to date have contained β-sheet secondary structure, for relatively small

oligomers of Aβ42, it was determined that hydrophobic exposure and not the presence of β-sheets are required for toxicity. The study also found that aggregate number is also not necessarily linked to toxicity; two similar sized globular oligomers were characterized and the more-hydrophobic exposed oligomer was toxic (19).

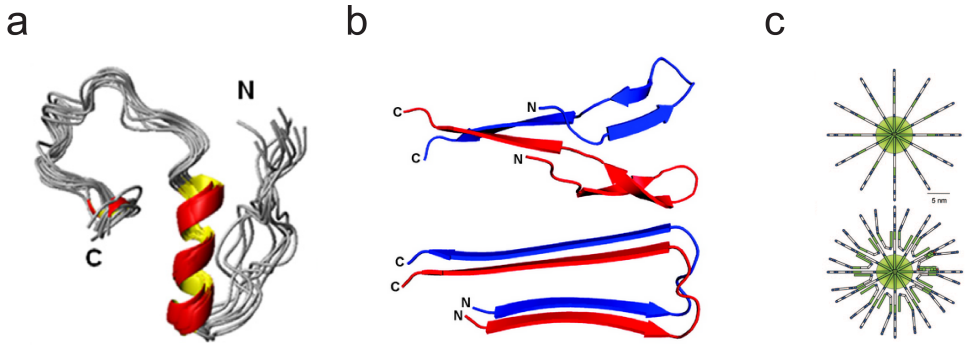

Figure 1.3 Various structures of Aβ in solution and detergents characterized by NMR.
(a) Aβ40 as a partially folded structure in the presence of 50 mM NaCl, with residues 13 to 23 forming a 310 helix.18 (b) Solution NMR structure of 0.05% SDS-stabilized pre-globulomer of Aβ42 (top) compared with the basic fold of the fibrils of Aβ42 (bottom). Adapted with permission from Yu et al.21 Copyright 2009 American Chemical Society. (c) Structural schematic of β-balls formed at low pH in the absence (top) and presence (bottom) of DSS. These structures both show a pinwheel, or micelle-like, arrangement of monomers. Reprinted with permission from Laurents et al. 2005. Copyright 2005 Journal of Biological Chemistry.20

Some structural studies have utilized detergents or small molecules to stabilize both large (20) and small (21) oligomeric states with some success while others have utilized the freeze-trapping of purified oligomers (9). Very large oligomers formed at low pH, described as amyloid "β-balls" and having a molecular weight of 764 kDa, have been studied at low-resolution. These very large assemblies can also be stabilized by DSS (4,4-dimethyl-4-silapentane-1-sulfonic acid), and are hypothesized to have a pin-wheel-like structure, with monomers protruding radially outward (Fig. 2c) (20). In the case of freeze-trapped large oligomers of Aβ40, structural studies by solid state NMR have identified fibril-like contacts (9). These large spherical oligomers contain primarily β-sheet secondary structure and are toxic to cultured neurons. Smaller Aβ42 oligomers, thought to be pentamers, show a more loose arrangement with turns and C-termini

contained in the center of the oligomer (10). Polymerization of these "disk-shaped" oligomers into fibrils is thought to occur by association and lateral extension of parallel β-strands into fibrils. These pentamers are also toxic to cultured mouse neurons, even in the absence of β-sheet secondary structure. The collective theme associated with the three aforementioned structures is the idea of a pinwheel, or micelle-like, structure which may confirm the notion that oligomers of various size and sequence share a common structural element.

Smaller oligomers, coined as pre-globulomers and globulomers, of Aβ42 described by Yu et al show similar molecular contacts to amyloid fibers of Aβ (Fig. 2b) (21). The pre-globulomers (16 kDa) and globulomers (64 kDa) were stabilized by 0.05% sodium dodecyl sulphate (SDS) and studied by solution NMR. As with larger freeze trapped oligomers of Aβ40, the identification of these fibril-like structures provides a basis for the conversion of oligomers to fibrils, but do not directly explain the ability of Aβ to permeabilize cell membranes.

Overall, high-resolution reports of fibril-like contacts for spherical oligomers of Aβ40 have shown parallel β-sheets (9) while oligomers of Aβ42 demonstrated a lack of β-sheet secondary structure (10), highlighting the important difference observed between the structure and toxicity of these Aβ alloforms. Others have pointed to oligomers containing anti-parallel β-sheets for the formation of pores and thus, the permeabilization of cell membranes (22).

Annular oligomers, or annular protofibrils, are 8-20 nm in diameter and contain, as with spherical oligomers, a high β-sheet secondary structure (16). Despite the β-sheet content, circular oligomers are quite different from their spherical counterparts. It has been shown that these annular oligomers may share a common structure with β-barrel pores, such as α-hemolysin, through the binding of an anti-annular protofibril antibody to assembled α-hemolysin (16). Despite having a preformed pore-like structure, these circular oligomers do not permeabilize

membranes, but rather convert to spherical oligomers in the presence of lipids. Regardless of their inability to permeabilize membranes, annular protofibrils point to the possibility of a β-barrel pore as the Aβ pore structure.

The relationship between structure and cellular toxicity has been of primary focus in recent amyloid research. Given the number of reportedly different oligomeric Aβ species, relating these parameters could provide intuition into how we might go about preventing unfavorable folds from occurring. Despite the propensity of Aβ to form fibril-like intermediates early and late in its aggregation pathway, existing evidence suggests that the fold of toxic oligomers may differ considerably from that of the Aβ fibril (15, 23). As a result of the variance in secondary structure between different oligomer preparations, Aβ toxicity need not derive from a 'single' toxic species. In a recent study, Lashuel and co-workers argued that Aβ toxicity results from an "ongoing polymerization process" by demonstrating that a heterogeneous mixture of monomers and protofibrils were prone to heightened aggregation and, in turn, cytotoxicity (24). Neurotoxicity occurring by such a mechanism would only present greater difficulties in seeking therapeutic measures for alleviating AD symptoms, and attributes greater stress to understanding misfolding pathways as opposed to identifying individual toxic structures.

While it is important to understand the structural link between intermediates and fibrils, their ultimate mode of action should be considered. Therefore, it is of utmost importance to gain structural and functional information on intermediates at their site of action, namely the membrane. Solid state NMR has proven to be an effective tool for the characterization of Aβ oligomer structures in the absence of the membrane. This technique has been a cornerstone of lipid biophysics as well, allowing researchers to effectively determine the integrity and dynamics of the lipid bilayer. With solid state NMR having been recently used to solve the structures and

dynamics of several membrane proteins (25) and membrane disrupting antimicrobial peptides (26), it stands to reason that this technique will be on the forefront of structural determination of Aβ in the membrane environment.

1.3 The role of membrane composition and disruption in AD pathogenesis

A number of studies have identified various possible mechanisms for cytotoxicity mediated by Aβ, and a prominent focus in AD pathology has centered on Aβ's ability to disrupt membranes (5). In order to be cytotoxic via membrane disruption, Aβ aggregates must interact with the cellular surface by either a receptor or the lipid membrane. The mechanism of Aβ-membrane interactions has not been fully elucidated; however, its interaction with the membrane is likely to affect the structure and properties of any type of aggregate. Dysregulation of ionic homeostasis, particularly of Ca2+, has been a consistent pathology in AD; thus, understanding the molecular mechanics by which Aβ induces ionic flux has become crucial to AD pathology (27). The cellular membrane in live cells is exceedingly complex, involving many variables that are difficult to isolate and control. Consequently, studying structural transitions of Aβ in the presence of membranes (with varying composition) and the ionic flux across a cellular membrane that results due to specific Aβ-membrane interactions has been extremely challenging.

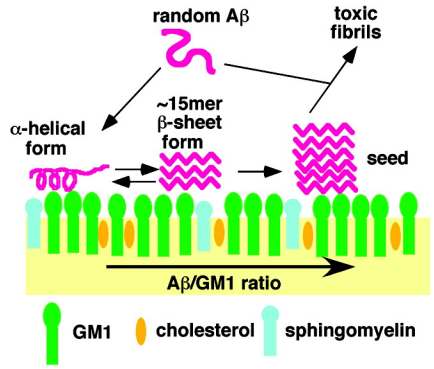

Figure 1.4 Model of GM1 ganglioside-clusters leading to the formation of toxic Aβ species.

Studies have found that low Aβ:GM1 ratios yield an α-helical Aβ structure, while an increasing Aβ:GM1 ratio produces fibrils. Reprinted with permission from Ikeda et al. 2011. Copyright 2011 American Chemical Society (33).

1.4 Ganglioside-containing membranes influence structural changes during Aβ aggregation

Although obtaining structural models of Aβ oligomers is paramount to understanding the pathology of AD, the presence of membranes has been shown to strongly influence the Aβ aggregation pathway. While a number of studies have reported on the Aβ-membrane interaction, a great body of evidence points to gangliosides playing a significant role in altering the aggregation pathway of Aβ (28, 29). Gangliosides are glycospingolipids that contain a sialic acid headgroup moiety and play a substantial role in cell signaling and memory function. Early work identified Aβ fibrils tightly bound to monosialoganglioside (GM1), generating a conformationally distinct Aβ species (30). Since this work, a series of in vitro and in vivo studies demonstrated GM1 strongly influences the secondary structure of Aβ in the early and late stages of aggregation (31). Initial biophysical characterization demonstrated the pivotal role the sialic acid played in inducing such structural transitions (32). Work along this direction from the Matsuzaki group showed structural changes of Aβ upon interaction with GM1 was dependent upon the Aβ:GM1 ratio—for a low Aβ:GM1 ratio Aβ assumes an α-helix conformation, while at a high Aβ:GM1 ratio fibril formation ensues (Fig. 3) (29, 33). A great body of evidence from the Matsuzaki group has demonstrated Aβ amyloidogenicity can be altered in the presence of GM1-containing membranes, with this effect being amplified by introducing Aβ to a lipid raft-like membrane mimetic. Cell viability assays showed that co-incubation of Aβ40 with GM1 in a lipid raft-like environment generated toxic amyloid species. Furthermore, concurrent measurements of the accumulation of Aβ and oligomer formation at the cell membrane were visualized with TIRF microscopy, revealing membrane-mediated aggregation affects fibril morphology (34).

The enhanced binding of Aβ to gangliosides is largely dependent upon the sialic acid of the headgroup moiety. Yet, McLaurin and Chakrabartty demonstrated that neither the ceramide nor the sialic acid alone could induce a partial helical structure; rather, the structural transition brought about by gangliosides is dependent upon the association of the sialic acid with the carbohydrate backbone (32). Recently, an NMR study came to a similar conclusion using the paramagnetic relaxation enhancement (PRE) effect to identify Aβ binding to GM1 at the sugar-ceramide junction (35). In a related study, Williamson et al employed the use of chemical shift perturbations of uniformly ^{15}N-labeled Aβ40 upon titration of GM1 and asialo-GM1 micelles as monitored by HSQC (heteronuclear single-quantum coherence) and revealed: i) the presence of the sialic acid in the ganglioside headgroup enhanced Aβ-GM1 binding, ii) Aβ binding to GM1 was N-terminally driven, and iii) Aβ association is localized to His-13 and Leu-17 (36). In accordance with these data, a separate NMR study using ^{1}H-^{15}N TROSY and TROSY-based saturation transfer experiments, it was found that Aβ assumes a partial helical structure with an "up and down topological mode" when bound to GM1 micelles (35). A structure was not determined by this study from Utsumi et al; however, it was found through backbone chemical shifts that the regions of Aβ bound to GM1 micelles assumes discontinuous α-helices between residues His14-Val24 and Ile31-Val26 (other regions of the peptide being unstructured).

The studies from Williamson et al and Utsumi et al seem to generate conflicting results of Aβ binding to gangliosides being N- or C-terminally driven. Yet, one can imagine a multi-step process involving initial electrostatic interactions with the N-terminus and hydrophobic interactions driving binding and/or insertion of the C-terminus into the GM1-containing membrane. The early biophysical characterization of the Aβ-GM1 interaction demonstrating the subtle dependence on the peptide:lipid ratio was corroborated by the more recent NMR studies.

Collectively, these data provide a better understanding for the production of structurally dissimilar Aβ aggregation states and heterogeneity in the aggregation pathway; the central dogma of the amyloid problem. It is well known that Aβ membrane binding is amplified by the presence of negatively charged lipid headgroups. Nonetheless, answering questions as to what makes for favorable binding to gangliosides and how gangliosides generate toxic amyloid species remain inadequate in the broader scope of AD pathology. While there is still much to be learned about the Aβ-ganglioside interaction, recent progress has been made in understanding how gangliosides might play a role in the mechanism of Aβ toxicity.

1.5 Gangliosides mediate a two-step mechanism of amyloid-β membrane disruption

Studying the interactions between Aβ and cellular membranes has proven to be of great importance, yet more insight must be gained by understanding the mechanism by which these oligomers can be toxic to cells. Aβ generates a multifactorial response in neurons, making the study of Aβ's cytotoxicity difficult to pinpoint. While the exact mechanism of Aβ neuronal toxicity remains elusive, one of the long-standing pathologies is believed to arise from increased levels of cytosolic Ca2+ resulting from plasma membrane disruption (37). A number of in vitro studies over the last two decades demonstrated that ionic dyshomestasis can be caused by Aβ's ability to form ion channel-like pores: an annular oligomer structure that allows ions to permeate the membrane through a pore of a hydrophilic interior and hydrophobic exterior (27). The resulting unregulated influx of Ca2+ is a result of the general properties of Aβ pores being cation selective and capable of being blockaded by Zn2+, suggesting these pores adopt a specific structure (37–39). Yet, there is little information on the structure adopted by Aβ upon its insertion to the membrane. Studies have suggested that pore structures contain a β-sheet rich conformation which is consistent with the current available structural data of Aβ; particularly the

common U-shaped motif found in amyloid structures (40). The concept of an explicit pore structure is further supported from a study by Capone et al, which demonstrated Aβ ion channels could be modulated by non-natural amino acid substitutions and emphasized the necessity of secondary structure for such channels to form (41). In a related study from Lal and colleagues, Aβ with an all D-amino acid sequence retains strikingly similar features known for the all L-amino acids Aβ, demonstrating that chirality had no bearing on Aβ channel-like activity (42). The results using the all D-amino acids Aβ peptide are quite intriguing; however, in vivo toxicity measurements would provide a more definitive answer as to whether stereospecific, non-stereospecific, or both mechanisms are involved in membrane perturbations. Nevertheless, both neurons and mitochondria are highly sensitive to perturbations in ionic strength, and a small perturbation in intracellular calcium levels caused by unregulated Aβ channel activity can trigger an apoptotic cascade.

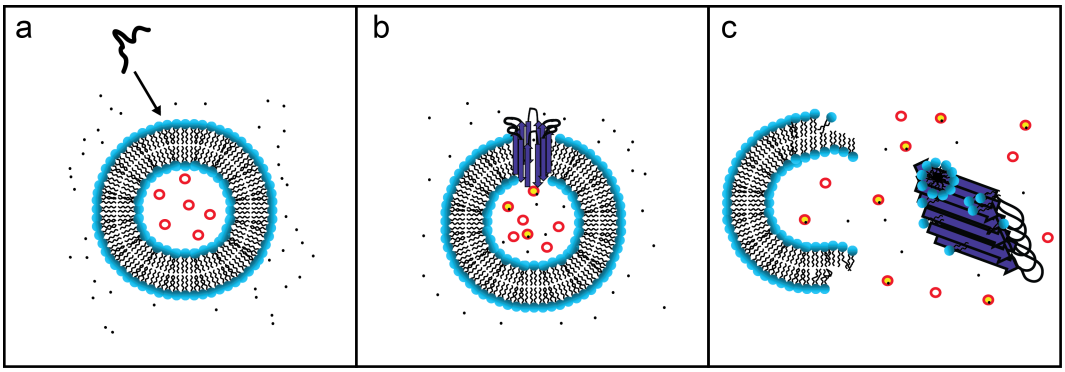

Figure 1.5 A two-step mechanism of membrane disruption by Aβ40.
Upon addition of Aβ to a membrane solution (a), it is capable of binding to the membrane and forming ion channel-like pores (b). Appearance of Aβ pores is increased by the presence of gangliosides in the membrane composition. Furthermore, gangliosides mediate a second step of membrane disruption, a fiber-dependent step, which acts via a detergent-like mechanism to fragment the lipid bilayer (c).

The amyloid channel hypothesis provides much insight into the membrane disruption mechanism by Aβ and other amyloid peptides; however, the mechanism by which Aβ stimulates ionic dyshomeostasis has not been fully elucidated. A multivariate analysis of Aβ cytotoxicity

found a negative correlation with both the particular cross-β sheet structure of amyloid fibers as well as the overall β-sheet content, contrary to the predicted models of Aβ pore structures (43). Moreover, spherical aggregates of Aβ have repeatedly shown to exhibit cytotoxicity (44, 45), and it is difficult to fathom how such structural polymorphs could form an Aβ ion channel.

Recently, Sciacca et al demonstrated that membrane disruption by Aβ involves a two-step mechanism: (i) Aβ oligomers bind to the membrane to form ion permeable pores and (ii) the process of Aβ fibrillization causes membrane fragmentation via a detergent-like mechanism (Fig. 4) (46). The first phase of this proposed two-step mechanism (Fig. 4b) shares many of the qualities observed for the previously described Aβ channel structures; namely, cation selectively and the ability to be blocked by Zn2+. The second step was found to be correlated with the formation of Aβ fibrils as revealed by leakage of the dye 6-carboxyfluorescein from large unilamellar vesicles (LUVs) and time course ThT measurements. Further examination of the fiber-dependent form of membrane disruption by ^{31}P NMR and a lipid sedimentation assay led to the conclusion that this mechanism acted in a detergent-like manner. Unlike the Aβ pores, the second phase of membrane disruption displayed neither charge nor size selectively, lending support to the loss of the integrity of the membrane (Fig. 4c). Interestingly, completion of fibril polymerization halted progression of further membrane fragmentation, and, perhaps more intriguing, this phase of membrane disruption was entirely dependent upon gangliosides being part of the membrane composition. Given the overwhelming evidence for the effect of ganglioside-containing membranes on Aβ aggregation, the finding of a relationship between aggregation and membrane disruption is a step forward in bridging ideals for further elucidation of a mechanism. In a similar train of thought, fiber-dependent membrane disruption can be

correlated with the results previously discussed from Lashuel that ongoing polymerization was a key factor in cytotoxicity.

It should be noted that both the pore and fiber-dependent mechanisms are not strictly characteristic of Aβ. For example, IAPP displays a similar biphasic effect in membrane disruption, and our group demonstrated that the fiber-dependent membrane permeabilization could be prevented by insulin (47) and both mechanisms could be modulated by the presence of PE lipids in the membrane composition (48). Furthermore, α-synuclein has been implicated as a membrane disrupting protein by pore formation and membrane fragmentation, in addition to other amyloidogenic proteins (38, 49). While there is an abundance of existing biophysical and biochemical data to support the amyloid hypothesis for Aβ and other amyloids, much more characterization needs to be done; namely, in the area of the therapeutic prevention of membrane disruption and further elucidation in the structure of misfolded intermediate states.

1.6 Preventing membrane disruption by Aβ

Small molecule compounds blocking Aβ channel formation and other forms of membrane disruption have the potential to alleviate Aβ-induced cytotoxicity. Current amyloid inhibitors target Aβ oligomers and fibrils outside the membrane (50, 51). For Aβ structures formed on and in the membrane this can be problematic as the small molecule EGCG has been shown to be less effective at the membrane surface (52). Given Aβ's reactivity with the membrane, it is greatly important that small inhibitors such as EGCG have equal or superior efficacy at the peptide-membrane interface. Inhibitors of channel formation would therefore seem to be a very attractive target for stopping Aβ cytotoxicity. Such small molecules designed by Arispe and co-workers protected against the neurotoxic effect of Aβ and blocked ion conductance activity in model membranes (53). Unfortunately, the number of known channel

inhibitors of Aβ is currently very limited. Since the Aβ channel is formed by the oligomerization of Aβ, aggregation inhibitors are likely to influence Aβ channel formation. However, many aggregation inhibitors are specific to the fibrillar form of Aβ and therefore may not have activity against the specific oligomerization process that creates Aβ channels. Thus, an attractive approach would be to seek a set(s) of molecules to synergistically prevent all possible modes of membrane disruption by screening known inhibitors of Aβ aggregation as inhibitors of Aβ membrane disruption. If pore and oligomer formation are at least partially independent, as our previous data indicates, the elimination of either process alone will be insufficient to stop Aβ toxicity. However, the addition of both pore blockers and aggregation inhibitors simultaneously may eliminate the cellular dysfunction caused by Aβ. Given the common pathology associated with many amyloidogenic proteins, this avenue of research seems promising in light of the amyloid hypothesis.

1.7 Obtaining high-resolution structures of membrane-bound Aβ species

Due to the inability to crystallize stable and homogeneous Aβ preparations on membranes, the use of computational techniques has become the principal mode to model Aβ structure in membranes (27, 40). Yet, the details of Aβ-membrane interactions and the membrane disruption process are not merely of theoretical importance, but have great practical implications for the prevention of membrane damage by amyloidosis. Membrane damage that is primarily mediated by discrete ion channels can be alleviated by channel blockers designed specifically to plug the channels formed by toxic amyloid species. Such small molecules were designed with the intention of complementary binding to distinct Aβ channel structures, thereby reducing cytotoxic effects and strengthening the amyloid channel hypothesis (53). However, prevention of a non-specific mechanism involving membrane fragmentation requires a different approach

aimed at blocking the interaction of protofibrillar Aβ with the membrane. To accomplish this it is necessary to have some understanding of the interactions involved in binding of Aβ to the membrane in fibrillar and prefibrillar conformations and some idea of the conformation of the membrane-bound peptide in a given aggregation state. Unfortunately, while many of the mechanistic details of Aβ amyloid formation in solution remain to be determined, experimental evidence of structural polymorphisms involved in amyloid formation on or in a membrane beyond the resolution of CD, ThT fluorescence, and other biophysical measurements are almost completely unknown.

Currently, the only membrane bound models of Aβ that exist are high-resolution structures of Aβ monomers bound to detergent micelles and computer simulations of channels or oligomers constructed from fragments of the Aβ fiber (27, 40, 54). The computer simulations of Aβ channels have been invaluable in identifying molecular features of potential Aβ pore structures, yet more structural data is necessary to further refine computational models and to collectively understand all forms of membrane disruption. It is apparent that membranes have a two-fold effect on Aβ: (i) membranes can greatly accelerate the rate of fibrillization and (ii) Aβ can directly disrupt plasma and possibly organelle membranes. The cell membrane therefore contributes to Aβ toxicity as both a site for the accumulation/nucleation of toxic oligomers and as a target for their cytotoxic effect. Consequently, it is imperative to better understand how environmental factors within the cell membrane (such as the lipid composition) contribute to structural polymorphisms of Aβ oligomers. Such data will help us understand both how membrane disruption occurs and possibly if certain cell types are more sensitive to Aβ toxicity due to an altered lipid composition, generating a more toxic conformation.

1.8 Experimental methods for studying the process of amyloid fibrillization and oligomerization

Characterizing the kinetics of amyloid formation as well as the structural transitions that occur therein is experimentally challenging. The primary challenge results from the fact that Aβ aggregation is a highly heterogeneous process sensitive to a variety conditions; e.g. salt concentration, pH, and temperature. Small changes can result in the kinetics of aggregation for seemingly similar samples by 1-2 orders of magnitude (Fig. 1.6A), and comparable observations are found with other measurements such as cytotoxicity (55). One of the most common methods to investigate Aβ aggregation, and any amyloid forming protein in general, is through the use of the amyloid-specific dye thioflavin T (ThT) (Fig. 1.6A). ThT specifically binds to the cross β-sheet structure of the long, linear fibrils and may provide indirect evidence on the conversion of monomers to oligomers and oligomers to fibrils (56). The ThT fluorescence response to fibril formation typically displays sigmoidal growth kinetics, resulting from the nucleated self-assembly reactions. While the ThT-based fluorescence assay is robust for most amyloidogenic proteins, it suffers from several drawbacks that may convolute the fuller picture of Aβ aggregation, and amyloid aggregation broadly (57). Firstly, because the dye is amyloid-specific, the ThT assay provides little to no information on intermediate species that may nucleate fibril formation; a necessary process for fibrillization (56). Furthermore, ThT may compete with the same binding on the fiber structure of a small molecule inhibitor of aggregation, potentially giving rise to a false positive for fiber inhibition (58). Thus, complementary biophysical approaches are necessary, and correspondingly used in throughout this dissertation, to enable a comprehensive of Aβ aggregation under particular conditions.

A suite of biophysical techniques has been developed and is still being developed to dissect the Aβ aggregation. CD spectroscopy is routinely used to provide information about secondary structure of a particular aggregate and/or the time-course nature of the structural transition occurring under aggregation conditions (56, 57, 59). CD is capable of distinguishing monomeric species from aggregated species, in general (Fig. 1.6C); however, still suffers from a similar shortcoming of the ThT assay in that CD cannot distinguish between an oligomer with β-sheet structural elements and a fibers or an oligomer lacking secondary structure and a monomer; the latter being true only for amyloid-forming proteins that intrinsically disordered in monomeric form. Light scattering methods can be used to distinguish aggregate size and may be done so in time-course or single time point fashion (60). However, light scattering methods fall short when the aggregate sizes are highly heterogeneous or too large, making such an approach limited in its utility as well. Separation-based approaches such as size exclusion chromatography (SEC) or gel electrophoresis are often employed as well (55, 61). The disadvantage with such methods stems from their capacity to break apart loosely associated oligomeric species and underestimates their actual size (61). As a result of the possible artifacts inherent to the techniques previously mentioned, microscopy methods, particularly atomic force microscopy (AFM) and electron microscopy (EM), have been invaluable to complement optical spectroscopic and separation-based techniques (62–64). EM has been especially useful to differentiate fibril polymorphs that may result from different aggregation conditions (65, 66), while AFM has been a versatile tool for in situ imaging of aggregation (61–63). Both EM and AFM have thus far, however, been unable to achieve the level of resolution likely necessary to fully elucidate amyloid aggregation. It should be mentioned that analytical ultracentrifugation (AUC), X-ray diffraction, and small-angle X-ray scattering (SAXS) may provide the level resolution desired, yet does not maintain

the temporal resolution required to perform kinetic studies of amyloid formation. Finally, NMR is another of the many techniques that are highly valuable to the study of amyloid aggregation while also having a number of advantages and some disadvantages that will be discussed in further detail in subsequent section (Fig 1.6B and 1.6D).

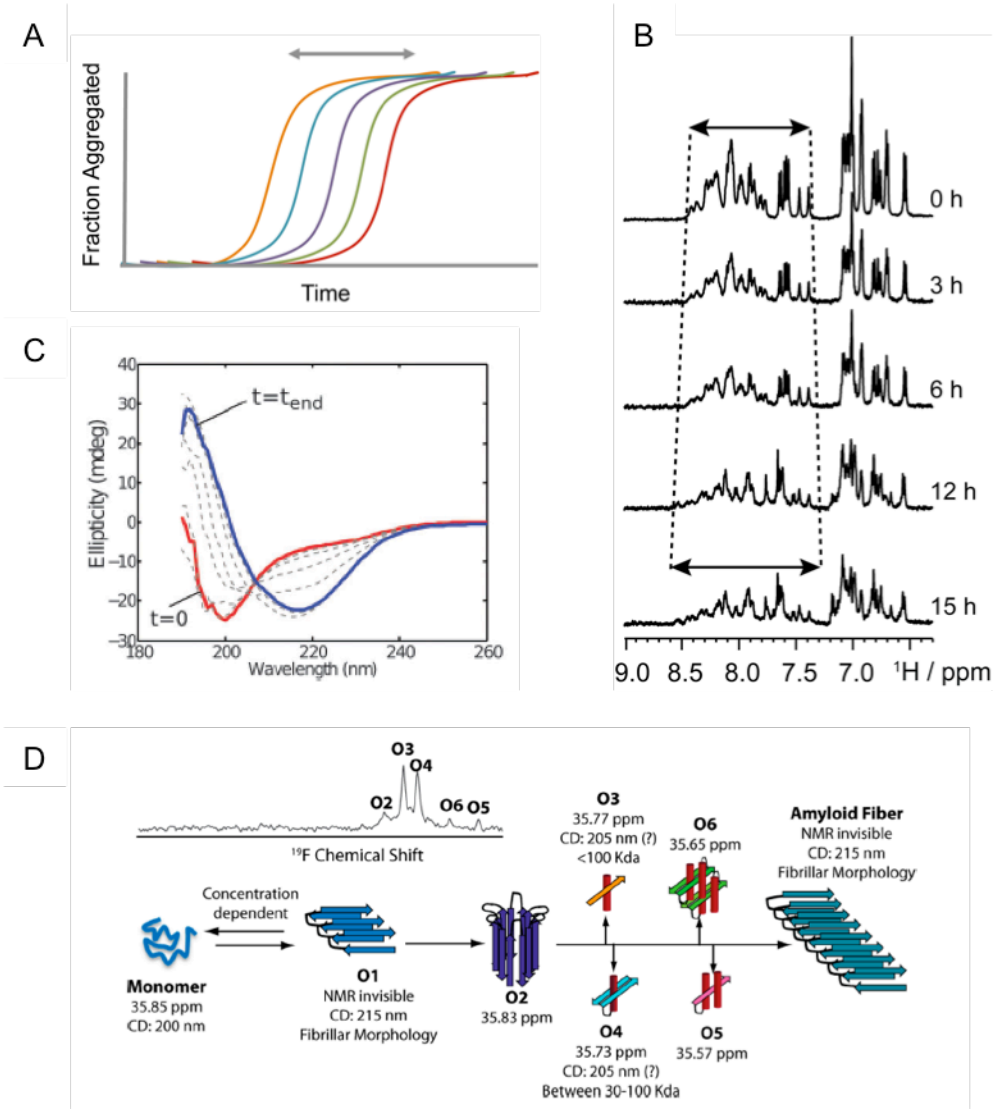

Figure 1.6 Measuring the process of amyloid aggregation can be probed by many biophysical methods.
(A) Thioflavin T is an amyloid-specific and is the most common way to probe amyloid formation. (B) Real-time NMR measurements can provide insight into the loss of monomer to higher order aggregates and gain of secondary structure through loss of intensity and increased spectral dispersion (indicated by arrows and dotted lines), respectively. (C) Time-course CD experiments demonstrate the transition from an unstructured monomeric state to an extended β-sheet conformation of the amyloid fibers. (D) Scheme describing the possible variation in aggregation pathways of Aβ40 based on different experimental data

depicted above. The ^{19}F spectrum above the scheme shows peaks that correspond to various intermediates formed as a result of Aβ40 aggregation. Panels C and D are adapted from references X and XX, respectively.

While the discussion of the plethora of biophysical techniques can be and have been used to study amyloid aggregation and morphology seems overall negative or unenthusiastic, it merely serves to demonstrate that studies involving amyloid research must encompass a wide array of experimental approaches to gain a full picture of the various processes occurring therein.

1.9 Using NMR to study amyloid aggregation

NMR has emerged as a vital tool for the structural and dynamic characterization of aggregate assembly (67–69), oligomer structure (9, 10, 70), and amyloid fibril structure (6, 65). While NMR must commonly be complemented with other biophysical approaches, it offers the capability to measure many of the quantities afforded by the techniques previously discussed, namely: (i) distinguishing monomeric, oligomer, and fibrillar species (ii) sensitivity to lowly populated species (iii) being non-perturbative (iv) no interference with small molecule inhibitors (v) achieving atomic resolution. The main disadvantage is the typical requirement for higher concentrations, although recent advancements in hardware have made possible the ability to work in the micromolar range.

This dissertation focuses on the development and application of two distinct NMR methodologies each of which with distinct advantages geared towards elucidating the mechanism of amyloid aggregation. Approaches from both solution- and solid-state NMR are used in this dissertation and manner in which they are used is discussed below.

1.9.1 Solution NMR and the application of fast acquisition NMR techniques

Solution NMR has long been a powerful biophysical tool for high-resolution structural and dynamic studies of biomacromolecules. Using the intrinsic magnetic properties of atomic

nuclei, NMR is used to determine protein structure, internal protein dynamics, and/or transient protein-protein interactions. Due to the high sensitivity and high natural abundane of the ^{1}H nucleus, one-dimenerionsal (1D) ^{1}H NMR is routinely used for the characterization of small organic and inorganic compounds. For studies of biomacromolecules, such as proteins or nucleic acids, multidimensional NMR is necessary to achieve higher resolution due to spectral overlap resulting from the sheer quantity of ^{1}H present. In protein NMR spectroscopy, one of the most widely used 2D NMR techniques used is the Heteronuclear Single Quantum Coherence (HSQC) experiment (Fig 1.7A) (71). HSQC uses J-coupling (i.e. through-bond coupling) to correlate a ^{1}H nucleus with a directly bonded ^{13}C or ^{15}N nucleus. The ^{1}H-^{15}N/^{13}C HSQC experiment is extensively used to examine protein structure and dynamics with residue specificity as function of any number of parameters, e.g. through changing environmental variables such as pH, salt concentration, temperature, or introduction of a ligand (71–73).

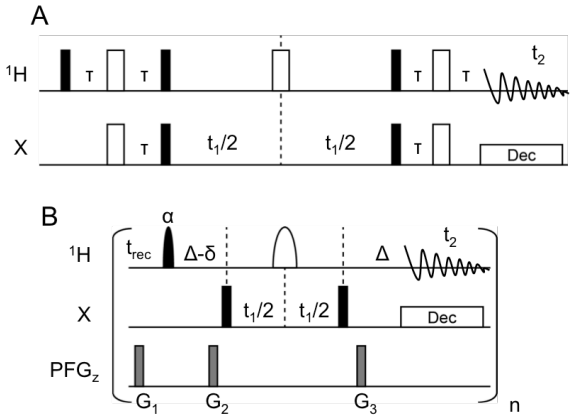

Figure 1.7 Pulse sequences to record ^{1}H-X correlation spectra.
(A) The standard ^{1}H-X HSQC experiment. The time delay τ is set to ($1/2J_{HX}$). (B) The SOFAST-HMQC experiment. The time delay Δ is set to ($1/2J_{HX}$) and t_{rec} is the recycle delay between scans. The delay δ accounts for spin evolution between pulses and is optimized prior to acquisition to yield pure absorption spectra. (A, B) Filled and open symbols indicate 90º and 180º pulses, respectively; except for the ^{1}H excitation pulse applied with a flip angle α designated in the SOFAST-HMQC experiment. In panel B, the gray filled symbols are gradient pulses that are used to purge undesired magnetization components. Panel B has been adapted from ref 72.

With the development of fast acquisition NMR methods, namely, the SOFAST-HMQC (band-Selective Optimized-Flip-Angle Short-Transient heteronuclear multiple quantum coherence) experiment, multidimensional experiments that previously took hours are reduced to an acquisition time of minutes (Fig. 1.7B) (71). As a result of this reduced experimental acquisition time, amyloid aggregation can be studied in real time without worry of differing sample conditions over the course of acquisition. For example, in the case of Aβ aggregation, fibers can form in as little as 2 hours and oligomers can often form with several minutes (61, 74). The loss of monomer to a larger, potentially structured oligomer or fiber will result in loss signal intensity due to changing populations or chemical exchange. The time required for the acquisition of an n-dimensional experiment is determined by the sensitivity of a given sample, the number of indirectly sampled dimensions (*n-1*), and the desired spectral resolution (71). What the SOFAST-HMQC experiment has done to reduce experimental is solved the problem of data sampling by reducing the time between scans (t_{rec}, Fig 1.7B) through enhanced longitudinal relaxation (achieved by band-selective ^{1}H pulse) (71).

Real-time NMR is a promising alternative to studying the time-course evolution of amyloid aggregation. Real-time 1D NMR has been previously used for Aβ and IAPP (58, 59); however, as mentioned previously, the lack of resolution hampers any high-resolution information that would otherwise be gained through 2D NMR studies. Two recent studies utilized single-site labeling incorporating a ^{19}F probe to track Aβ and IAPP aggregation (58, 59). Intriguingly, in the case of Aβ distinct new peaks could be observed deep into the incubation (> 50 days) and after the formation of fibers (see spectrum in Fig 1.6D). While real-time 1D NMR is highly useful, it is does not achieve details beyond low-resolution measurements. SOFAST-HMQC offers the unique ability to monitor amyloid aggregation at atomic resolution without the

time constraints typical of most 2D NMR experiments, allowing the kinetic processes of fibril or oligomer assembly to be tracked with residue specificity in real-time. Further details on application of this methodology to can be found in Chapter 4.

1.9.2 Magic Angle Spinning NMR and Radio frequency-driven dipolar recoupling

Solution NMR in limited in its ability to resolve molecules based on their size. With increasing molecular weight, anisotropic contributions to NMR signal intensity results in increased linewidths and, in turn, reduced spectral resolution. In solution samples, this line broadening is a result of decreased molecular tumbling rates, leading to decreased sampling of the molecules orientations. In true solid samples, there is essentially no molecular tumbling and, therefore, the spectrum of such a sample results in a powder pattern (Fig. 1.8, bottom). To overcome the molecular weight limit imposed by static NMR, a technique called magic angle spinning (MAS) is used to mechanically average the anisotropic interactions inherent to such systems. Moreover, MAS can be used on solution samples that have solid-like characteristics (e.g. amyloid oligomers) to bridge the gap between limitations imposed on both solution- and solid-state NMR methods; the molecular weight limit in solution NMR and problems with sensitivity in solid-state NMR. These limitations are further overcome by taking advantage of both solution- and solid-state techniques: performing solid-state NMR experiments on liquid sample with "solid" characteristics (75).

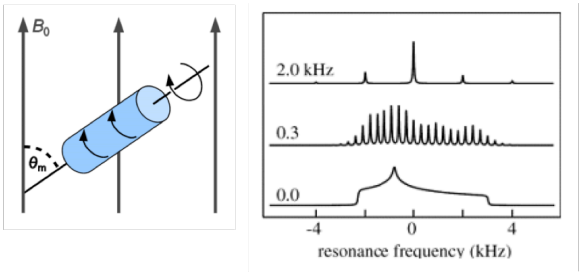

Figure 1.8 Magic angle spinning can create solution-like conditions on a solid sample.

Increasing MAS rates yields spectra that more closely resemble isotropic conditions. Spurious signals that may be attributed to an incomplete averaging by MAS appear under slow spinning conditions (middle).

While there are number of solid-state NMR techniques that can be applied in this regard, this dissertation will focus only on radiofrequency-driven dipolar recoupling (RFDR) (76). Recoupling pulse sequences are often used in MAS NMR to reintroduce and measure anisotropic interactions being averaged out by MAS. In other words, we use RF pulses synchronized with the spinning frequency of MAS to interfere with the averaging process that it induces to recouple the dipole interactions (77). Dipolar recoupling methods are often used in solid-state NMR experiments to measure distances between nuclei and, upon doing so with appropriate biomolecular systems, such techniques can be used as tool for structural biology (77, 78). The RFDR recoupling scheme is used to measure dipole interactions of homonuclear spins, and here specifically studied using ^{1}H-^{1}H dipole interactions (Fig 1.9, top). Several groups, including ours, have been exploring methods to improve sensitivity in the ^{1}H MAS NOESY experiment (Fig 1.9, bottom) to be used on various biological samples (26, 79–81). The RFDR-based 2D ^{1}H/^{1}H correlation experiment generates longitudinal exchange of magnetization during the mixing to obtain isotropic chemical shift correlation spectra via coherent ^{1}H-^{1}H dipolar coupling and the NOE (80). Thus, this approach is highly useful for non-deuterated solution samples not readily amenable to solution NMR techniques as it takes advantage of the "residual" dipolar couplings inherent to such systems. The Aβ oligomer is one such system that has primarily evaded high-resolution due to its size.

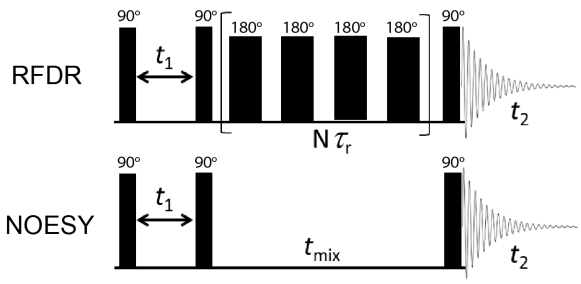

Figure 1.9 Pulse sequence schemes for 2D RFDR-based (top) and NOESY (bottom) ^{1}H/^{1}H chemical shift correlation experiments.

1.10 Dissertation objectives

While there are countless studies demonstrating the cytotoxic nature of Aβ and the relationship between various Aβ aggregates and their cytotoxicity, many questions remain. Particularly, in this dissertation, I first explore in greater detail Aβ's ability to bind to and disrupt cell membranes as a potential mechanism for cytotoxicity, paying particular attention to the role of membrane composition in diminishing or enhancing this effect while simultaneously understanding how membrane composition alters Aβ aggregation (Chapter 2) (82). Then, with the aim of further elucidating the Aβ aggregation pathway(s), I implement a combinational technique utilizing both solution- and solid-state NMR for the high-resolution characterization of Aβ oligomers (Chapter 3) (79). Additionally, using fast acquisition NMR techniques coupled with measurements of residual dipolar couplings by solution NMR, I investigate the transient, non-native states of the amyloid fiber elongation process (Chapter 4). These contributions are explored due to the fact that protofibrillar Aβ aggregates and/or the process of Aβ fibrillization remain probable causative or contributing agents in AD.

1.11 Acknowledgements and contributions

In the adapted portions of this chapter from Kotler, S.A. et al, (2014) *Chem. Soc. Rev.*, 43, 6692-6700:

Cell membrane related research was supported by funds from NIH (GM084018 and GM095640 to A.R.)

The portions of this chapter adapted from the above publication were edited and written by S.A.K., P.W., J.R.B., and A.R.

1.12 References

1. 2015 Alzheimer's disease facts and figures (2015) *Alzheimer's Dement.* **11**, 332–384

2. Hardy, J., and Selkoe, D. J. (2002) The amyloid hypothesis of Alzheimer's disease: progress and problems on the road to therapeutics. *Science*. **297**, 353–6

3. Benilova, I., Karran, E., and De Strooper, B. (2012) The toxic Aβ oligomer and Alzheimer's disease: an emperor in need of clothes. *Nat. Neurosci.* **15**, 349–57

4. Bateman, R. J., Xiong, C., Benzinger, T. L. S., Fagan, A. M., Goate, A., Fox, N. C., Marcus, D. S., Cairns, N. J., Xie, X., Blazey, T. M., Holtzman, D. M., Santacruz, A., Buckles, V., Oliver, A., Moulder, K., Aisen, P. S., Ghetti, B., Klunk, W. E., McDade, E., Martins, R. N., Masters, C. L., Mayeux, R., Ringman, J. M., Rossor, M. N., Schofield, P. R., Sperling, R. a, Salloway, S., and Morris, J. C. (2012) Clinical and biomarker changes in dominantly inherited Alzheimer's disease. *N. Engl. J. Med.* **367**, 795–804

5. Butterfield, S. M., and Lashuel, H. a (2010) Amyloidogenic protein-membrane interactions: mechanistic insight from model systems. *Angew. Chem. Int. Ed. Engl.* **49**, 5628–54

6. Tycko, R. (2006) Molecular structure of amyloid fibrils: insights from solid-state NMR. *Q Rev Biophys*. **39**, 1–55

7. Ross, C. a, and Poirier, M. a (2004) Protein aggregation and neurodegenerative disease. *Nat. Med.* **10 Suppl**, S10–7

8. Teplow, D. B. (2013) On the subject of rigor in the study of amyloid β -protein assembly. **5**, 1

9. Chimon, S., Shaibat, M. A., Jones, C. R., Calero, D. C., Aizezi, B., and Ishii, Y. (2007) Evidence of fibril-like β-sheet structures in a neurotoxic amyloid intermediate of Alzheimer's β-amyloid. *Nat. Struct. Mol. Biol.* **14**, 1157–64

10. Ahmed, M., Davis, J., Aucoin, D., Sato, T., Ahuja, S., Aimoto, S., Elliott, J. I., Van Nostrand, W. E., and Smith, S. O. (2010) Structural conversion of neurotoxic amyloid-beta(1-42) oligomers to fibrils. *Nat. Struct. Mol. Biol.* **17**, 561–567

11. Lambert, M. P., Barlow, a K., Chromy, B. a, Edwards, C., Freed, R., Liosatos, M., Morgan, T. E., Rozovsky, I., Trommer, B., Viola, K. L., Wals, P., Zhang, C., Finch, C. E., Krafft, G. a, and Klein, W. L. (1998) Diffusible, nonfibrillar ligands derived from Abeta1-42 are potent central nervous system neurotoxins. *Proc. Natl. Acad. Sci. U. S. A.* **95**, 6448–53

12. Brender, J. R., Salamekh, S., and Ramamoorthy, A. (2012) Membrane disruption and early events in the aggregation of the diabetes related peptide IAPP from a molecular perspective. *Acc. Chem. Res.* **45**, 454–462

13. Glabe, C. G. (2009) Amyloid Oligomer Structures and Toxicity

14. Walsh, D. M., Klyubin, I., Fadeeva, J. V, Cullen, W. K., Anwyl, R., Wolfe, M. S., Rowan, M. J., and Selkoe, D. J. (2002) Naturally secreted oligomers of amyloid beta protein potently inhibit hippocampal long-term potentiation in vivo. *Nature*. **416**, 535–9

15. Ono, K., Condron, M. M., and Teplow, D. B. (2009) Structure-neurotoxicity relationships of amyloid beta-protein oligomers. *Proc. Natl. Acad. Sci. U. S. A.* **106**, 14745–50

16. Kayed, R., Pensalfini, A., Margol, L., Sokolov, Y., Sarsoza, F., Head, E., Hall, J., and Glabe, C. (2009) Annular protofibrils are a structurally and functionally distinct type of amyloid oligomer. *J Biol Chem*. **284**, 4230–4237

17. Lashuel, H. A., Hartley, D., Petre, B. M., Walz, T., and Lansbury Jr., P. T. (2002) Neurodegenerative disease: amyloid pores from pathogenic mutations. *Nature*. **418**, 291

18. Vivekanandan, S., Brender, J. R., Lee, S. Y., and Ramamoorthy, A. (2011) A partially folded structure of amyloid-beta(1-40) in an aqueous environment. *Biochem. Biophys. Res. Commun.* **411**, 312–6

19. Ladiwala, A. R. a, Litt, J., Kane, R. S., Aucoin, D. S., Smith, S. O., Ranjan, S., Davis, J., Van Nostrand, W. E., and Tessier, P. M. (2012) Conformational differences between two amyloid β oligomers of similar size and dissimilar toxicity. *J. Biol. Chem.* **287**, 24765–73

20. Laurents, D. V, Gorman, P. M., Guo, M., Rico, M., Chakrabartty, A., and Bruix, M. (2005) Alzheimer's Abeta40 studied by NMR at low pH reveals that sodium 4,4-dimethyl-4-silapentane-1-sulfonate (DSS) binds and promotes beta-ball oligomerization. *J. Biol. Chem.* **280**, 3675–85

21. Yu, L., Edalji, R., Harlan, J. E., Holzman, T. F., Lopez, A. P., Labkovsky, B., Hillen, H., Barghorn, S., Ebert, U., Richardson, P. L., Miesbauer, L., Solomon, L., Bartley, D., Walter, K., Johnson, R. W., Hajduk, P. J., and Olejniczak, E. T. (2009) Structural characterization of a soluble amyloid beta-peptide oligomer. *Biochemistry*. **48**, 1870–7

22. Cerf, E., Sarroukh, R., Tamamizu-Kato, S., Breydo, L., Derclaye, S., Dufrêne, Y. F., Narayanaswami, V., Goormaghtigh, E., Ruysschaert, J.-M., and Raussens, V. (2009)

Antiparallel beta-sheet: a signature structure of the oligomeric amyloid beta-peptide. *Biochem. J.* **421**, 415–23

23. Sarroukh, R., Cerf, E., Derclaye, S., Dufrêne, Y. F., Goormaghtigh, E., Ruysschaert, J.-M., Raussens, V., Dufre, Y. F., and Raussens, J. R. V. (2011) Transformation of amyloid β(1-40) oligomers into fibrils is characterized by a major change in secondary structure. *Cell. Mol. Life Sci.* **68**, 1429–38

24. Jan, A., Adolfsson, O., Allaman, I., Buccarello, A.-L., Magistretti, P. J., Pfeifer, A., Muhs, A., and Lashuel, H. A. (2011) Abeta42 neurotoxicity is mediated by ongoing nucleated polymerization process rather than by discrete Abeta42 species. *J. Biol. Chem.* **286**, 8585–96

25. Mani, R., Cady, S. D., Tang, M., Waring, A. J., Lehrer, R. I., and Hong, M. (2006) Membrane-dependent oligomeric structure and pore formation of a beta-hairpin antimicrobial peptide in lipid bilayers from solid-state NMR. *Proc. Natl. Acad. Sci. U. S. A.* **103**, 16242–7

26. Ramamoorthy, A., and Xu, J. (2013) 2D 1H/1H RFDR and NOESY NMR experiments on a membrane-bound antimicrobial peptide under magic angle spinning. *J. Phys. Chem. B*. **117**, 6693–700

27. Jang, H., Connelly, L., Arce, F. T., Ramachandran, S., Lal, R., Kagan, B. L., and Nussinov, R. (2013) Alzheimer's disease: which type of amyloid-preventing drug agents to employ? *Phys. Chem. Chem. Phys.* 10.1039/c3cp00017f

28. McLaurin, J., and Chakrabartty, A. (1997) Characterization of the interactions of Alzheimer beta-amyloid peptides with phospholipid membranes. *Eur J Biochem*. **245**, 355–363

29. Kakio, A., Nishimoto, S., Yanagisawa, K., Kozutsumi, Y., and Matsuzaki, K. (2002) Interactions of amyloid beta-protein with various gangliosides in raft-like membranes: importance of GM1 ganglioside-bound form as an endogenous seed for Alzheimer amyloid. *Biochemistry*. **41**, 7385–7390

30. Yanagisawa, K., Odaka, A., Suzuki, N., and Ihara, Y. (1995) GM1 ganglioside-bound amyloid beta-protein (A beta): a possible form of preamyloid in Alzheimer's disease. *Nat Med*. **1**, 1062–1066

31. Matsuzaki, K., Kato, K., and Yanagisawa, K. (2010) Abeta polymerization through interaction with membrane gangliosides. *Biochim. Biophys. Acta*. **1801**, 868–77

32. McLaurin, J., Franklin, T., Fraser, P. E., and Chakrabartty, a (1998) Structural transitions associated with the interaction of Alzheimer beta-amyloid peptides with gangliosides. *J. Biol. Chem.* **273**, 4506–15

33. Ikeda, K., Yamaguchi, T., Fukunaga, S., Hoshino, M., and Matsuzaki, K. (2011) Mechanism of amyloid beta-protein aggregation mediated by GM1 ganglioside clusters. *Biochemistry*. **50**, 6433–6440

34. Wakabayashi, M., and Matsuzaki, K. (2007) Formation of amyloids by Abeta-(1-42) on NGF-differentiated PC12 cells: roles of gangliosides and cholesterol. *J. Mol. Biol.* **371**, 924–33

35. Yagi-Utsumi, M., Kameda, T., Yamaguchi, Y., and Kato, K. (2010) NMR characterization of the interactions between lyso-GM1 aqueous micelles and amyloid beta. *FEBS Lett.* **584**, 831–6

36. Williamson, M. P., Suzuki, Y., Bourne, N. T., and Asakura, T. (2006) Binding of amyloid beta-peptide to ganglioside micelles is dependent on histidine-13. *Biochem. J.* **397**, 483–90

37. Arispe, N., Rojas, E., and Pollard, H. B. (1993) Alzheimer disease amyloid beta protein forms calcium channels in bilayer membranes: blockade by tromethamine and aluminum. *Proc Natl Acad Sci U S A*. **90**, 567–571

38. Quist, A., Doudevski, I., Lin, H., Azimova, R., Ng, D., Frangione, B., Kagan, B., Ghiso, J., and Lal, R. (2005) Amyloid ion channels: a common structural link for protein-misfolding disease. *Proc Natl Acad Sci U S A*. **102**, 10427–10432

39. Rhee, S. K., Quist, A. P., and Lal, R. (1998) Amyloid beta protein-(1-42) forms calcium-permeable, Zn2+-sensitive channel. *J Biol Chem*. **273**, 13379–13382

40. Jang, H., Zheng, J., Lal, R., and Nussinov, R. (2008) New structures help the modeling of toxic amyloidbeta ion channels. *Trends Biochem. Sci.* **33**, 91–100

41. Capone, R., Jang, H., Kotler, S. A., Kagan, B. L., Nussinov, R., and Lal, R. (2012) Probing structural features of Alzheimer's amyloid-β pores in bilayers using site-specific amino acid substitutions. *Biochemistry*. **51**, 776–85

42. Capone, R., Jang, H., Kotler, S. A., Connelly, L., Teran Arce, F., Ramachandran, S., Kagan, B. L., Nussinov, R., and Lal, R. (2012) All-d-Enantiomer of β-Amyloid Peptide Forms Ion Channels in Lipid Bilayers. *J. Chem. Theory Comput.* **8**, 1143–1152

43. Prangkio, P., Yusko, E. C., Sept, D., Yang, J., and Mayer, M. (2012) Multivariate analyses of amyloid-beta oligomer populations indicate a connection between pore formation and cytotoxicity. *PLoS One*. **7**, e47261

44. Solomonov, I., Korkotian, E., Born, B., Feldman, Y., Bitler, A., Rahimi, F., Li, H., Bitan, G., and Sagi, I. (2012) Zn2+-Abeta40 complexes form metastable quasi-spherical oligomers that are cytotoxic to cultured hippocampal neurons. *J Biol Chem*. **287**, 20555–20564

45. Hoshi, M., Sato, M., Matsumoto, S., Noguchi, A., Yasutake, K., Yoshida, N., and Sato, K. (2003) Spherical aggregates of beta-amyloid (amylospheroid) show high neurotoxicity and activate tau protein kinase I/glycogen synthase kinase-3beta. *Proc. Natl. Acad. Sci. U. S. A.* **100**, 6370–5

46. Sciacca, M. F. M., Kotler, S. A., Brender, J. R., Chen, J., Lee, D. K., and Ramamoorthy, A. (2012) Two-step mechanism of membrane disruption by Aβ through membrane fragmentation and pore formation. *Biophys. J.* **103**, 702–710

47. Brender, J. R., Lee, E. L., Hartman, K., Wong, P. T., Ramamoorthy, A., Steel, D. G., and Gafni, A. (2011) Biphasic effects of insulin on islet amyloid polypeptide membrane disruption. *Biophys. J.* **100**, 685–692

48. Sciacca, M. F. M., Brender, J. R., Lee, D.-K. K., and Ramamoorthy, A. (2012) Phosphatidylethanolamine enhances amyloid fiber-dependent membrane fragmentation. *Biochemistry*. **51**, 7676–7684

49. Sparr, E., Engel, M. F., Sakharov, D. V, Sprong, M., Jacobs, J., de Kruijff, B., Hoppener, J. W., and Killian, J. A. (2004) Islet amyloid polypeptide-induced membrane leakage involves uptake of lipids by forming amyloid fibers. *FEBS Lett*. **577**, 117–120

50. DeToma, A. S., Salamekh, S., Ramamoorthy, A., and Lim, M. H. (2012) Misfolded proteins in Alzheimer's disease and type II diabetes. *Chem. Soc. Rev.* **41**, 608–21

51. Necula, M., Kayed, R., Milton, S., and Glabe, C. G. (2007) Small molecule inhibitors of aggregation indicate that amyloid beta oligomerization and fibrillization pathways are independent and distinct. *J. Biol. Chem.* **282**, 10311–24

52. Engel, M. F. M., vandenAkker, C. C., Schleeger, M., Velikov, K. P., Koenderink, G. H., and Bonn, M. (2012) The polyphenol EGCG inhibits amyloid formation less efficiently at phospholipid interfaces than in bulk solution. *J. Am. Chem. Soc.* **134**, 14781–8

53. Diaz, J. C., Simakova, O., Jacobson, K. a, Arispe, N., and Pollard, H. B. (2009) Small molecule blockers of the Alzheimer Abeta calcium channel potently protect neurons from Abeta cytotoxicity. *Proc Natl Acad Sci U S A*. **106**, 3348–3353

54. Jarvet, J., Danielsson, J., Damberg, P., Oleszczuk, M., and Gräslund, A. (2007) Positioning of the Alzheimer Abeta(1-40) peptide in SDS micelles using NMR and paramagnetic probes. *J. Biomol. NMR*. **39**, 63–72

55. Jan, A., Hartley, D. M., and Lashuel, H. a (2010) Preparation and characterization of toxic Abeta aggregates for structural and functional studies in Alzheimer's disease research. *Nat. Protoc.* **5**, 1186–209

56. Arosio, P., Knowles, T. P. J., and Linse, S. (2015) On the lag phase in amyloid fibril formation. *Phys. Chem. Chem. Phys.* 10.1039/c4cp05563b

57. Patel, H. R., Pithadia, A. S., Brender, J. R., Fierke, C. A., and Ramamoorthy, A. (2014) In Search of Aggregation Pathways of IAPP and Other Amyloidogenic Proteins: Finding Answers through NMR Spectroscopy. *J. Phys. Chem. Lett.* **5**, 1864–1870

58. Suzuki, Y., Brender, J. R., Hartman, K., Ramamoorthy, A., and Marsh, E. N. G. (2012) Alternative pathways of human islet amyloid polypeptide aggregation distinguished by (19)f nuclear magnetic resonance-detected kinetics of monomer consumption. *Biochemistry*. **51**, 8154–62

59. Suzuki, Y., Brender, J. R., Soper, M. T., Krishnamoorthy, J., Zhou, Y., Ruotolo, B. T., Kotov, N. a, Ramamoorthy, A., and Marsh, E. N. G. (2013) Resolution of oligomeric species during the aggregation of Aβ1-40 using (19)F NMR. *Biochemistry*. **52**, 1903–12

60. Lee, J., Culyba, E. K., Powers, E. T., and Kelly, J. W. (2011) Amyloid-beta forms fibrils by nucleated conformational conversion of oligomers. *Nat Chem Biol*. **7**, 602–609

61. Fu, Z., Aucoin, D. S., Davis, J., Van Nostrand, W. E., and Smith, S. O. (2015) Mechanism of nucleated conformational conversion of Aβ42. *Biochemistry*. 10.1021/acs.biochem.5b00467

62. Jeong, J. S., Ansaloni, A., Mezzenga, R., Lashuel, H. a, and Dietler, G. (2013) Novel mechanistic insight into the molecular basis of amyloid polymorphism and secondary nucleation during amyloid formation. *J. Mol. Biol.* **425**, 1765–81

63. Mastrangelo, I. a, Ahmed, M., Sato, T., Liu, W., Wang, C., Hough, P., and Smith, S. O. (2006) High-resolution atomic force microscopy of soluble Abeta42 oligomers. *J. Mol. Biol.* **358**, 106–19

64. Sachse, C., Grigorieff, N., and Fändrich, M. (2010) Nanoscale flexibility parameters of Alzheimer amyloid fibrils determined by electron cryo-microscopy. *Angew. Chem. Int. Ed. Engl.* **49**, 1321–3

65. Petkova, A. T., Leapman, R. D., Guo, Z., Yau, W.-M., Mattson, M. P., and Tycko, R. (2005) Self-propagating, molecular-level polymorphism in Alzheimer's beta-amyloid fibrils. *Science*. **307**, 262–265

66. Paravastu, A. K., Leapman, R. D., Yau, W., and Tycko, R. (2008) Molecular structural basis for polymorphism in Alzheimer's beta-amyloid fibrils. *Proc. Natl. Acad. Sci. U. S. A.* **105**, 18349–54

67. Fawzi, N. L., Ying, J., Torchia, D. a, and Clore, G. M. (2010) Kinetics of amyloid beta monomer-to-oligomer exchange by NMR relaxation. *J. Am. Chem. Soc.* **132**, 9948–51

68. Fawzi, N. L., Ying, J., Ghirlando, R., Torchia, D. A., and Clore, G. M. (2011) Atomic-resolution dynamics on the surface of amyloid-β protofibrils probed by solution NMR. *Nature*. **480**, 268–272

69. Fawzi, N. L., Libich, D. S., Ying, J., Tugarinov, V., and Clore, G. M. (2014) Characterizing Methyl-Bearing Side Chain Contacts and Dynamics Mediating Amyloid β Protofibril Interactions Using 13 C methyl -DEST and Lifetime Line Broadening. *Angew. Chemie*. **126**, 10513–10517

70. Walsh, P., Neudecker, P., and Sharpe, S. (2010) Structural properties and dynamic behavior of nonfibrillar oligomers formed by PrP(106-126). *J. Am. Chem. Soc.* **132**, 7684–95

71. Schanda, P., Kupce, E., and Brutscher, B. (2005) SOFAST-HMQC experiments for recording two-dimensional heteronuclear correlation spectra of proteins within a few seconds. *J. Biomol. NMR*. **33**, 199–211

72. Sathyamoorthy, B., Lee, J., Kimsey, I., Ganser, L. R., and Al-Hashimi, H. (2014) Development and application of aromatic [(13)C, (1)H] SOFAST-HMQC NMR experiment for nucleic acids. *J. Biomol. NMR*. **60**, 77–83

73. Viéville, J. M. P., Charbonnier, S., Eberling, P., Starck, J.-P., and Delsuc, M.-A. (2014) A new NMR technique to probe protein-ligand interaction. *J. Pharm. Biomed. Anal.* **89**, 18–23

74. O'Malley, T. T., Oktaviani, N. A., Zhang, D., Lomakin, A., O'Nuallain, B., Linse, S., Benedek, G. B., Rowan, M. J., Mulder, F. A. A., and Walsh, D. M. (2014) Aβ dimers differ from monomers in structural propensity, aggregation paths and population of synaptotoxic assemblies. *Biochem. J.* **461**, 413–26

75. Power, W. P. (2011) *Chapter 3 - High-Resolution Magic Angle Spinning-Enabling Applications of NMR Spectroscopy to Semi-Solid Phases*, 1st Ed., Elsevier Ltd., 10.1016/B978-0-12-385857-3.00003-7

76. Bennett, A. E., Griffin, R. G., Ok, J. H., and Vega, S. (1992) Chemical shift correlation spectroscopy in rotating solids: Radio frequency-driven dipolar recoupling and longitudinal exchange. *J. Chem. Phys.* **96**, 8624

77. Griffin, R. G. (1998) NMR supplement Dipolar recoupling in MAS spectra of biological solids

78. Castellani, F., van Rossum, B., Diehl, A., Schubert, M., Rehbein, K., and Oschkinat, H. (2002) Structure of a protein determined by solid-state magic-angle-spinning NMR spectroscopy. *Nature*. **420**, 98–102

79. Kotler, S. A., Brender, J. R., Vivekanandan, S., Suzuki, Y., Yamamoto, K., Monette, M., Krishnamoorthy, J., Walsh, P., Cauble, M., Holl, M. M. B., Marsh, E. N. G., and Ramamoorthy, A. (2015) High-resolution NMR characterization of low abundance oligomers of amyloid-β without purification. *Sci. Rep.* **5**, 11811

80. Aucoin, D., Camenares, D., Zhao, X., Jung, J., Sato, T., and Smith, S. O. (2009) High-resolution 1H MAS RFDR NMR of biological membranes. *J. Magn. Reson.* **197**, 77–86

81. Pandey, M. K., Vivekanandan, S., Yamamoto, K., Im, S., Waskell, L., and Ramamoorthy, A. (2014) Proton-detected 2D radio frequency driven recoupling solid-state NMR studies on micelle-associated cytochrome-b(5). *J. Magn. Reson.* **242**, 169–79

82. Kotler, S. A., Sciacca, M. F. M., Brender, J. R., Chen, J., Yamamoto, K., Lee, D., and Ramamoorthy, A. (2013) Gangliosides Mediate a Two-Step Mechanism of Membrane Disruption by Beta-Amyloid: Initial Pore Formation Followed by Membrane Fragmentation. *Biophys. J.* **104**, 217A–217A

Chapter 2: Elucidating the Role of Lipid Composition on Aβ Aggregation and Aβ-Induced Membrane Disruption

This chapter was adapted from the following publication:

Sciacca, M.F.M., Kotler, S.A., Brender, J.R., Chen, J., Lee, D.K., and Ramamoorthy, A. (2012) Two-step mechanism of membrane disruption by Aβ through membrane fragmentation and pore formation. *Biophysical Journal*, **103**, 702-710.

2.1. Introduction

Alzheimer's disease is a devastating neurodegenerative disease characterized by memory loss and severe cognitive impairment. A key pathological marker of Alzheimer's disease is the formation of extracellular plaques caused by the misfolding and aggregation of the Aβ40 and $A\beta_{1-42}$ peptides into extended fibrillar structures known as amyloid (1,2). Amyloid formation by Aβ40 is believed to be a key early stage in the development of Alzheimer's, as Aβ40 aggregation has been repeatedly linked to neuronal dysfunction and death (3). The aggregation of Aβ40 generates a complex, multifactorial response in neurons, leaving the actual source of Aβ40 cytotoxicity unresolved. A number of studies have identified several factors that may contribute to the pathology of Alzheimer's disease, including the generation of reactive oxygen species during aggregation, excessive aggregation of misfolded proteins leading to stress in the endoplasmic reticulum, inflammation, disruption of cellular membrane integrity, and activation of cell surface receptors that lead to cell death (3).

Although the exact mechanism by which Aβ causes neuronal death is not certain, one of the most clear and consistent pathologies in Alzheimer's disease is an elevation of cytoplasmic

Ca^{2+} in the vicinity of Aβ amyloid deposits (4,5). The mechanism by which Aβ stimulates Ca^{2+} influx has not been fully elucidated, but it has been suggested that Aβ can directly disrupt membranes through the formation of ion channels (the "channel hypothesis of Alzheimer's disease") (6,7). In the channel hypothesis, small annular oligomers of Aβ possessing a hydrophobic exterior and hydrophilic interior insert into the membrane, spanning the bilayer (8,9). The hollow structure of the oligomers allows ions to cross through the hydrophilic interior of the pore, causing an unregulated influx of Ca^{2+} into the cell. Since both neurons and mitochondria are highly sensitive to perturbations in ionic strength, a small perturbation in intracellular calcium levels caused by the unregulated Aβ channels can trigger an apoptotic cascade (10).

Experimental support for the channel hypothesis largely rests on atomic force and electron microscopy and single channel conductance measurements. Annular structures suggestive of ion channels have been directly observed by AFM when Aβ40 and $Aβ_{1-42}$ is reconstituted into planar lipid bilayers (9). The formation of these annular structures correlates with single-channel ion conductance measurements which show step-wise current fluctuations suggestive of the formation of discrete pores (9,11-13). Like endogenous calcium channels, the channels formed by Aβ are charge and size selective and can be blockaded by specific molecules such as Zn^{2+} that bind to the interior of the pore (14-17). The ability of Aβ channels to be blockaded by Zn^{2+} suggests a specific structure is involved in membrane disruption rather than a generalized disruption of the physical integrity of the bilayer.

Although the channel hypothesis accounts for many facets of Aβ toxicity through membrane disruption, some facets remain unexplained. First, large (up to 30 nm in diameter) spherical aggregates of Aβ have been repeatedly found to be toxic (18-20). This finding is

surprising in light of the channel hypothesis, which would predict such large spherical aggregates could not form ion channels unless disassembled into smaller aggregates. Second, aggregation of Aβ is often accompanied by large-scale morphological changes in the membrane that would not be expected by the insertion of small oligomeric pores (21-23). Rather, these large-scale morphological changes suggest physical disruption of the membrane also takes place after prolonged incubation with Aβ, which may be a contributing or dominant factor in the toxicity of Aβ. It has been suggested that the elongation of existing fibrils adsorbed to the membrane can remove lipids from the membrane via a detergent-like mechanism, causing membrane disruption that could lead to cell death (24,25). However, the relationship between these two types of membrane disruption by Aβ and other amyloidogenic proteins has not been defined.

We show here through the use of model membrane systems that the mechanism of Aβ membrane disruption in vitro is likely to be mediated by a two-step process similar to that proposed for IAPP: (i) prior to fibril formation, soluble oligomers bind to the membrane to form small channel-like pores and (ii) Aβ fibril elongation causes membrane fragmentation through a detergent-like mechanism. Furthermore, we found that the fiber-dependent step of membrane disruption only occurred in the presence of gangliosides, whereas pore formation occurred at low level in the absence of gangliosides.

2.2. Results

2.2.1. Oligomerization of Aβ40 on the membrane strongly disrupts ganglioside-containing membranes.

Membrane disruption by Aβ40 was estimated by quantifying dye leakage induced by Aβ40 from vesicle encapsulated 6-carboxyfluorescein (26). Previous measurements have shown freshly dissolved Aβ40 typically induces a very small amount of dye release for standard

membrane compositions in comparison to other membrane disruptive proteins such as antimicrobial peptides (27,28). However, these experiments usually measured membrane disruption only for a few minutes after the addition of Aβ40 and therefore did not take into account the time-dependent oligomerization of the Aβ40 peptide (27-29).

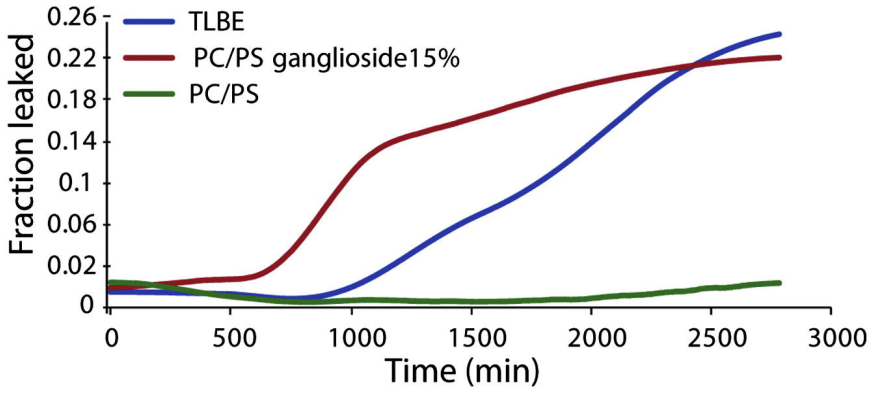

Figure 2.1 Membrane disruption induced by Aβ40, as measured by the 6-carboxyfluorescein dye leakage assay.
The graph illustrates the release of 6-carboxyfluorescein induced by 10 μM Aβ40 from 7:3 POPC/POPS LUVs (green line), 5:3.5:1.5 POPC/POPS/gangliosides LUVs (red line), and TBLE LUVs (blue line). Dye leakage occurs only after a lag period and is detected only in ganglioside-containing membranes. Experiments were performed at room temperature in 10 mM phosphate buffer, pH 7.4, 100 mM NaCl, and all LUV concentrations were 0.2 mg/ml. Results are the average of three measurements.

To take into account how the ongoing polymerization of Aβ40 may affect membrane disruption, we recorded dye leakage from model membranes over several days after the addition of freshly dissolved Aβ40 (Fig. 2.1). Corresponding assays using the amyloid sensitive dye thioflavin T (ThT) were used to measure fiber formation (Fig. 2.2). No significant leakage was observed from membranes composed of only POPC/POPS within two days, suggesting that Aβ40 does not cause membrane defects that allow the passage of 6-carboxyfluorescein in membranes in POPC/POPS membranes. However, membrane binding by Aβ40 is highly sensitive to membrane composition (30,31). To test a more physiologically relevant membrane composition, we performed the identical experiment with lipid vesicles formed from total lipid

brain extract (TLBE) with strikingly different results. Leakage from TLBE vesicles was initially low, similar to the leakage observed from POPC/POPS vesicles. However, leakage from TLBE vesicles sharply increased after a lag time of approximately 1000 minutes after the addition of Aβ40. The time–scale of release shares the same sigmoidal profile as amyloid formation (Fig. 2.1-2), suggesting this second phase of membrane disruption is correlated with fiber formation. However, since the ThT assay measures fiber formation occurring both in solution and on the membrane, an exact correspondence cannot be made because of the differing sensitivities of the two assays.

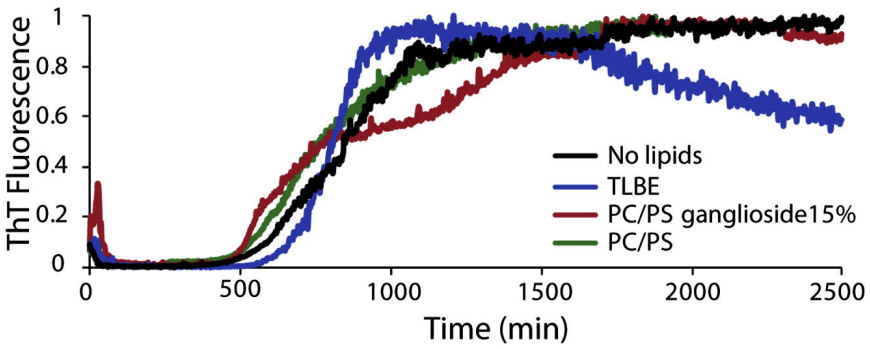

Figure 2.2 Kinetics of Aβ40 amyloid formation measured by ThT fluorescent emission.
The graph shows 10 μM Aβ40 in buffer in the absence of membranes (black line) an din the presence of 0.2 mg/ml 7:3 POPC/POPS LUVs (green line), 5.5:3:1.5 POPC/POPS/gangliosides LUVs (red line), or TBLE LUVs (blue line). Experiments were performed at room temperature in 10 mM phosphate buffer, pH 7.4, 100 mM NaCl. Results are the average of three measurements.

The dye release assay shows Aβ40 is substantially more efficient at disrupting TBLE vesicles than PC/PS vesicles. The TLBE is a complex mixture of lipids containing a variety of phospholipids, cholesterol, sphingolipids and gangliosides. Gangliosides in particular may be important for membrane disruption, as several studies have shown binding to the membrane surface is strongly enhanced by the ganglioside content (27,32-35). In addition, fiber formation is greatly accelerated by the presence of gangliosides, which may affect an oligomerization dependent process (25,32,36-41).

To test if the presence of ganglioside contributed to membrane disruption by oligomeric Aβ40, we performed the same dye leakage experiment using a simpler model membrane system (POPC/POPS/total ganglioside extract, molar ratio 5.5/3/1.5) containing an amount of ganglioside similar to that found in the total lipid brain extract. The results for this sample resemble the results obtained from total lipid brain extract (Fig. 2.1, red line), confirming that the presence of ganglioside in the membrane is sufficient for membrane defects that allow the passage of 6-carboxyfluorescein.

2.2.2. Cation-selective pores form immediately upon addition of Aβ to all membrane types.

The carboxyfluorescein assay suggests membrane disruption after the addition of Aβ40 is initially low but becomes higher after oligomerization begins. While this finding is consistent with the well-known toxicity of protofibrillar Aβ, many conductance studies in planar lipid bilayers have shown channel-like activity occurring immediately after the addition of freshly dissolved Aβ40 (42-46), well before the appearance of fibers (47,48). In addition, the pores detected by electrical recording are cation-selective (6-carboxyfluorescein is negatively charged) and are predicted through AFM measurements to have an inner diameter of 2 nm, which may be too small to allow efficient passage of the 6-carboxyfluorescein molecule (9,49-51). This raises the possibility that Aβ40 quickly forms pores in the membrane, but the pores are not detected by the 6-carboxyfluorescein dye leakage assay due to the size or charge of the molecule.

To test this possibility, we measured the influx of calcium ions into the LUV using vesicle encapsulated calcium sensitive Fura-2 dye. Calcium ions are smaller than 6-carboxyfluorescein (the Stokes radius of the hydrated calcium ion is 0.3 nm compared to 0.7 nm

for fluorescein) (52,53) and positively charged, and therefore measurements of Ca^{2+} influx more directly correspond to conductance measurements on planar lipid bilayers.

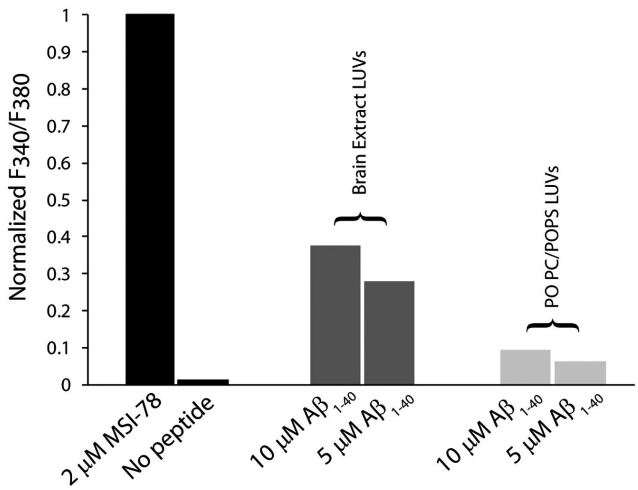

Figure 2.3 Ca2+ influx into LUVs after the addition of freshly dissolved Aβ40.
The maximum values of Ca2+ ion influx detected by encapsulated Fura-2 after 30 min of incubation with freshly dissolved Aβ40 from 0.2 mg/ml of TBLE LUVs (dark gray bars) or 7:3 POPC/POPS LUVs (light gray bars) are shown. In contrast to the 6-carboxyfluorescein due release assay, Ca2+ influx occurs shortly after the addition of Aβ40 and occurs weakly in the absence of gangliosides. The antimicrobial peptide MSI-78 was used as a reference for total disruption of membranes (black bars).

Fig. 2.3 shows the calcium influx obtained 30 minutes after incubation with Aβ40. Influx of Ca^{2+} occurs immediately after the addition of the peptide (within 10 minutes), well before membrane disruption as measured by the 6-carboxyfluorescein measurement (Fig. 2.1) and fiber formation as measured by ThT fluorescence (Fig. 2.2). The amount of influx induced by Aβ40 in TLBE vesicles is significant, but less than that induced by the strongly membrane disruptive antimicrobial peptide MSI-78 which completely disrupts the membrane at equivalent concentrations (Fig. 2.3) (54). Interestingly, we detected calcium influx in POPC/POPS LUVs, which do not contain gangliosides (Fig. 2.3, light gray bars), although the amount is less than that observed for the total brain extract LUV. This finding is in contrast to the 6-carboxyfluorescein assay in which membrane disruption of POPC/POPS LUVs is negligible

even after prolonged incubation. The small but measureable Ca^{2+} influx in POPC/POPS LUVs suggests that the presence of ganglioside enhances the formation of cation-selective small pores by the peptide, but is not absolutely essential for their formation.

2.2.3. Zinc ions can block early permeabilization by pores but not fiber-dependent membrane disruption.

To confirm calcium influx is correlated with the formation of small pores similar to those detected by electrical recording in planar bilayers, we repeated the previous experiment using Zn^{2+} ions instead of Ca^{2+}. The ability of Zn^{2+} to block the activity of the Aβ40 peptide channel in single channel conductance measurements has been well established (13,50,55-57) and is believed to result from the specific binding of Zn^{2+} to His-13 and His-14 in the interior of the channel (58). Accordingly, Zn^{2+} is not expected to penetrate into LUVs if the pores detected by the Fura-2 assay are similar to those detected by single channel recording.

Fig. 2.4 shows a comparison of the results obtained with Fura-2 assay using calcium ions (red line) and zinc ions (blue line). While we clearly observed influx of Ca^{2+} inside the LUV immediately after the addition of Aβ40, we did not observe any influx of Zn^{2+}. Since Fura-2 binds Zn^{2+} more tightly than Ca^{2+} (59) and MSI-78 permits influx of both Ca^{2+} and Zn^{2+} (Fig. A.1), this result indicates that Zn^{2+}, unlike Ca^{2+}, is unable to penetrate into the interior LUV despite the similar charge and size of both ions. This finding suggests that the first step of membrane disruption involves the formation of small-sized pores similar to those detected by single channel electrical recording.

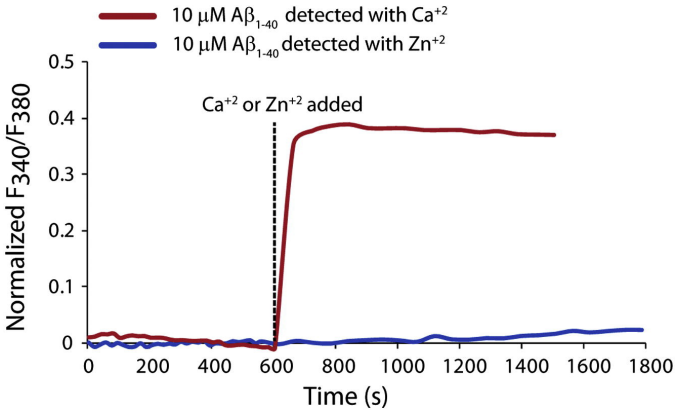

Figure 2.4 Zn2+ inhibits the pore activity of freshly dissolved Aβ40.
The graph shows the influx of Ca2+ (red line) and Zn2+ (blue line) ions induced by Aβ40 on 0.2 mg/ml of TBLE LUVs. Freshly dissolved Aβ40 was added to each sample at time zero. Ca2+ or Zn2+ was added at 600 s as indicated by the dashed line. Fura-2 is sensitive to both Zn2+ and Ca2+ ions, as indicated by a control experiment performed with MSI-78 (Fig. S1.4).

As mentioned above, membrane disruption is initially selective for Ca^{2+} over carboxyfluorescein; however, becomes nonselective as time progresses (compare Fig. 2.1 and 2.3). This finding implies two distinct mechanisms are operational in membrane disruption by Aβ40. To verify that the mechanism underlying the second step of membrane disruption is different from the initial pore formation and to demonstrate it involves fiber growth on the surface of the bilayer, we measured the influx of ions into the LUV caused by fiber elongation by adding freshly dissolved Aβ40 to the solution after incubation of the model membrane with preformed fibers. As expected, mature preformed fibers, which do not disrupt membranes (35), did not induce the influx of Ca^{2+} into TLBE LUVs (Fig. 2.5, black line) by themselves. When the reaction is seeded with pre-formed fibers of Aβ40, the LUVs became permeable to both Ca^{2+} and Zn^{2+}. This finding indicates that the elongation of the amyloid fibers on the membrane surface disrupts membranes by a mechanism different from that initially observed when freshly dissolved Aβ40 is added to the membrane, since the defects in the membrane caused by fiber elongation are permeable to Zn^{2+}.

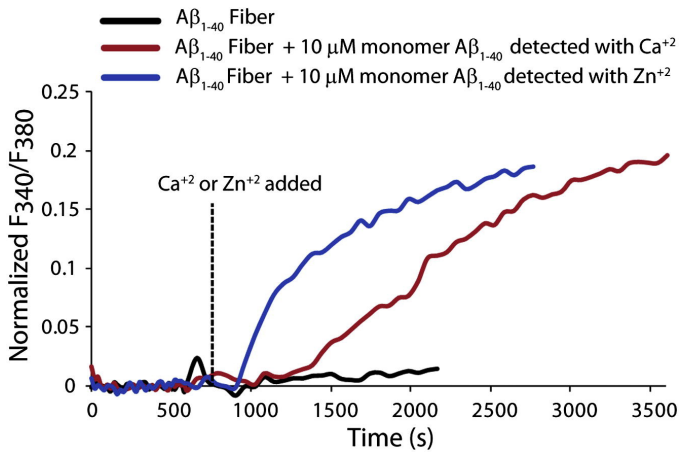

Figure 2.5 Zn2+ ions cannot block the fiber-dependent step of membrane disruption.
The figure shows the influx of Ca2+ (red line) and Zn2+ (blue line) ions induced by adding freshly dissolved Aβ40 to 0.2 mg/ml of TBLE LUVs incubated with preformed fibers. Freshly dissolved Aβ40 was added to each sample at time zero, and Ca2+ and Zn2+ was added 600 s as indicated by the dashed line. No Ca2+ influx was detected after the addition of preformed fibers alones (black line). The influx of bot Ca2+ and Zn2+ ions (red and blue lines, respectively) were detected by seeding Aβ40 fiber formation with preformed fibers. This finding suggests that the fiber-dependent step of membrane disruption is not well correlated with pore formation.

2.2.4. Fiber-dependant membrane disruption occurs by a detergent-like mechanism.

The Fura-2 assay did not allow us to determine how membrane disruption by fiber growth occurs. For other amyloidogenic peptides, it has been demonstrated that fiber growth is associated with the extraction of lipids from the membrane surface, resulting in the complete fragmentation of the membrane (60,61). Thus, one of the possible mechanisms to explain the fiber-dependent step of membrane disruption by Aβ40 is a detergent-like mechanism characterized by the fragmentation of the membrane into peptide-lipid micelles or vesicles without the appearance of defined pores.

To test this hypothesis we incubated LUV samples with Aβ40 for two days, centrifuged the samples to sediment intact LUVs, and then measured lipid concentrations in the supernatant by the Stewart assay (62). Fiber formation is expected to be complete within the two day incubation time (Fig. 2.2). For samples without Aβ40 (black bars in Fig. 2.6), only a small percentage of the total lipid concentration could be found in the supernatant, confirming almost

all of the lipids had pelleted after centrifugation and lipids in the supernatant are likely to be the result of membrane fragmentation by Aβ40. Incubation with Aβ40 caused significant membrane fragmentation only of ganglioside-containing membranes (Fig. 2.6). For the POPC/POPS LUV samples (Fig. 2.6, light gray bar), the addition of Aβ40 did not elevate the soluble fraction of lipid, in agreement with the lack of carboxyfluorescein release from this sample (Fig. 2.1). This finding suggests that membrane disruption by fiber elongation may occur by a detergent-like mechanism. Moreover, this result also matches with the 6-carboxyfluorescein dye leakage assay showing that membrane disruption occurs only if ganglioside is present in the membrane composition.

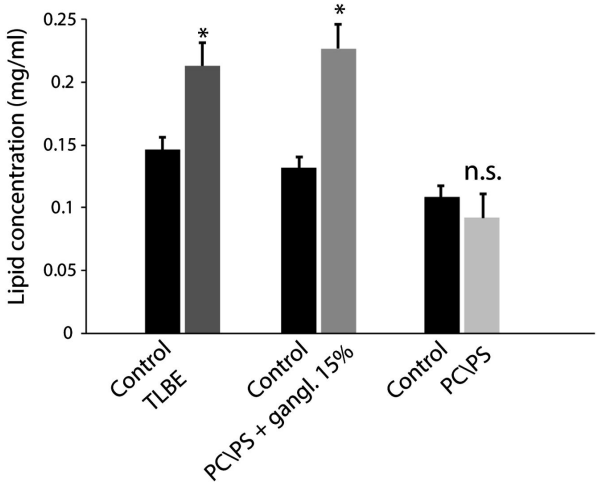

Figure 2.6 Membrane fragmentation induced by prolonged incubation with Aβ40.
Lipid concentrations in the supernatant after centrifugation from TBLE LUVs (dark gray) and 5.5:3:1.5 POPC/POPC/gangliosides LUVs (gray) after incubation with Aβ40 fir 48 h are shown. The failure of lipids to sediment is an indication of their removal from bilayers to form micelle-like structures. No significant lipids were detected in the supernatant of samples from 7:3 POPC/POPS LUVs (light gray), in agreement with the dye leakage assay (Fig. 1). Results are the average of three independent measurements and error bars represent their standard deviation. Black bars indicate controls without peptide.

The formation of small micelle-like lipid structures that are characteristic of a detergent-like mechanism can also be detected by using ^{31}P solid-state NMR (34,61). Fig. 2.7 shows the ^{31}P spectra obtained for POPC/POPS and POPC/POPS/Ganglioside LUVs before and after the

addition of Aβ40. In each experiment, a ^{31}P spectrum of the LUVs was collected before and after the addition of Aβ40. In the absence of Aβ40, both samples show resonances around -13 ppm and -17 ppm originating from PS-rich and PC-rich lipids in the flat lamellar phases, respectively. An isotropic peak suggesting the formation of small micelle-like lipidic structures appears only in the sample containing ganglioside 10 hours after the addition of Aβ40 (Fig. 2.7B). The corresponding POPC/POPS LUV sample does not show an isotropic peak (Fig. 2.7A), matching the results of the sedimentation assay (Fig. 2.6).

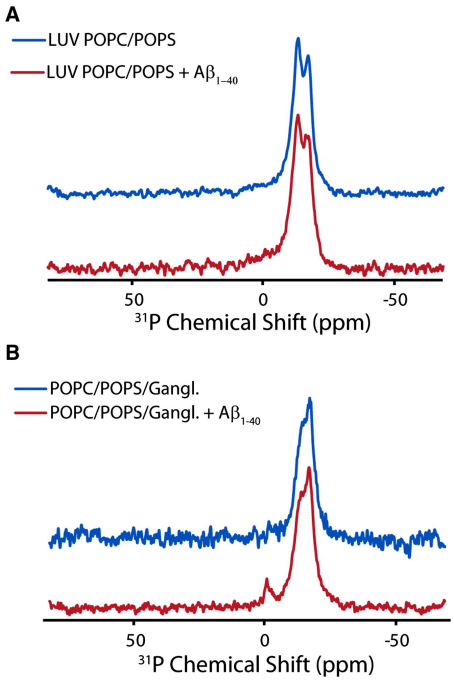

Figure 2.7 ^{31}P solid-state NMR of LUVs incubated with Aβ40.
^{31}P chemical shift spectra of LUVs composed 7:3 POPC/POPS (A) and 5.5:3:1.5 POPC/POPS/gangliosides (B) before (blue) and after the additionf of Aβ40 (red) are illustrated. The small peak near 0 ppm in the ganglioside containing spectra indicates the formation of small, rapidly tumbling lipid structures indicative of membrane fragmentation. The absence of a corresponding peak for samples without ganglioside is an indication that membrane fragmentation does not occur. All spectra were obtained at 37 ºC and referenced with respect to 85% H_3PO_4 at 0.0 ppm.

2.2.5. Paramagnetic quenching NMR experiments suggest that pores disappear after fiber formation.

To test for the integrity of the membrane after fiber formation is complete we employed paramagnetic quenching NMR experiments. Paramagnetic quenching experiments reveal the exposure of the lipid headgroup to solvent: if a headgroup is exposed to Mn^{2+} the corresponding resonance is broadened and the intensity decreases. If the membrane is intact only the outer leaflet will be broadened, as the Mn^{2+} ions cannot pentrate into the membrane to quench the inner leaflet. If pores or other defects are present that allow Mn^{2+} to pass through the membrane, both leaflets will be broadened to some degree. Interestingly, when adding Mn^{2+} to the sample containing Aβ40 incubated for 4 days the intensity of the main resonance is reduced only by 50% (Fig. 2.8B), suggesting that only the headgroups of lipids in the outer leaflet of the bilayer are exposed to the quencher. The resonance corresponding to the isotropic phase is completely quenched, as is expected for a micelle-like structure. By contrast, the intensity of the resonances corresponding to both the lamellar and isotropic phases decrease nearly 100% after addition of the pore forming peptide MSI-78 (Fig. 2.8A). The absence of an effect of Mn^{+2} on the lamellar phase in the Aβ40 sample is an indication the membrane reseals after fiber formation without defects that allow the passage of Mn^{+2} through the membrane.

2.3. Discussion

Although it is widely accepted that disruption of the integrity of the plasma and possibly mitochondrial membranes contributes to the toxicity of amyloidogenic peptides, the mechanism underlying this process is still not completely understood. We demonstrate here that the membrane disruption caused by Aβ40 is a two-step process involving initial selective disruption of the membrane by pores followed by non-selective physical disruption during fiber formation.

A similar two-step process involving fiber-dependent and non-fiber dependent steps has been suggested for the related amyloidogenic peptide IAPP, suggesting the mechanism by which the two peptides disrupt the membrane may be similar (26,63).

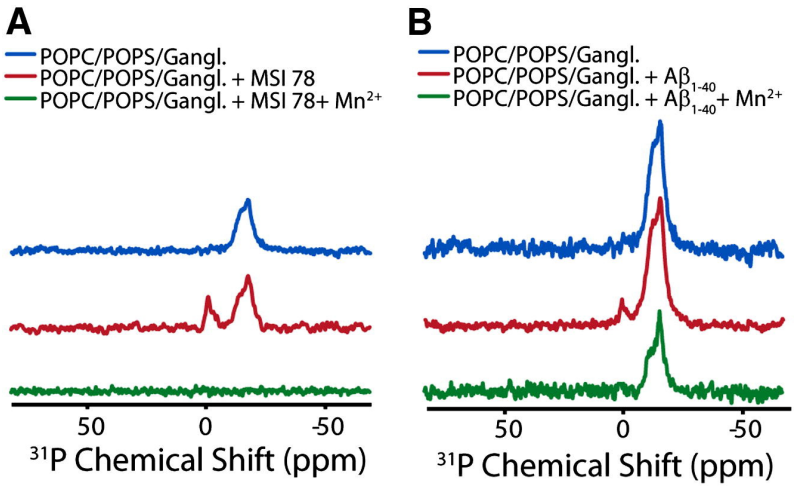

Figure 2.8 Absence of membrane defects after fiber formation as detected by paramagnetic relaxation enhancement.
(A and B) 31P chemical shift spectra of 5.5:3:1.5 POPC/POPS/gangliosides LUVs before (top), after the addition of MSI-78 (A) and Aβ40 (B) (middle), and after the addition of 500 μM Mn2+ (bottom). Mn2+ completely quenches the peaks originating from both the isotropic and lamellar phases in the MSI-78 sample; however, only does so to the isotropic peak in the Aβ40 sample, indicating the absence of membrane defects after fiber formation is complete. Aβ40 was allowed to incubate on the membrane for 4 days before acquisition. All spectra were collected at 37 ºC and referenced to 85% H_3PO_4 at 0.0 ppm.

The initial step of membrane disruption by Aβ40 in LUVs shares many properties with the channels detected by single channel recording. First, membrane disruption is detected in both cases rapidly after the addition of freshly dissolved Aβ40. In LUVs, influx of Ca^{+2} occurs immediately after the addition of Aβ40 (Fig. 2.4). This compares favorably with single channel recordings and live cell calcium imaging studies, which show the influx of Ca^{+2} can occur several minutes after the addition of Aβ40 (13,64). Second, both the channels observed in single-channel recording and the pores initially observed in LUVs are charge selective (44). In LUVs, membrane disruption is initially characterized by the influx of positively charged Ca^{2+} (Figs. 2.3

and 2.4) and not the negatively charged 6-carboxyfluorescein into the LUV (Fig. 2.1); despite their relatively similar sizes. Finally, channel activity in supported lipid bilayers and the initial phase of membrane disruption in LUVs can both be stopped by the addition of Zn^{2+} (Fig. 2.4), most likely through the interaction of Zn^{2+} with His-13 and His-14 located in the inner part of the channel (13,50,55-58). This finding suggests pores of a specific structure are likely to be involved in both experiments.

The second phase of membrane disruption is distinguished by the leakage of 6-carboxyfluorescein from the vesicles. Initially, Aβ40 proteoliposomes of all membrane compositions are impermeant to 6-carboxyfluorescein (Fig. 2.1), and leakage can only be detected after a significant lag-time in a manner reminiscent of fiber formation (Figs. 2.1 and 2.2). A direct link between fiber formation and membrane disruption is suggested by seeding experiments, which show that membrane disruption is immediately apparent after the addition of freshly dissolved Aβ40 to preformed fibers (Fig. 2.5).

While early membrane disruption in LUVs appears to share many properties with the channels detected by single channel recording, later membrane disruption differs markedly from both. First, later membrane disruption is largely non-selective for the passage of molecules. While both channels detected by electrical recording and the early phase of membrane disruption are selective for the passage of cationic molecules, the membrane becomes permeable to both negatively charged 6-carboxyfluorescein and Ca^{2+} as time progresses. The lack of selectivity in the second phase is consistent with a total loss of the physical integrity of the membrane, resulting in the appearance of small micelle-like structures as time progresses (Figs. 2.6 and 2.7). Second, membrane damage by fiber elongation is not stopped by the addition of Zn^{2+} (Fig. 2.5). If anything Zn^{2+} appears to enhance fiber dependent membrane disruption (Fig. 2.5). Finally, the

second phase is completely dependent on the presence of ganglioside. While early pore formation is enhanced in ganglioside containing membranes (Fig. 2.3), membrane fragmentation by fiber elongation cannot be observed at all in the absence of ganglioside (Figs. 2.6 and 2.7). All of these factors suggest a second process can also disrupt membranes that is not detected in channel recording, most likely due to the breakage of the membrane correlating with the formation of large membrane-bound Aβ40 oligomers (65). However, these findings are consistent with earlier ^{31}P NMR and AFM results suggesting the eventual disintegration of membranes by Aβ40 (23,34).

We cannot distinguish on the basis of our data if the two phases of membrane disruption are truly two separate and independent processes or if they are a single process with several stages. Several researchers have noted that the pores formed by Aβ40 appear to be unstable. Instead, pores formed by Aβ40 appear to be dynamic with subunits of the pore breaking off and coalescing into larger, extended, and ThT-positive aggregates (65,66). The formation of these larger aggregates is correlated with a large change in conductance that is in agreement with the start of a second phase of membrane detected in our measurements (65). Furthermore, we show that membrane disruption by Aβ40 is transient and is abolished after fiber formation is complete (Fig. 2.8), suggesting the possibility that pores are converted into fibers during the membrane disruption process that eventually detach form the membrane. Nevertheless, it is difficult to resolve this question using ensemble techniques that cannot follow individual oligomers on the membrane throughout the aggregation process.

Synthetic model membranes have the advantage of being able to simplify a complex system, enabling us to test our hypothesis under controlled conditions. Although the model membranes used here are a simplification of the complex nature of biological membranes,

our data could be useful to better understand the mechanism underlying the toxicity of Aβ peptide to neurons. For example, it would be highly interesting to test the synergistic effects of channel specific blockers such as the NA4 hexapeptide with inhibitors of fiber elongation in inhibiting Aβ (67,68). Experiments are underway to test this hypothesis.

2.4. Materials and Methods

2.4.1. Materials:

Aβ40 (97% purity) was purchased from Anaspec (Fremont, CA). 1-palmitoyl-2-oleoyl-*sn*-glycero-3-phosphocholine (POPC), 1-palmitoyl-2-oleoyl-*sn*-glycero-3-phospho-L-serine sodium salt (POPS), Total Ganglioside Extract (Brain, Porcine-Ammonium Salt), and Total Brain Lipid Extract were purchased from Avanti Polar lipids Inc. (Alabaster, AL). Ferric chloride hexahydrate, ammonium thiocyanate, and Fura-2 pentapotassium salt were purchased from Sigma-Aldrich (St.Louis, MO). 6-Carboxyfluorescein was purchased from Fluka.

2.4.2. Peptide preparation.

In order to break up any preformed aggregates, Aβ40 was initially dissolved in NH_3 $2\%_{v/v}$ at a concentration of 1 mg/ml. The peptide was then lyophilized overnight and the powder obtained was dissolved in DMSO to a final concentration of 500 μM. Stock solution of Aβ40 was used immediately after preparation.

2.4.3. Model membrane preparation.

Large unilamellar vesicles (LUV) of POPC/POPS 7/3, POPC/POPS/ganglioside 5.5/3/1.5, and total lipid brain extract (TLBE) were prepared from a chloroform solution of lipids in the desired ratio. The solution was gently dried under nitrogen flow and then placed under a high vacuum overnight to further evaporate any residual solvent. The obtained lipid film was

rehydrated with a buffer solution (10 mM phosphate buffer solution, pH 7.4, 100 mM NaCl), to yield a final concentration of 4 mg/ml, and dispersed by vigorous stirring. The resulting solution was extruded 23 times through a 100 nm polycarbonate Nucleopore membrane filter (Whatman) mounted on a mini-extruder in order to obtain LUV with an average diameter of 100 nm.

To prepare dye-filled LUV, the dry lipid film was hydrated with a buffer solution containing 6-carboxyfluorescein (10 mM phosphate buffer solution, 70 mM 6-carboxyfluorescein, 100 mM NaCl, pH 7.4) or 100 μM Fura-2 pentapotassium salt (10 mM Hepes buffer solution, 200 μM EGTA, 100 mM NaCl, pH 7.4) to a final concentration of 10 mg/ml, which was followed by the procedures described above. Removal of any non-encapsulated 6-carboxyfluorescein or Fura-2 pentapotassium salt was performed by running the extruded LUV solution through a Sephadex G50 gel exclusion column (Sigma-Aldrich) and collecting the first colored band detectable under visible or UV light which contained the separated dye-containing vesicles. The final lipid concentrations were measured using the Stewart assay. All solutions were freshly prepared before each experiment.

2.4.4. Dye leakage assay.

Membrane leakage experiments were carried out using 6-carboxyfluorescein-filled LUV composed of POPC/POPS 7/3, POPC/POPS/gangliosides 5.5/3/1.5 and total brain extract. Membrane leakage was detected by measuring the increase in fluorescence 6-carboxyfluorescein resulting from its dilution and subsequent dequenching following membrane leakage. Samples were prepared by first diluting the dye-filled vesicles solution with buffer solution (10 mM phosphate buffer solution, 100 mM NaCl, pH 7.4) to a final concentration of 0.2 mg/ml. The presence of 100 mM NaCl in the buffer ensured that the osmotic pressure exerted on the membrane bilayer by the dye itself had no effect on dye release from the vesicles. The NaCl

concentration was optimized by varying the NaCl concentration in the buffer outside the LUVs until baseline leakage in the absence of peptide was negligible over several days. To initiate membrane disruption, 1 or 2 μl of the peptide stock solution was added to 100 μl of the LUV solution to obtain a final peptide concentration of 5 or 10 μM , respectively. Experiments were carried out in Corning 96 well non-binding surface plates. Time traces were recorded using Biotek Synergy 2 plate reader using a 2 nm bandpass filters at 494 nm excitation and 520 nm emission at room temperature, shaking samples for 10 seconds before each read. The fraction of dye released was calculated by:

$$\text{Fraction of dye released} = (I - I_0)/(I_{100} - I_0)$$

where I is the emission intensity of the sample, I_0 is the emission intensity obtained in the absence of peptide (baseline control) and I_{100} is the emission intensity obtained after adding 1 μl of Triton X-100, a detergent which acted as a positive control to give 100% leakage.

2.4.5. ThT assay.

The kinetics of amyloid peptide formation were measured through increased fluorescence emission upon binding of amyloid fibers to the commonly used amyloid specific dye, thioflavin T (ThT). Samples were prepared by adding 1 or 2 μl of the peptide stock solution to 100 μl of the 10 mM phosphate buffer solution (100 mM NaCl, pH 7.4 containing 10 μM ThT) containing 0.2 mg/mL LUV prepared in the same manner as above, to yield a final peptide concentration of 5 or 10 μM, respectively. Experiments were carried out in Corning 96 well nonbinding surface plates as detailed for the 6-carboxyfluorescein assay using a 440 nm excitation filter and a 485 nm emission filter.

2.4.6. Fura-2 assay.

The presence of cation or size selective pores was detected by measuring changes in the 340/380 nm excitation ratio upon binding of Ca^{+2} or Zn^{+2} to the cation sensitive dye Fura-2 encapsulated within the LUVs. Samples were prepared by first diluting the Fura-2 dye-filled vesicles solution with buffer solution (10 mM Hepes buffer solution, 100 μM Fura-2 pentapotassium salt, 200 μM EGTA, 100 mM NaCl, pH 7.4) to a final concentration of 0.2 mg/ml. Then, Aβ40 was added with a final concentration of 5 μM or 10 μM. Fluorescence was measured at 340 and 380 nm with slits set for 10 nm bandwidths to obtain the baseline. After 10 minutes, 500 μM of Ca^{+2} or Zn^{+2} was added to the sample and changes in the 340/380 ratio were recorded. Samples with MSI-78, an antimicrobial peptide that is known to strongly disrupt membranes, were also run as a positive control.

2.4.7. Lipid sedimentation assay.

The presence of micelle formation was detected measurement of lipid concentration in the supernatant following sedimentation of 1000 nm LUVs by centrifugation.Solutions of POPC/POPS 7/3, POPC/POPS/Ganglioside 5.5/4/1.5, and total brain extract LUV and final concentration of 1 mg/ml were prepared as described above except extrusion was performed through 1000 nm membranes. 20 μM Aβ40 was first incubated with 250 μl of the LUV solution for 2 days in order to form amyloid fibers. Following incubation with Aβ40, samples were then centrifuged for 40 minutes at 14000 rpm and the supernatant, which contained any micelles, was collected, diluted in 1 ml of chloroform, and treated as described below in order to measure the lipid concentration in solution. Solutions without $A\beta_{-40}$ were set as controls.

Lipid concentrations in the supernatant were detected via the Stewart assay, a colorimetric technique based on the ability of phospholipids to form a complex with ammonium

ferrothiocyanate. Initially, a calibration curve was created for each LUV lipid composition. A series of chloroform solutions with known concentrations of lipids (each solution 1 ml) were prepared and treated with 1 ml of a solution containing ferric chloride and ammonium thiocyanate. Each solution was vortexed for 20 seconds and the organic phase collected. The optical density of these standard solutions was at 461 nm and plotted versus the known lipid concentration and used as a calibration curve to determine the lipid concentrations in the supernatant.

2.4.8. ^{31}P solid state NMR.

All of the experiments were performed on a Varian Infinity 400 MHz solid-state NMR spectrometer operating at resonance frequencies of 400.139 MHz and 161.976 MHz for ^{1}H and ^{31}P nuclei, respectively. A 5 mm double-resonance MAS probe was used for experiments on LUVs under static conditions. A Varian temperature control unit was used to maintain the sample temperature at 37 ^{o}C. All the ^{31}P spectra were collected using a spin echo sequence (90^{o}-delay-180^{o} with 60 μs delay) and 25 kHz RF field for TPPM decoupling of protons. A typical 90^{o} pulse length of 5 μs was used with a recycle delay of 3 seconds. The ^{31}P chemical shift spectra are referenced with respect to 85% H_3PO_4 at 0 ppm. In each experiment, the ^{31}P spectrum of 200 μL LUVs composed of 4 mg POPC/POPS or POPC/POPS/Ganglioside was first collected in a 5 mm NMR tube. Following the acquisition of the control spectrum without peptide, 20 μL of 0.3 mg/ml Aβ40 or 0.1 mg/ml MSI-78 was added into the same NMR tube and acquisition immediately repeated to obtain the spectra of the membrane in the presence of 0.5 wt % MSI-78 or 1.6 wt % Aβ40. Each spectra is composed of 25000 scans for a total acquisition time of 21 hours. Aβ40 was then allowed to incubate on the membrane for three days before 500 μM $MnCl_2$ was added for the paramagnetic quenching experiments.

2.5. Acknowledgements and contributions

In the adapted portions of this chapter from Sciacca, M.F.M. et al, (2012) *Biophys J.*, 103(4), 702-710:

This research was supported by funds from the NIH (GM095640 to A.R.) D.K.L. was partly supported by the Basic Science Research Program through the National Research Foundation of Korea, fund by the Ministry of Education, Science, and Technology (2009-0087836).

M.F.M.S., S.A.K., J.C., J.R.B., and A.R. performed fluorescence experiments and analyzed fluorescence results. D.K.L., M.F.M.S., J.R.B. and A.R. performed NMR experiments and analyzed NMR results. All authors in this publication analyzed all results. M.F.M.S., S.A.K., J.R.B., and A.R. wrote the publication and A.R. directed the research. All authors reviewed and edited the published article.

2.6. References

1. Hardy, J. A., and Higgins, G. A. (1992) Alzheimer's disease: the amyloid cascade hypothesis. *Science* **256**, 184-185

2. Demuro, A., Mina, E., Kayed, R., Milton, S. C., Parker, I., and Glabe, C. G. (2005) Calcium dysregulation and membrane disruption as a ubiquitous neurotoxic mechanism of soluble amyloid oligomers. *J Biol Chem* **280**, 17294-17300

3. Benilova, I., Karran, E., and De Strooper, B. (2012) The toxic A beta oligomer and Alzheimer's disease: an emperor in need of clothes. *Nat. Neurosci.* **15**, 349-357

4. Small, D. H. (2009) Dysregulation of Calcium Homeostasis in Alzheimer's Disease. *Neurochem. Res.* **34**, 1824-1829

5. Mattson, M. P., Cheng, B., Davis, D., Bryant, K., Lieberburg, I., and Rydel, R. E. (1992) Beta-Amyloid Peptides Destabilize Calcium Homeostasis and Render Human Cortical-Neurons Vulnerable to Excitotoxicity. *J. Neurosci.* **12**, 376-389

6. Pollard, H. B., Arispe, N., and Rojas, E. (1995) Ion channel hypothesis for Alzheimer amyloid peptide neurotoxicity. *Cell. Mol. Neurobiol.* **15**, 513-526

7. Pollard, H. B., Rojas, E., and Arispe, N. (1993) A New Hypothesis for the Mechanism of Amyloid Toxicity, Based on the Calcium-Channel Activity of Amyloid-Beta Protein (a-Beta-P) in Phospholipid-Bilayer Membranes. *Alzheimers Disease: Amyloid Precusor Proteins, Signal Transduction, and Neuronal Transplantation* **695**, 165-168

8. Lal, R., Lin, H., and Quist, A. P. (2007) Amyloid beta ion channel: 3D structure and relevance to amyloid channel paradigm. *Biochim. Biophys. Acta* **1768**, 1966-1975

9. Quist, A., Doudevski, L., Lin, H., Azimova, R., Ng, D., Frangione, B., Kagan, B., Ghiso, J., and Lal, R. (2005) Amyloid ion channels: A common structural link for protein-misfolding disease. *Proc. Natl. Acad. Sci. U. S. A.* **102**, 10427-10432

10. Demuro, A., Parker, I., and Stutzmann, G. E. (2010) Calcium Signaling and Amyloid Toxicity in Alzheimer Disease. *J. Biol. Chem.* **285**, 12463-12468

11. Capone, R., Quiroz, F. G., Prangkio, P., Saluja, I., Sauer, A. M., Bautista, M. R., Turner, R. S., and Mayer, M. (2008) Amyloid-beta Ion Channels in Artificial Lipid Bilayers and Neuronal Cells. *Neurotoxicity Research* **15**, 608-650

12. Capone, R., Jang, H., Kotler, S. A., Connelly, L., Arce, F. T., Ramachandran, S., Kagan, B. L., Nussinov, R., and Lal, R. (2012) All-D-Enantiomer of beta-Amyloid Peptide Forms Ion Channels in Lipid Bilayers. *Journal of Chemical Theory and Computation* **8**, 1143-1152

13. Capone, R., Quiroz, F. G., Prangkio, P., Saluja, I., Sauer, A. M., Bautista, M. R., Turner, R. S., Yang, J., and Mayer, M. (2009) Amyloid-beta-Induced Ion Flux in Artificial Lipid Bilayers and Neuronal Cells: Resolving a Controversy. *Neurotoxicity Research* **16**, 1-13

14. Arispe, N., Rojas, E., and Pollard, H. B. (1993) Alzheimer-Disease Amyloid Beta-Protein Forms Calcium Channels in Bilayer-Membranes - Blockade by Tromethamine and Aluminum. *Proc. Natl. Acad. Sci. U. S. A.* **90**, 567-571

15. Diaz, J. C., Simakova, O., Jacobson, K. A., Arispe, N., and Pollard, H. B. (2009) Small molecule blockers of the Alzheimer A beta calcium channel potently protect neurons from A beta cytotoxicity. *Proc. Natl. Acad. Sci. U. S. A.* **106**, 3348-3353

16. Hirakura, Y., Yiu, W. W., Yamamoto, A., and Kagan, B. L. (2000) Amyloid peptide channels: blockade by zinc and inhibition by Congo red (amyloid channel block). *Amyloid* **7**, 194-199

17. Lin, H., Zhu, Y. W. J., and Lal, R. (1999) Amyloid beta protein (1-40) forms calcium-permeable, Zn2+-sensitive channel in reconstituted lipid vesicles. *Biochemistry* **38**, 11189-11196

18. Chimon, S., Shaibat, M. A., Jones, C. R., Calero, D. C., Aizezi, B., and Ishii, Y. (2007) Evidence of fibril-like beta-sheet structures in a neurotoxic amyloid intermediate of Alzheimer's beta-amyloid. *Nat. Struct. Mol. Biol.* **14**, 1157-1164

19. Hoshi, M., Sato, M., Matsumoto, S., Noguchi, A., Yasutake, K., Yoshida, N., and Sato, K. (2003) Spherical aggregates of beta-amyloid (amylospheroid) show high neurotoxicity and activate tau protein kinase I/glycogen synthase kinase-3 beta. *Proc. Natl. Acad. Sci. U. S. A.* **100**, 6370-6375

20. Solomonov, I., Korkotian, E., Born, B., Feldman, Y., Bitler, A., Rahimi, F., Li, H., Bitan, G., and Sagi, I. Zn2+-Abeta40 complexes form metastable quasi-spherical oligomers that are cytotoxic to cultured hippocampal neurons. *J. Biol. Chem.*

21. Morita, M., Vestergaard, M., Hamada, T., and Takagi, M. (2010) Real-time observation of model membrane dynamics induced by Alzheimer's amyloid beta. *Biophys. Chem.* **147**, 81-86

22. Michikawa, M., Gong, J. S., Fan, Q. W., Sawamura, N., and Yanagisawa, K. (2001) A novel action of Alzheimer's amyloid beta-protein (A beta): Oligomeric A beta promotes lipid release. *J. Neurosci.* **21**, 7226-7235

23. Yip, C. M., and McLaurin, J. (2001) Amyloid-beta peptide assembly: A critical step in fibrillogenesis and membrane disruption. *Biophys. J.* **80**, 1359-1371

24. Williams, T. L., Johnson, B. R., Urbanc, B., Jenkins, A. T., Connell, S. D., and Serpell, L. C. (2011) Abeta42 oligomers, but not fibrils, simultaneously bind to and cause damage to ganglioside-containing lipid membranes. *Biochem J* **439**, 67-77

25. Ikeda, K., Yamaguchi, T., Fukunaga, S., Hoshino, M., and Matsuzaki, K. (2011) Mechanism of amyloid beta-protein aggregation mediated by GM1 ganglioside clusters. *Biochemistry-Us* **50**, 6433-6440

26. Brender, J. R., Lee, E. L., Hartman, K., Wong, P. T., Ramamoorthy, A., Steel, D. G., and Gafni, A. (2011) Biphasic effects of insulin on islet amyloid polypeptide membrane disruption. *Biophys. J.* **100**, 685-692

27. McLaurin, J., and Chakrabartty, A. (1996) Membrane disruption by Alzheimer beta-amyloid peptides mediated through specific finding to either phospholipids or gangliosides - Implications for neurotoxicity. *J Biol Chem* **271**, 26482-26489

28. Wong, P. T., Schauerte, J. A., Wisser, K. C., Ding, H., Lee, E. L., Steel, D. G., and Gafni, A. (2009) Amyloid-beta membrane binding and permeabilization are distinct processes influenced separately by membrane charge and fluidity. *J. Mol. Biol.* **386**, 81-96

29. Gauci, A. J., Caruana, M., Giese, A., Scerri, C., and Vassallo, N. (2011) Identification of Polyphenolic Compounds and Black Tea Extract as Potent Inhibitors of Lipid Membrane Destabilization by A beta(42) Aggregates. *J Alzheimers Dis* **27**, 767-779

30. Matsuzaki, K. (2007) Physicochemical interactions of amyloid beta-peptide with lipid bilayers. *Biochim. Biophys. Acta* **1768**, 1935-1942

31. Sani, M. A., Gehman, J. D., and Separovic, F. (2011) Lipid matrix plays a role in Abeta fibril kinetics and morphology. *FEBS Lett.* **585**, 749-754

32. Ikeda, K., and Matsuzaki, K. (2008) Driving force of binding of amyloid beta-protein to lipid bilayers. *Biochem. Biophys. Res. Commun.* **370**, 525-529

33. Chi, E. Y., Frey, S. L., and Lee, K. Y. C. (2007) Ganglioside G(M1)-mediated amyloid-beta fibrillogenesis and membrane disruption. *Biochemistry* **46**, 1913-1924

34. Nakazawa, Y., Suzuki, Y., Williamson, M. P., Saito, H., and Asakura, T. (2009) The interaction of amyloid A beta(1-40) with lipid bilayers and ganglioside as studied by P-31 solid-state NMR. *Chem. Phys. Lipids* **158**, 54-60

35. Williams, T. L., Johnson, B. R. G., Urbanc, B., Jenkins, A. T. A., Connell, S. D. A., and Serpell, L. C. (2011) A beta 42 oligomers, but not fibrils, simultaneously bind to and cause damage to ganglioside-containing lipid membranes. *Biochem. J.* **439**, 67-77

36. Okada, T., Ikeda, K., Wakabayashi, M., Ogawa, M., and Matsuzaki, K. (2008) Formation of toxic A beta(1-40) fibrils on GM1 ganglioside-containing membranes mimicking lipid rafts: Polymorphisms in A beta(1-40) fibrils. *J Mol Biol* **382**, 1066-1074

37. Wakabayashi, M., and Matsuzaki, K. (2009) Ganglioside-induced amyloid formation by human islet amyloid polypeptide in lipid rafts. *Febs Lett* **583**, 2854-2858

38. Matsuzaki, K., Kato, K., and Yanagisawa, K. (2010) Abeta polymerization through interaction with membrane gangliosides. *Biochim Biophys Acta* **1801**, 868-877

39. Matsuzaki, K. (2011) Formation of Toxic Amyloid Fibrils by Amyloid beta-Protein on Ganglioside Clusters. *Int J Alzheimers Dis* **2011**, 956104

40. Ogawa, M., Tsukuda, M., Yamaguchi, T., Ikeda, K., Okada, T., Yano, Y., Hoshino, M., and Matsuzaki, K. (2011) Ganglioside-mediated aggregation of amyloid beta-proteins (A beta): comparison between A beta-(1-42) and A beta-(1-40). *J Neurochem* **116**, 851-857

41. Yanagisawa, K. (2005) GM1 ganglioside and the seeding of amyloid in Alzheimer's disease: Endogenous seed for alzheimer amyloid. *Neuroscientist* **11**, 250-260

42. Inoue, S. (2008) In situ A beta pores in AD brain are cylindrical assembly of A beta protofilaments. *Amyloid* **15**, 223-233

43. Jang, H., Arce, F. T., Ramachandran, S., Capone, R., Lal, R., and Nussinov, R. (2010) beta-Barrel Topology of Alzheimer's beta-Amyloid Ion Channels. *J Mol Biol* **404**, 917-934

44. Kagan, B. L., and Thundimadathil, J. (2010) Amyloid Peptide Pores and the Beta Sheet Conformation. *Proteins: Membrane Binding and Pore Formation* **677**, 150-167

45. Kayed, R., Pensalfini, A., Margol, L., Sokolov, Y., Sarsoza, F., Head, E., Hall, J., and Glabe, C. (2009) Annular Protofibrils Are a Structurally and Functionally Distinct Type of Amyloid Oligomer. *J Biol Chem* **284**, 4230-4237

46. Small, D. H., Gasperini, R., Vincent, A. J., Hung, A. C., and Foa, L. (2009) The Role of A beta-Induced Calcium Dysregulation in the Pathogenesis of Alzheimer's Disease. *J Alzheimers Dis* **16**, 225-233

47. McLean, C. A., Cherny, R. A., Fraser, F. W., Fuller, S. J., Smith, M. J., Beyreuther, K., Bush, A. I., and Masters, C. L. (1999) Soluble pool of A beta amyloid as a determinant of severity of neurodegeneration in Alzheimer's disease. *Annals of Neurology* **46**, 860-866

48. Lue, L. F., Kuo, Y. M., Roher, A. E., Brachova, L., Shen, Y., Sue, L., Beach, T., Kurth, J. H., Rydel, R. E., and Rogers, J. (1999) Soluble amyloid beta peptide concentration as a predictor of synaptic change in Alzheimer's disease. *American Journal of Pathology* **155**, 853-862

49. Arispe, N., Pollard, H. B., and Rojas, E. (1993) Giant multilevel cation channels formed by Alzheimer disease amyloid beta-protein [A beta P-(1-40)] in bilayer membranes. *Proc Natl Acad Sci U S A* **90**, 10573-10577

50. Arispe, N., Pollard, H. B., and Rojas, E. (1996) Zn2+ interaction with Alzheimer amyloid beta protein calcium channels. *Proceedings of the National Academy of Sciences of the United States of America* **93**, 1710-1715

51. Durell, S. R., Guy, H. R., Arispe, N., Rojas, E., and Pollard, H. B. (1994) Theoretical-Models of the Ion-Channel Structure of Amyloid Beta-Protein. *Biophys J* **67**, 2137-2145

52. Corti, H. R., Frank, G. A., and Marconi, M. C. (2008) An Alternate Solution of Fluorescence Recovery Kinetics after Spot-Bleaching for Measuring Diffusion Coefficients. 2. Diffusion of Fluorescein in Aqueous Sucrose Solutions. *J. Solution Chem.* **37**, 1593-1608

53. Maroudas, A., Weinberg, P. D., Parker, K. H., and Winlove, C. P. (1988) The Distributions and Diffusivities of Small Ions in Chondroitin Sulfate, Hyaluronate and Some Proteoglycan Solutions. *Biophys. Chem.* **32**, 257-270

54. Hallock, K. J., Lee, D. K., and Ramamoorthy, A. (2003) MSI-78, an analogue of the magainin antimicrobial peptides, disrupts lipid bilayer structure via positive curvature strain. *Biophys. J.* **84**, 3052-3060

55. Capone, R., Jang, H., Kotler, S. A., Kagan, B. L., Nussinov, R., and Lal, R. (2012) Probing structural features of Alzheimer's amyloid-beta pores in bilayers using site-specific amino acid substitutions. *Biochemistry-Us* **51**, 776-785

56. Hirakura, Y., Lin, M. C., and Kagan, B. L. (1999) Alzheimer amyloid abeta1-42 channels: effects of solvent, pH, and Congo Red. *J Neurosci Res* **57**, 458-466

57. Kawahara, M., Arispe, N., Kuroda, Y., and Rojas, E. (1997) Alzheimer's disease amyloid beta-protein forms Zn2+-sensitive, cation-selective channels across excised membrane patches from hypothalamic neurons. *Biophys J* **73**, 67-75

58. Diaz, J. C., Linnehan, J., Pollard, H., and Arispe, N. (2006) Histidines 13 and 14 in the A beta sequence are targets for inhibition of Alzheimer's disease A beta ion channel and cytotoxicity. *Biol Res* **39**, 447-460

59. Grynkiewicz, G., Poenie, M., and Tsien, R. Y. (1985) A New Generation of Ca-2+ Indicators with Greatly Improved Fluorescence Properties. *J. Biol. Chem.* **260**, 3440-3450

60. Sparr, E., Engel, M. F., Sakharov, D. V., Sprong, M., Jacobs, J., de Kruijff, B., Hoppener, J. W., and Killian, J. A. (2004) Islet amyloid polypeptide-induced membrane leakage involves uptake of lipids by forming amyloid fibers. *Febs Lett* **577**, 117-120

61. Brender, J. R., Durr, U. H. N., Heyl, D., Budarapu, M. B., and Ramamoorthy, A. (2007) Membrane fragmentation by an amyloidogenic fragment of human Islet Amyloid Polypeptide detected by solid-state NMR spectroscopy of membrane nanotubes. *Biochimica Et Biophysica Acta-Biomembranes* **1768**, 2026-2029

62. Stewart, J. C. M. (1980) Colorimetric Determination of Phospholipids with Ammonium Ferrothiocyanate. *Analytical Biochemistry* **104**, 10-14

63. Engel, M. F., Khemtemourian, L., Kleijer, C. C., Meeldijk, H. J., Jacobs, J., Verkleij, A. J., de Kruijff, B., Killian, J. A., and Hoppener, J. W. (2008) Membrane damage by human islet amyloid polypeptide through fibril growth at the membrane. *Proc. Natl. Acad. Sci. U. S. A.* **105**, 6033-6038

64. Simakova, O., and Arispe, N. J. (2006) Early and late cytotoxic effects of external application of the Alzheimer's A beta result from the initial formation and function of A beta ion channels. *Biochemistry* **45**, 5907-5915

65. Schauerte, J. A., Wong, P. T., Wisser, K. C., Ding, H., Steel, D. G., and Gafni, A. (2010) Simultaneous Single-Molecule Fluorescence and Conductivity Studies Reveal Distinct Classes of Abeta Species on Lipid Bilayers. *Biochemistry*

66. Jang, H., Arce, F. T., Capone, R., Ramachandran, S., Lal, R., and Nussinov, R. (2009) Misfolded Amyloid Ion Channels Present Mobile beta-Sheet Subunits in Contrast to Conventional Ion Channels. *Biophys. J.* **97**, 3029-3037

67. Arispe, N., Diaz, J. C., and Simakova, O. (2007) A beta ion channels. Prospects for treating Alzheimer's disease with A beta channel blockers. *Biochim. Biophys. Acta* **1768**, 1952-1965

68. Butterfield, S., Hejjaoui, M., Fauvet, B., Awad, L., and Lashuel, H. A. Chemical Strategies for Controlling Protein Folding and Elucidating the Molecular Mechanisms of Amyloid Formation and Toxicity. *J. Mol. Biol.*

Chapter 3: Characterizing Structural Features of Amyloid-β Oligomers Through Combined Approaches in Solution- and Solid-State NMR

This chapter was adapted from the following publication:

Kotler, S.A., Brender, J.R., Vivekanandan, S., Suzuki, Y., Yamamoto, K., Krishnamoorthy, J., Walsh, P., Cauble, M., Monette, M., Banaszak Holl, M.M., Marsh, E.N.G., and Ramamoorthy, A. (2015) High-resolution NMR characterization of low abundance oligomer of amyloid-β without purification. *Scientific Reports*, **5**, 11811; doi: 10.1038/srep11811.

3.1. Introduction

Alzheimer's disease (AD) is a fatal neurological disorder affecting more than five million people in the United States today; a figure that is expected to increase three-fold by 2050 if therapeutics remain inadequate (1). Although the exact cause of AD remains undetermined, many signs point to the involvement of the aggregation of the amyloid-β (Aβ) peptide at some stage (2, 3). The aggregation of Aβ leads to the formation of senile plaques found in patients with AD, the main constituent of which is the Aβ peptide in its fibrillar form (4). However, attempts at pharmaceutical intervention aimed at targeting Aβ aggregation has been complicated by the myriad forms that aggregates of Aβ can adopt, many of which remain poorly characterized (3, 5, 6).

Much effort has been undertaken in the way of understanding the structural details of the monomeric (7–9) and fibrillar (10–13) forms of Aβ both computationally and experimentally; however, there are only few existing structural models of the intermediates formed along the

misfolding pathway of Aβ (14–17). Unfortunately, these are the species currently believed to be most critical for pathogenesis in Alzheimer's and other amyloid related neurodegenerative diseases (3). Most of the models that do exist bear a close structural resemblance to the fiber end-product (15, 18–20), with few exceptions (21). However, considerable evidence from lower-resolution techniques like CD suggests some (but not all) of the most toxic oligomers may have a considerably different structure that may be closer to the Aβ monomer than the Aβ fiber (22–25).

The transient nature and high heterogeneity of amyloid oligomers present significant challenges for high-resolution structural studies. Oligomers of a specific conformation are difficult to isolate, which has thus far severely limited high-resolution characterization of Aβ. Moreover, oligomer structures of Aβ40 and Aβ42 have not been obtained by crystallography (only a low resolution structure of a specific Aβ oligomer obtained by powder X-ray diffraction and modeling exists) (26), nor have they been obtained for oligomers of other amyloidogenic proteins, except for αB-crystallin (27).

Previous studies have shown Aβ40's ability to form unordered, globular aggregates with little to no secondary structure (22, 24, 25, 28). Not only are these oligomers a critical step in the aggregation of Aβ, but they also exhibit a high degree of cytotoxicity (22, 24, 25). A time dependent ^{19}F NMR study showed that such oligomers can persist even after prolonged incubation (>50 days) and the formation of amyloid fibrils (29); however, none of these studies demonstrated structural details beyond low-resolution measurements. To characterize the disordered globular oligomers, we chose experimental conditions similar to these previous studies using low salt concentrations and neutral pH, yet here we also apply agitation during seeded fibrillization. This method of preparation results in the formation of an aggregated Aβ sample comprised mostly of fibrils with a small population of a predominantly disordered

oligomeric species of Aβ40. Remarkably, this method of preparation yielded disordered oligomers reproducibly at almost 10% of the total peptide concentration without perturbative methods, such as chemical- or photo-crosslinking, freezing, amino acid substitution, or any other type of protein engineering to stabilize the oligomer.

Using magic angle spinning (MAS) NMR spectroscopy on these samples, we are able to resolve structural details otherwise unobservable by other biophysical measurements. We do so by bridging the gap in the limitations imposed on solution- and solid-state NMR methods; a molecular weight limit in solution NMR and problems with sensitivity in solid-state NMR. These limitations are overcome by taking advantage of both solution- and solid-state NMR techniques: performing solid-state NMR experiments on a liquid sample with "solid" characteristics. A similar approach was taken with a solution sample of Aβ by monitoring the formation and kinetics of large aggregates sedimenting out of solution (30). However, this technique used ^{13}C detection requiring large amounts of sample and expensive, isotopic labeling.

Here, we employ a RFDR (radio frequency driven dipolar recoupling)-based 2D $^{1}H/^{1}H$ chemical shift correlation experiment to overcome these limitations (31). High-resolution structural features of high molecular weight oligomers are difficult to characterize directly by solution NMR; however, the RFDR-based 2D $^{1}H/^{1}H$ experiment enables the specific detection of this oligomeric species over fibrillar and monomeric Aβ40 due to the line-narrowing afforded by slow MAS and the reintroduction of residual $^{1}H/^{1}H$ dipolar couplings by RFDR. Previously, the applicability of RFDR for the study of such "soft" solid systems was used to investigate the structural and motional characteristics of a resin-bound peptide (32), a micelle-associated cytochrome b5 (33), and membrane-bound peptides (34–36). Here, we demonstrate the utility of $^{1}H/^{1}H$ RFDR for the specific structural characterization of a minority population of a stable,

disordered Aβ40 oligomer containing sparse secondary structure, at low abundance, directly from an unlabeled sample in coexistence with amyloid fibrils without further purification or filtration. To the best of our knowledge, this is the first instance in which $^{1}H/^{1}H$ dipolar couplings have been used for structural studies of an amyloid oligomer, which may provide a general method to study intermediate size oligomers of the type believed to play a crucial role in amyloid pathology (3).

3.2. Results and Discussion

Aβ40 can form a disordered oligomer in parallel with β-sheet fibrils. Since intermediate size (<100 kDa) oligomers have been a prime target of both pharmaceutical and scientific research (3), we first sought to find a condition that allowed the reproducible generation of oligomers of this type. Our previous study utilizing real-time observation of a single-site ^{19}F-label at the Met-35 of Aβ40, found that Aβ40 oligomers are observed and stabilized well into the late stages of the aggregation process (29). In agreement with Suzuki et al, we find the coexistence of oligomers and fibers in our samples; however, the oligomers formed under our shaking conditions are not of the β-sheet type. A CD spectrum (Fig. 3.1a, solid) shows an intensity minimum at 225 nm indicating the bulk sample is predominantly β-sheet. Using size-cutoff filtration with a Spin-X 0.22 μm filter, we could isolate the oligomers and any residual monomers from the fibrils of Aβ40. A noticeably different CD spectrum is apparent in the filtrate, which shows a strong minimum near 198 nm indicative of a predominantly disordered structure (Fig. 3.1a, blue) very similar to that of early aggregation states of Aβ (Fig. 3.1a, red). We further confirmed the lack of β-sheet content of the filtered Aβ40 oligomers using the amyloid-specific dye, ThT (Fig. 3.1b). Similar to the freshly dissolved Aβ40 sample, the oligomers isolated by spin-X filtration display essentially no fluorescence in its ThT emission

profile, indicating a β-sheet conformation is not present (Fig. 3.1b). Conversely, an intense ThT signal is present in the isolated fibril fraction. Measuring the concentration of the spin-X filtrate by the bicinchoninic acid (BCA) protein concentration assay (Thermo Scientific) revealed 17.0 ± 6.0 μM or only 7.3+2.6% of the total Aβ40 concentration (231 μM) was not fibrillar. Together, the ThT, CD, and BCA results confirm the sample primarily consists of amyloid fibrils with a minority population of a largely disordered, relatively low MW species.

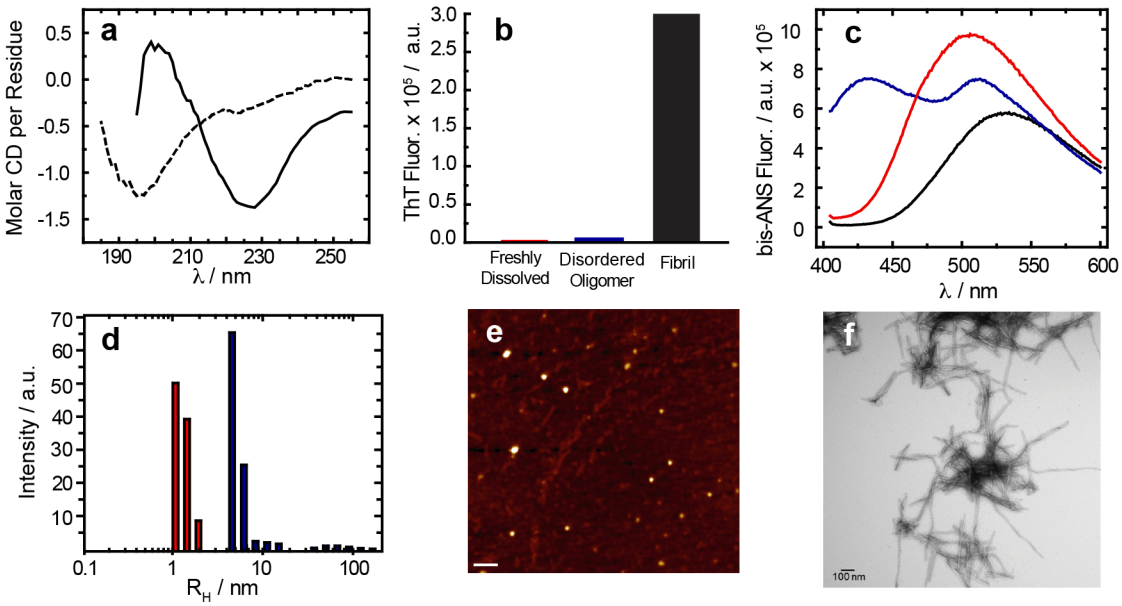

Figure 3.1 Biophysical characterization of Aβ40 disordered oligomers.
(a) CD spectra, (b) ThT fluorescence, and (c) bis-ANS fluorescence of fibrillar (black), the spin-X isolated oligomer (blue), and freshly dissolved (red) samples of Aβ40. In panel c, the emission spectrum of bis-ANS in solution is shown in gray. (d) Distributions of hydrodynamic radii of freshly dissolved Aβ40 (red) and spin-X-isolated Aβ40 oligomers (blue) determined by DLS. Representative AFM and TEM images of the oligomers (e) and fibrils (f), respectively. Scale bars in both images are 100 nm. All experiments were performed in 10 mM phosphate buffer, pH 7.4, at 25 ºC.

Since the CD spectra of the spin-X filtrate resemble CD spectra of monomeric Aβ, it is possible that the filtered sample consists of residual monomeric Aβ40. We first tested this possibility with the molecular probe 4,4'-Dianilino-1,1'-Binaphthyl-5,5'-Disulfonic Acid (bis-ANS). The spectral properties and the quantum yield of bis-ANS are highly sensitive to

polarity, thus upon binding to hydrophobic surfaces bis-ANS becomes appreciably more fluorescent. A unique feature of bis-ANS is its ability to selectively identify different aggregation states of Aβ40 through distinct emission spectra (Fig. 3.1c) (22, 37, 38). The emission spectra of bis-ANS after isolation and separation of the fibrils from disordered oligomers is shown in Fig. 3.1c, along with the bis-ANS signal from a freshly dissolved Aβ40 sample prepared without incubation or seeding. The emission spectrum of bis-ANS in the spin-X-isolated oligomers (Fig. 1c, blue) is significantly more blue-shifted than that of the emission spectrum observed from the fibril fraction (Fig. B.1). Also in Fig. 3.1c, the bis-ANS fluorescence observed in the presence of the freshly dissolved Aβ40 sample (red) is only slightly blue-shifted from that of the spectrum of bis-ANS alone (black), indicating limited binding of bis-ANS to monomeric Aβ40 and a significant difference in the hydrophobic exposure compared to the freshly dissolved Aβ40 or the Aβ40 fibrils.

In addition to the bis-ANS measurements, dynamic light scattering (DLS) studies revealed distinct size distributions of these disordered Aβ oligomers when compared to the freshly dissolved Aβ40 sample (Fig. 3.1d and Supplementary Fig. B.2). DLS measured a R_H of ~5.1 nm with a polydispersity of 32.2% for the oligomers isolated by spin-X filtration, whereas the R_H of the freshly dissolved Aβ40 sample was ~1.4 nm with a polydispersity of 19.0%. To complement our optical spectroscopy data, representative electron micrographs and AFM images of the amyloid preparations showed oligomeric and fibrillar forms present in the aggregated sample of Aβ40 (Fig. 3.1e-f). All AFM images showed the disordered Aβ oligomers exhibit an amorphous, spherical morphology (Fig. 3.1e). The oligomers were found present among a dense fibrillar network whose bundled, twisted features were apparent in all electron micrographs as observed in Fig. 3.1f. Taken together, all biophysical measurements point to the existence of a

disordered and soluble Aβ40 oligomer coexisting as a minority population amongst Aβ40 fibrils. This finding is very intriguing as it indicates Aβ40 is simultaneously undergoing β-sheet and non-β-sheet aggregation pathways. For this reason, we aimed to find distinct structural features that contributed to the formation of such an Aβ oligomer.

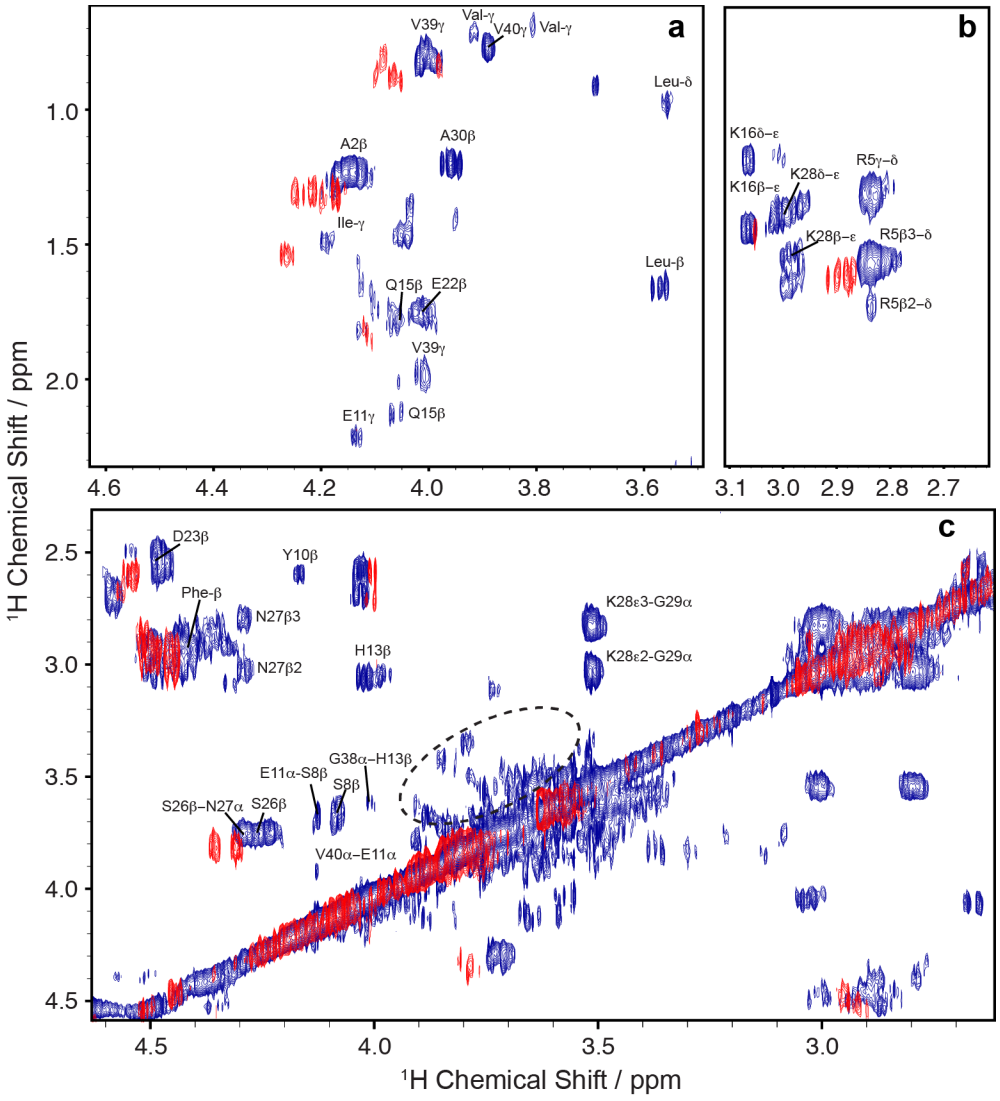

Figure 3.2 RFDR-based 2D $^{1}H/^{1}H$ chemical shift correlation spectra on solution samples of freshly dissolved (red) and aggregated (blue) forms of Aβ40.
(a) Side-chain to Hα, (b) side-chain, and (c) Hβ-Hα and Hα -Hα regions of the overlaid 2D spectra were recorded under 2.7 kHz MAS. The dotted circle highlights the Ser and Gly fingerprints of the aggregated Aβ40 sample. Peak assignments are given for the mixed Aβ40 sample. The spectra were acquired with a 50 ms mixing time at 600 MHz in 100% D2O, 10 mM sodium phosphate buffer, pH 7.4, and 37 °C. Total

Aβ40 concentrations for both samples were 462 μM; the estimated oligomer concentration in the aggregated sample is 35 ± 12 μM. The acquisition time was 4 days.

The RFDR-based 2D $^{1}H/^{1}H$ chemical shift correlation provides site-specific information on a minority population of disordered Aβ40 oligomers in a fiber-containing sample. To obtain an atomic-level picture of these disordered oligomers, we use a combination of solution- and solid-state NMR experiments. RFDR is different from the NOESY experiment in that the incorporation of rotor-synchronized π-pulses during the mixing period reintroduces coherent homonuclear dipole-dipole interactions (Supplementary Fig. B.3). We first performed RFDR-based 2D $^{1}H/^{1}H$ experiments on two types of samples: the unfiltered, aggregated Aβ40 sample used in the CD experiments and a control sample of freshly dissolved Aβ40 without fibers made primarily of monomeric and low MW species. An overlay of the two 2D RFDR spectra is shown in Fig. 3.2. Only a few cross-peaks are observed in the 2D $^{1}H/^{1}H$ spectrum of the freshly dissolved Aβ40 sample (red in Fig. 3.2), probably due to the rapid tumbling of monomeric and/or low molecular weight Aβ40. The few cross-peaks that do appear in the spectrum of freshly dissolved Aβ40 likely arise from early aggregates, and the presence of peaks appearing near 0 ppm in the 1D 1H spectrum suggests that this is indeed the case (Supplementary Fig. B.4). Such peaks (near 0 ppm) are commonly observed in the spectra of amyloidogenic peptides, and have been shown to occur due to the presence of an oligomeric species in which aliphatic protons are solvent protected and thus shifted to the high field region of the 1D ^{1}H spectrum (39, 40). However, with the exception of these few cross-peaks, the RFDR-based 2D $^{1}H/^{1}H$ spectra of unaggregated Aβ40 is very sparse, consistent with weak (to negligible) ^{1}H-^{1}H dipolar couplings in low MW samples. The RFDR-based 2D $^{1}H/^{1}H$ experiment therefore acts as an efficient spectral filter for intermediate sized oligomers; low MW exhibit few cross-peaks because of weak (to negligible) ^{1}H-^{1}H dipolar couplings while the linewidth from very high MW species

like amyloid fibers is too large (due to very strong dipolar couplings) to generate a detectable signal under the slow MAS speeds used in this study.

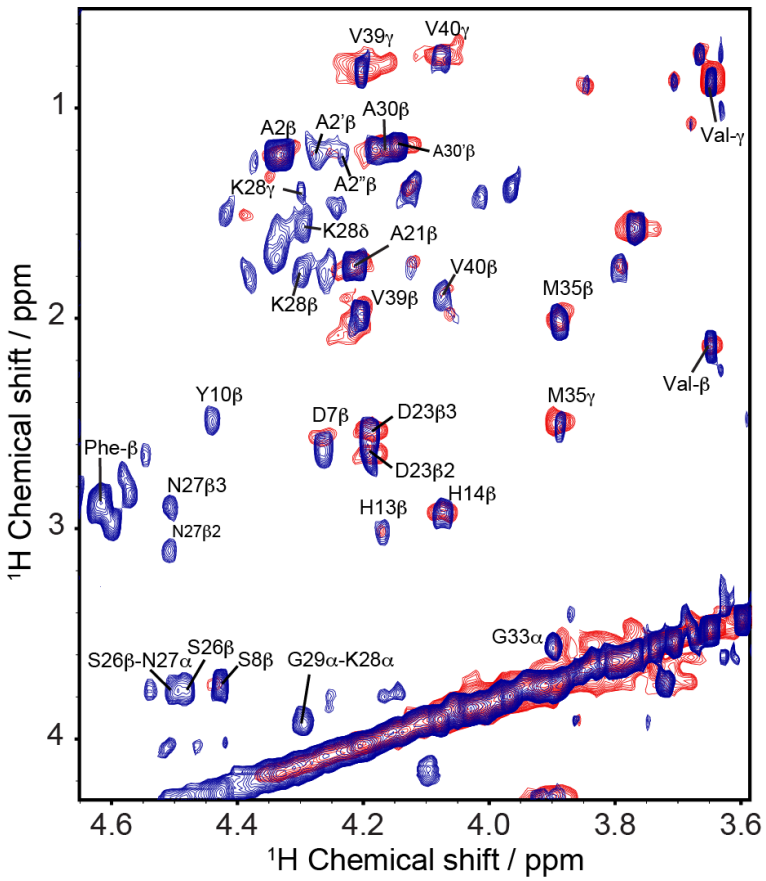

Figure 3.3 MAS spectra of the filtered disordered Aβ40 oligomer.
An overlay of the assigned Hα regions from RFDR-based 2D $^{1}H/^{1}H$ (blue) and 2D $^{1}H/^{1}H$ TOCSY (red) spectra acquired at 298 K with 10 kHz MAS. The filtered oligomer sample was lyophilized and re-hydrated to double its initial concentration, making for a total Aβ40 of ~35 μM. The RFDR and TOCSY based 2D $^{1}H/^{1}H$ spectra were acquired with mixing times of 50 and 70 ms, respectively, at 600 MHz in 100% D2O, 10 mM sodium phosphate buffer, pH 7.4. RFDR spectra were acquired at 25 °C under 10 kHz MAS. Assignments are given for the RFDR-based 2D $^{1}H/^{1}H$ spectra. The non-uniform sampling based data acquisition time was 4 hours.

In contrast to the sparse spectra obtained from unaggregated Aβ40, the RFDR-based 2D $^{1}H/^{1}H$ spectra of the aggregated sample showed multiple cross-peaks consistent with the presence of the disordered oligomer suggested by the CD, fluorescence, and AFM experiments (Fig. 3.1). The dominant feature of the RFDR-based 2D $^{1}H/^{1}H$ spectra is a very strong upfield

shift of Hα resonances compared to both the expected random coil values and the unaggregated, primarily monomeric sample. Upfield shifts typically derive from two primary sources: the formation of helical secondary structure and the shielding of the residue from solvent. Unfortunately, the spectra in Fig. 3.2 are not sufficient to distinguish between these two sources.

However, this spectrum was taken under rather extreme conditions of low concentration (~35 μM) and high heterogeneity (the oligomers only constitute 7-10% of the entire sample) to test the limits of the technique to samples not traditionally considered amenable for NMR. To see if additional structural details could be resolved in a more conformationally pure sample, we performed the RFDR-based 2D $^{1}H/^{1}H$ experiment on purified oligomers by removing the fibers through Spin-X filtration. We first tested the influence of the MAS rate by increasing it up to 15 kHz (Supplementary Fig. B.5). The fact that the resolution of 1D ^{1}H spectra does not improve with the increasing MAS rate suggests that oligomers are not sedimenting out of solution at the speeds used in the experiment, although the selective sedimentation of fibers may play a role in enhancing the resolution of the mixed fiber/oligomer sample (30).

Under 10 kHz MAS, we were able to obtain a well-resolved RFDR-based 2D $^{1}H/^{1}H$ spectrum of the pure oligomer sample (Fig. 3.3). A majority of peaks assigned in the RFDR-based 2D $^{1}H/^{1}H$ spectrum of the unfiltered sample (Fig. 3.2) are identified in the spectrum of the filtered oligomer sample as well (Fig. 3.3), suggesting peaks appearing in both samples arise from conformationally similar species. Under these conditions, it was possible to perform a partial assignment of the resonances using TOCSY experiments under MAS (Figs. 3.3, red spectrum). The lack of complete connectivity hampered the complete assignment of peaks in RFDR-based 2D $^{1}H/^{1}H$ spectra. Accordingly, the assignments of a partially folded structure of Aβ40 guided unambiguous assignment of 2D $^{1}H/^{1}H$ NMR spectra (14). While the lack of

connectivity is unavoidable given these constraints, the results suggest a spectrum that, while unusual for either a well-folded or unstructured protein, is consistent with results obtained from other biophysical experiments shown in Fig. 3.1. At the atomic level, the RFDR-based 2D $^{1}H/^{1}H$ spectrum contains inter-residue cross-peaks between the aliphatic and alpha protons of K28-G29, S26-N27, H13-G38, and S8-E11. These inter-residue contacts are observed for both 20 and 50 ms RFDR mixing times (Supplementary Fig. B.6), indicating the interaction of these residues are prominent features for the oligomer's structure. Moreover, the Ser and Gly fingerprints are observed only for the disordered oligomer species (circled cross-peaks in Fig. 3.2), suggesting the involvement of these residues in the oligomer formation and stabilization. More generally, though there are very strong up-field shifts for the resonances that usually suggest helix formation, no medium range αN (i, i+3/i+4) connectivity was found indicative of an α- or 310-helical conformation. Rather, the strong upfield shift appears to be the result of the oligomerization of peptide and the consequent shielding of the residues from solvent. Taken together, this finding suggests a dynamic and disordered structure with a high degree of turns and twists but without a well-defined secondary structure.

We do not rule out the possibility that highly mobile regions of the fibril may contribute in part to the RFDR spectrum recorded on the mixed fibril-oligomer sample. The serine and glycine fingerprints highlighted in Fig. 3.2 are not found in the RFDR spectra of the filtered oligomer nor are they found in the freshly dissolved samples of Aβ40. Nevertheless, a majority of the cross-peaks assigned in the RFDR spectra of the filtered oligomer are the same as those assigned in the unfiltered Aβ40 sample. Given that any highly mobile residue from the Aβ fibril would largely maintain the fibril's correlation time, it is more than likely that cross-peaks observed in the RFDR spectrum of the unfiltered sample derive from the disordered Aβ40

oligomer as MAS experiments performed on the filtered oligomer (Fig. 3.3 and Supplemental Fig. B.5). Isolation of the oligomer, although helpful in improving the resolution (compare Fig. 3.2 and Fig. 3.3), is not strictly necessary.

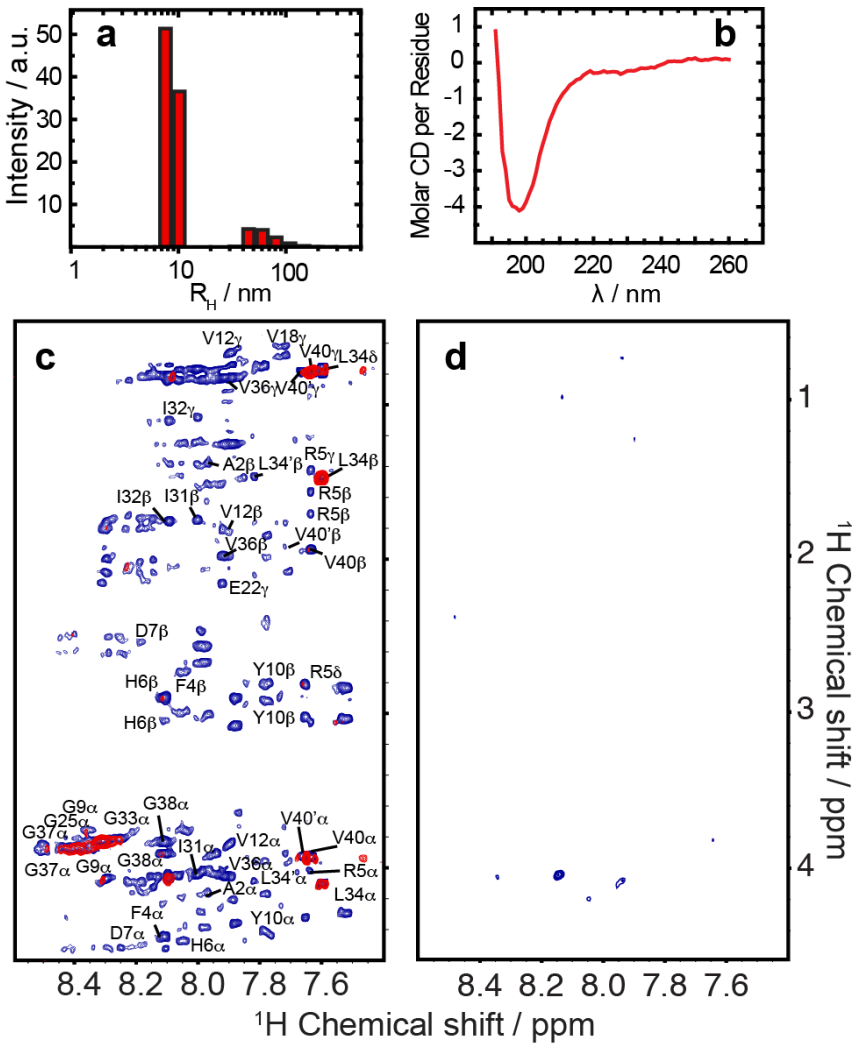

Figure 3.4 The disordered Aβ40 oligomer grows in size while maintaining its morphology.
(a) DLS experiments at 19 days demonstrate that the disordered oligomer not only remains disordered, but also grows in size as well with a distribution of hydrodynamic radii at 8.6 nm and 65.3 nm and polydispersity of 14.9% and 37.8%, respectively. (b) The strong minimum at ~ 200 nm in the CD spectrum of the disordered oligomer after 19 days reveals that the oligomer does not progress to a fibrillar state. Two-dimensional spectra of the fingerprint region of (c) TOCSY (70 ms mixing) and (d) NOESY (250 ms mixing) of the disordered Aβ1–40 oligomers recorded at 4 days (blue) and 19 days (red). The filtered oligomer sample was lyophilized and re-hydrated to double its initial concentration, making for a total Aβ40 of ~35 μM. After 19 days (red), almost all peaks are broadened beyond detection in both TOCSY and NOESY spectra.

The disordered Aβ40 oligomer is conformationally stable and grows in size. In light of our ability to purify the disordered Aβ oligomer, we were interested in whether the oligomers would aggregate into a fibrillar state. CD and DLS measurements confirm that the disordered nature of the oligomer is maintained while increasing in size over the course of 19 days (Fig. 3.4a-b). The CD spectrum of the spin-X-isolated oligomer at 19 days (Fig. 3.4b) shows a minimum intensity ca. 198 nm, indicative of random coil structure, and the DLS experiments indicate an increase in hydrodynamic radius of the oligomer from ~5.1 nm to ~8.6 nm (Fig 3.4a).

Solution and MAS NMR experiments further demonstrate that the spin-X-isolated Aβ oligomers are conformationally diverse and grow over time, yet maintain their disordered nature. The 1D profiles of ^{1}H MAS spectra do not change significantly over a period of 16 days, indicating the general fold of the oligomer is preserved. Between 4 and 9 days, the two sharp peaks at 1.20 and 1.18 ppm broaden beyond detection, while at the same time the oligomer peak at 0.16 ppm undergoes similar line-broadening (Supplementary Fig. B.7). We attribute this line-broadening to the increasing size of disordered Aβ oligomers. Even after 4 days of aggregation, cross-peaks were not observed in 2D NOESY spectra under MAS conditions (Supplementary Fig. B.8).

RFDR reveals details that solution NMR cannot for intermediate size oligomers. Since the RFDR pulse sequence (Supplementary Fig. B.3) utilizes the transfer of proton magnetization via coherent ^{1}H/^{1}H dipolar couplings and an incoherent cross-relaxation from the NOE to generate cross-peaks (34), we would expect the RFDR pulse sequence to be more sensitive to larger oligomers than the traditional NOESY experiment utilizing only NOE cross-relaxation. Accordingly, cross-peaks were not observed in 2D NOESY spectra obtained under MAS conditions and very few peaks were observed under static conditions (Supplementary Fig. B.8),

indicating the dipolar interaction among protons dominates the transfer of magnetization between nuclei of the disordered Aβ40 oligomer as evidenced by the RFDR spectrum in Fig. 3.3 (blue).

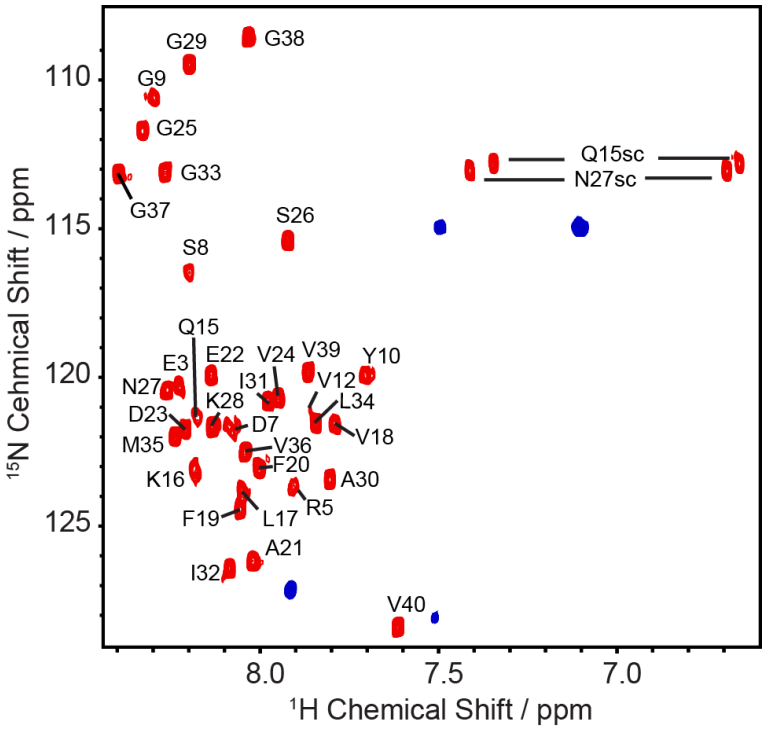

Figure 3.5 Comparison of $^{1}H/^{15}N$ HSQC spectra of the freshly dissolved (red) and the spin-X-isolated disordered oligomer (blue) of Aβ40 (after 4 days) recorded from a 900 MHz spectrometer. Both experiments were performed in 10 mM phosphate buffer, pH 7.4, and 10% D2O at 25 °C.

We further tested this observation by comparing the results from the RFDR experiment to solution NMR experiments using the time dependent growth of the oligomer from 4 to 19 days (Fig. 3.4c-d). Static TOCSY spectra (Fig. 3.4c) over this timeframe showed a severe decrease in the number of cross-peaks observed, while NOESY experiments under static conditions yielded little to very few cross-peaks at 4 days (Fig. 3.4d) and no cross-peaks were observed for the NOESY experiment at 19 days (data not shown). Similarly, 2D $^{1}H/^{15}N$ heteronuclear single-quantum correlation (HSQC) experiments performed on the spin-X-isolated oligomer of Aβ40

after 4 days (Fig. 3.5) exhibit drastically different HSQC spectra than that observed for a freshly dissolved Aβ40 sample (41, 42). Only four peaks are observed in the HSQC spectrum of the isolated, disordered Aβ40 oligomer after 4 days of aggregations; these likely coming from highly mobile residues and/or mobile side-chains. These results then suggest that molecular motions do not average out the $^{1}H/^{1}H$ dipolar interaction of the oligomer, and therefore the peaks are broadened beyond detection in solution NMR experiments. We therefore conclude that while the oligomer is observable by traditional solution NMR experiments, only limited information can be acquired, in contrast to the high-resolution information obtained from the RFDR-based 2D $^{1}H/^{1}H$ MAS solid-state NMR experiment.

3.3. Conclusions

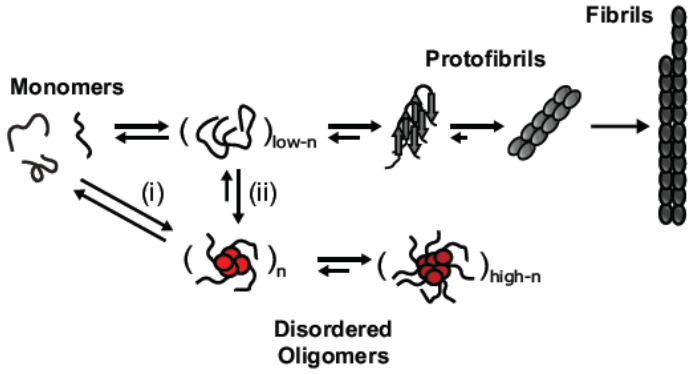

Figure 3.6 Simultaneously occurring aggregation pathways of Aβ40.
Early aggregates maintain structural similarity to the stable, disordered Aβ40 oligomers observed at late aggregation stages. The early aggregates either (i) solely nucleate the disordered oligomers or (ii) act as a single nucleating seed from which the two distinct aggregation pathways bifurcate.

Using the $^{1}H/^{1}H$ RFDR technique, we were able to reveal the dynamic and disordered structure comprised of turns and twists for the intermediate size (5-10 nm) oligomers. Through the implementation of both solution- and solid-state NMR experiments, particularly through the $^{1}H/^{1}H$ dipolar couplings recoupled by RFDR, we have characterized high-resolution structural properties of a dynamic and disordered Aβ40 oligomer and the development of early amyloid

aggregates. Disordered and/or micelle-like structures have been observed for other amyloid-forming proteins and peptides as well (43–46). In terms of a stable conformation, the oligomers studied here resemble, at least biophysically, conformers generated by small molecule amyloid inhibitors (such as polyphenols like EGCG (41, 47) or resveratrol (48)); i.e inert Aβ species that are large and predominantly unstructured. However, the stable oligomer studied here occurs without small molecule perturbations or chemical modifications in the Aβ peptide sequence. Furthermore, this disordered oligomer forms simultaneously with the highly ordered and well-defined structure of the β-sheet fibrils, indicating that a single aggregation pathway is not necessarily prevalent for a given preparation of Aβ (Fig. 3.6). Whether the disordered Aβ oligomer studied here is cytotoxic remains to be determined; however, the fact that this disordered conformation persists to an end-state that is not fibrillar is unexpected in light of the concept of nucleated conformational conversion and Aβ40 aggregation pathways in general (49, 50).

In a more general sense, our results demonstrate the value of the RFDR-based 2D $^{1}H/^{1}H$ experiment in obtaining high-resolution information on supramolecular assemblies not easily amenable to analysis by other biophysical techniques, including solution NMR and other solid-state NMR experiments. Specifically, most of the high-resolution data so far on amyloid oligomers and fibers has come from solid-state NMR experiments. These experiments have been invaluable in advancing our understanding of amyloid and other supramolecular assemblies. However, solid-state NMR experiments are inherently insensitive and require frozen or lyophilized samples that must also be isotopically labeled, often in a site-specific fashion that requires chemical synthesis rather than recombinant expression. Importantly, the $^{1}H/^{1}H$ RFDR experiment can be run on liquid samples using proton detection. For this reason, it is a highly

sensitive when compared to traditional solid-state NMR experiments and, at the same time, is able to access a molecular size range inaccessible to solution NMR experiments. Since it is run under solution conditions that allow dynamic averaging and very large insoluble aggregate species are spectrally filtered out by the procedure, it is also very tolerant to both conformational heterogeneity and heterogeneous oligomer size distributions. This is shown by Fig. 3.2, which shows the signal of the oligomer can be resolved without purification even though the oligomer comprises only ~7% of the total sample. Finally, since the experiment does not require isotopic labeling, it does not need recombinant protein expression. All of these characteristics make it ideal for medically relevant samples that have been difficult to characterize, such as amyloid oligomers directly derived from the brain, which in some cases have shown intriguingly different properties than the corresponding recombinant or synthetic Aβ peptide (13, 51–54).

3.4. Methods

3.4.1. Peptide Synthesis.

Aβ40 was synthesized manually by solid-phase Fmoc-based chemistry using the dimethoxybenzyl-protected (dmn) dipeptide, Fmoc-Val-(Dmb)-Gly-OH at positions 36 and 37 for the purpose of preventing aggregation during synthesis. The peptide was cleaved from the resin using 92.5% trifluoroacetic acid (TFA), 2.5% H2O, 2.5% ethanedithiol, and 2.5% anisole. The crude peptide was dissolved in 20% acetic acid (v/v) and purified by reverse-phase HPLC using a Waters semipreparative C18 column equilibrate in 0.1% TFA. The peptide was eluted with a linear gradient of 0-80% acetonitrile at a flow rate of 10 ml/min. Proper synthesis and purification were validated using matrix-assisted laser desorption ionization mass spectrometry, which gave a value corresponding to the correct mass 4329.9 Da.

3.4.2. Sample Preparation.

To remove preformed aggregates, the purified peptide was dissolved in 1% ammonium hydroxide (v/v) at a concentration of 1 mg/ml followed by removal of the solvent by lyophilization for 24 hours in aliquots of either 0.1 or 0.3 mg. The aliqouted peptide was then stored at -20 ^{O}C and only used once.

3.4.3. Preparation of Aggregated Aβ40 Sample:

For preparation of Aβ40 aggregated sample containing a mixture of fibers and disordered oligomers, 0.1 or 0.3 mg of the lyophilized peptide was solubilized in a 10 mM sodium phosphate buffer (pH 7.4) solution at a concentration of 1 mg/ml (231 μM) and incubated for 48 hours at 37 ^{O}C under agitation at 1000 rpm. This aggregated Aβ40 sample was then used to seed 5% of the total concentration of freshly dissolved Aβ40 in the same buffer conditions at a total Aβ40 concentration of 1 mg/ml. The seeded Aβ40 sample was incubated for 48 hours at 37 ^{O}C under agitation at 1000 rpm to form a sample containing a minority of Aβ40 oligomers (17.0 ± 6.0 μM or ~10% of the total peptide concentration) amongst a much larger population of Aβ40 fibrils. Concentrations were determined by the Thermo-Scientific BCA protein assay kit from 3 independent samples.

3.4.4. Isolation of Disordered Oligomers:

Upon completion of preparing the seeded Aβ40 aggregates (i.e. at the end of the 4 day incubation period), disordered oligomers were isolated using a Spin-X microcentrifuge spin column (Corning Inc.), containing a 0.22 μm cellulose acetate filter. The filtrate contained the isolated Aβ40 disordered oligomer (the 4-day old oligomer) and the Aβ40 fibrils were retained in the retentate. Due to the concentrations of the disordered oligomers being very low for NMR measurements, these samples could be lyophilized and rehydrated at double their concentration

(quantified above). This had no effect on the solution characteristics of the sample, namely its size, morphology, or secondary structure as verified by CD and DLS.

3.4.5. Monomer preparation (i.e., Freshly Dissolved Aβ40):

Preparation of Aβ40 monomer sample was performed as described previously.14 Briefly, 0.1 mg of the lyophilized peptide was first dissolved in 10 µl of 1 mM NaOH and sonicated until the peptide was solubilized. The peptide solution was then hydrated in H2O (or 100% D2O for MAS NMR measurements), buffered in 10 mM sodium phosphate (pH 7.4) and diluted to 76 µM (0.1 mg in 300 µl).

3.4.6. NMR Spectroscopy.

All NMR data was processed using TopSpin 2.1 (Bruker). 1D data were analyzed using TopSpin 2.1 and 2D data were analyzed using SPARKY. In all NMR spectra, the 1H peak from H2O was used as a chemical shift reference by setting its frequency at 4.7 ppm.

MAS NMR experiments were performed at 298 K or 310 K on an Agilent/Varian VNMRS 600 MHz solid-state NMR spectrometer using a 4 mm $^{1}H/X$ double-resonance Nanoprobe. The spectrometer was operated with a deuterium field lock and a MAS spinning speed of 2.7 kHz. The proton carrier frequency was set to the resonance frequency of water for all experiments and H_2O signal was suppressed using a 10 Hz saturation RF pulse for 1 s at the beginning of NOESY or RFDR-based 2D $^{1}H/^{1}H$ experiments. The radio frequency field strength used for the 90° and 180° pulses was 61 kHz. The NOESY and RFDR-based 2D $^{1}H/^{1}H$ spectra were recorded using 1100 scans, 200 t1 increments, 6252 t2 complex points and a spectral width of 11 ppm in both frequency dimensions. The experimental data sets were zero-filled in both t1 and t2 dimensions to form a 2048 x 4096 data matrix. Phase shifted sine bell multiplication was applied to both dimensions prior to Fourier transformation. Since the maximum MAS rate

possible with the Agilent Nanprobe is 2.7 kHz, to achieve higher MAS rates while maintaining the utility of deuterium locking and pulse-field gradients, we used a Bruker complete multi-phase (CMP) probe on a Bruker 600 MHz Avance III NMR spectrometer. 1D ^{1}H NMR spectra were acquired for MAS speeds from 5 to 15 kHz (Supplementary Figure 5). RFDR-based 2D ^{1}H/^{1}H experiments were performed under 10 kHz MAS with mixings times of 20 and 50 ms and using non-uniformly sampled (NUS), interleaved datasets. NUS datasets, where each dataset is split into its 2 component datasets using the Split program, were processed separately with the standard 'xfb' command, which regenerates the missing points and transforms the datasets.

Assignment of proton resonances was done using SPARKY with published assignments for Aβ40 as a guide. 1D ^{1}H MAS experiments were recorded with 20000 scans, 16 dummy scans, a spectral width of 12 ppm, and an acquisition time of 0.5 s. The proton carrier frequency was set at water resonance for all experiments and H_2O resonance was suppressed using a 50 Hz RF pulse for 1.5 s.

Solution NMR spectroscopy was performed on the filtered oligomer. Data were acquired on a 900 MHz Bruker NMR Spectrometer equipped with a cryogenic triple-resonance pulse-field gradient probe. 1D and 2D NMR spectra were collected at either 298 K or 310 K. NOESY spectra were acquired with a spectral width of 12 ppm in both dimensions; with 400 (ω1) and 2048 (ω2) complex points using a 1.5 s recycle delay. The NOESY experiments were acquired with two different mixing times: 250 and 600 ms. Solvent suppression was done using gradient pulses centered at ^{1}H resonance frequency of water. The same parameters were used for TOCSY experiments; however, mixing times of 70 and 100 ms were used. The experimental data sets were zero-filled to form a 2048 x 4096 data matrix and a phase-shifted sine bell multiplication was applied to both dimensions prior to Fourier transformation. ^{15}N-labeled Aβ40 was purchased

from rPeptide (Athens, GA, U.S.A.) and used for HSQC experiments. The exact same sample preparation protocols detailed above were used for ^{15}N-labeled Aβ40 samples. Each spectrum was obtained from 128 t1 experiments, 92 scans (for the spin-X-isolated Aβ40 oligomer) and 1 s recycle delay.

3.4.7. Circular Dichroism (CD).

CD measurements were performed on JASCO J-715 Spectropolarimeter using a 0.1 cm path length cell. Isolated oligomer and fibril samples of Aβ40 were prepared as described above. Molar CD per residue values were calculated using $\varepsilon = \theta_{obsd}/(3298lcn)$, where θ_{obsd} is the observed ellipticity measured in millidegrees, c is the molar concentration, l is the cell path length in centimeters, and n is the number of residues in the peptide.

3.4.8. bis-ANS and Thioflavin T Fluorescence Assays.

Aβ40 fibril formation was measured by increased fluorescence emission upon binding of amyloid fibers to the commonly used amyloid-specific dye, thioflavin T (ThT). Aβ40 oligomer and fibril formation were also measured by fluorescence emission spectra of the less specific dye, 4,4'-Dianilino-1,1'-Binaphthyl-5,5'-Disulfonic Acid (bis-ANS); purchased from Santa Cruz Biotechnology, Inc. bis-ANS exhibits limited fluorescence in water; however, becomes considerably fluorescent upon binding hydrophobic surfaces. Isolated oligomeric and fibrillar Aβ40 species were prepared as described above. The retentate containing Aβ40 fibrils was dissolved in 200 µL of 10 mM sodium phosphate buffer, pH 7.4, of which 90 µL was then aliquoted into microcentrifuge tubes. Similarly, the filtrate containing the Aβ40 oligomers was aliquoted into 90 µL quantities as well. Either ThT or bis-ANS fluorescent dye was then added to a peptide aliquot at a concentration of 10 µM and fluorescence emission was measured on a

Horiba FluoroMax 4 spectrofluorometer. An excitation wavelength of 446 nm and 350 nm was used for ThT and bis-ANS, respectively.

3.4.9. Atomic Force Microscopy (AFM).

An aggregated Aβ40 sample prepared as described above was deposited onto freshly cleaved mica and incubated for twenty minutes at room temperature. The surfaces was rinsed with nanopure water and dried under nitrogen flow. Dry imaging was carried out in tapping mode using a Nanoscope III atomic force microscopy (AFM) and JZ Scanner (Veeco) with VistaProbes T300R (NanoScience, AZ; nominal radius 10 nm, force constant 40 N/m, resonance frequency 300 kHz). The AFM was calibrated with a 100 nm x 100 nm standard (2D-100, NANOSENSORS, Switzerland). After calibration, the percent error was -0.6%. Random locations on the sample were selected for imaging. Particles were detected and height measurements were made using SPIP 6.0.13 software (NanoScience Instruments).

3.4.10. Dynamic Light Scattering (DLS).

Light scattering experiments were performed on Aβ40 samples prepared as described using a DynaPro Nanostar instrument from Wyatt Technology (Santa Barbara, CA). Light scattering was measured at 90°. The intensity correlation function and the distribution of the hydrodynamic radii (R_H) of the particles contributing to the scattering were determined using DYNAMICS software (Wyatt Technology).

3.4.11. Transmission Electron Microscopy (TEM).

Samples for negative stain TEM analysis were deposited on continuous carbon films on copper rhodium 100 mesh grids (Electron Microscopy Sciences, EMS Hatfield PA.). Prior to adding samples, the grids were charged using a glow discharger for 15 s at 30 mA negative

discharge. Fibrillar and oligomer sample solutions at 1 mg/ml were adsorbed to the grids for 2 minutes prior to rinsing with two 10 μL drops of water for 10 s. Samples were blotted using No. 2 Whatman filter paper. Samples for TEM were then stained with a 10 μL drop of freshly filtered 2% uranyl acetate (EMS) for 15s before blotting excess stain. Samples were analysed using a Philips CM-100 microscope operating at 80 kV.

3.5. Acknowledgements and contributions

In the adapted portions of this chapter from Kotler S.A. et al., (2015) *Sci. Rep.*, 5,11811, doi: 10.1038/srep11811:

This study was supported by research funds from the NIH and the Protein Folding Disease Initiative at the University of Michigan (to A.R.). S.K. was partly supported by the Molecular Biophysics Training Grant from the NIH to the University of Michigan. We would like to thank Dr. Ari Gafni and Dr. Duncan Steel for providing access to their lab equipment for optical spectroscopy measurements. We would also like to thank the Bruker Corporation for the use of their NMR spectrometers in Milton, Canada.

S.A.K., J.R.B., S.V., K.Y., J.K., M.M., and A.R. performed NMR experiments and analyzed NMR results. S.A.K., Y.S., and E.N.G.M. synthesized the peptide. M.C. and M.M.B.H. performed AFM experiments. S.A.K., P.W., and J.R.B. performed all other biophysical measurements. S.A.K., J.R.B., and A.R. designed the project and A.R. directed the research. All authors reviewed the published journal article.

3.6. References

1. 2015 Alzheimer's disease facts and figures (2015) *Alzheimer's Dement.* **11**, 332–384

2. Sakono, M., and Zako, T. (2010) Amyloid oligomers: formation and toxicity of Abeta oligomers. *FEBS J.* **277**, 1348–58

3. Benilova, I., Karran, E., and De Strooper, B. (2012) The toxic Aβ oligomer and Alzheimer's disease: an emperor in need of clothes. *Nat. Neurosci.* **15**, 349–57

4. Selkoe, D. J. (1991) The molecular pathology of Alzheimer's disease. *Neuron*. **6**, 487–498

5. Lin, H., Bhatia, R., and Lal, R. (2001) Amyloid beta protein forms ion channels: implications for Alzheimer's disease pathophysiology. *FASEB J*. **15**, 2433–2444

6. Butterfield, S. M., and Lashuel, H. a (2010) Amyloidogenic protein-membrane interactions: mechanistic insight from model systems. *Angew. Chem. Int. Ed. Engl.* **49**, 5628–54

7. Bernstein, S. L., Wyttenbach, T., Baumketner, A., Shea, J.-E., Bitan, G., Teplow, D. B., and Bowers, M. T. (2005) Amyloid β-protein: monomer structure and early aggregation states of Aβ42 and its Pro19 alloform. *J. Am. Chem. Soc.* **127**, 2075–84

8. Ball, K. A., Phillips, A. H., Wemmer, D. E., and Head-Gordon, T. (2013) Differences in β-strand populations of monomeric Aβ40 and Aβ42. *Biophys. J.* **104**, 2714–24

9. Baumketner, A., Bernstein, S. L., Wyttenbach, T., Bitan, G., Teplow, D. B., Bowers, M. T., and Shea, J.-E. (2006) Amyloid β-protein monomer structure: a computational and experimental study. *Protein Sci.* **15**, 420–8

10. Tycko, R. (2011) Solid-state NMR studies of amyloid fibril structure. *Annu. Rev. Phys. Chem.* **62**, 279–99

11. Schütz, A. K., Vagt, T., Huber, M., Ovchinnikova, O. Y., Cadalbert, R., Wall, J., Güntert, P., Böckmann, A., Glockshuber, R., and Meier, B. H. (2014) Atomic-Resolution Three-Dimensional Structure of Amyloid β Fibrils Bearing the Osaka Mutation. *Angew. Chem. Int. Ed. Engl.* 10.1002/anie.201408598

12. Petkova, A. T., Leapman, R. D., Guo, Z., Yau, W.-M., Mattson, M. P., and Tycko, R. (2005) Self-propagating, molecular-level polymorphism in Alzheimer's beta-amyloid fibrils. *Science*. **307**, 262–265

13. Lu, J.-X., Qiang, W., Yau, W.-M., Schwieters, C. D., Meredith, S. C., and Tycko, R. (2013) Molecular structure of β-amyloid fibrils in Alzheimer's disease brain tissue. *Cell*. **154**, 1257–68

14. Vivekanandan, S., Brender, J. R., Lee, S. Y., and Ramamoorthy, A. (2011) A partially folded structure of amyloid-beta(1-40) in an aqueous environment. *Biochem. Biophys. Res. Commun.* **411**, 312–6

15. Chimon, S., Shaibat, M. A., Jones, C. R., Calero, D. C., Aizezi, B., and Ishii, Y. (2007) Evidence of fibril-like β-sheet structures in a neurotoxic amyloid intermediate of Alzheimer's β-amyloid. *Nat. Struct. Mol. Biol.* **14**, 1157–64

16. Ahmed, M., Davis, J., Aucoin, D., Sato, T., Ahuja, S., Aimoto, S., Elliott, J. I., Van Nostrand, W. E., and Smith, S. O. (2010) Structural conversion of neurotoxic amyloid-beta(1-42) oligomers to fibrils. *Nat. Struct. Mol. Biol.* **17**, 561–567

17. Sarkar, B., Mithu, V. S., Chandra, B., Mandal, A., Chandrakesan, M., Bhowmik, D., Madhu, P. K., and Maiti, S. (2014) Significant structural differences between transient

amyloid-β oligomers and less-toxic fibrils in regions known to harbor familial Alzheimer's mutations. *Angew. Chemie*. **53**, n/a–n/a

18. Scheidt, H. a, Morgado, I., and Huster, D. (2012) Solid-state NMR reveals a close structural relationship between amyloid-β protofibrils and oligomers. *J. Biol. Chem.* **287**, 22822–6

19. Tay, W. M., Huang, D., Rosenberry, T. L., and Paravastu, A. K. (2013) The Alzheimer's amyloid-β(1-42) peptide forms off-pathway oligomers and fibrils that are distinguished structurally by intermolecular organization. *J. Mol. Biol.* **425**, 2494–508

20. Lendel, C., Bjerring, M., Dubnovitsky, A., Kelly, R. T., Filippov, A., Antzutkin, O. N., Nielsen, N. C., and Härd, T. (2014) A Hexameric Peptide Barrel as Building Block of Amyloid-β Protofibrils. *Angew. Chem. Int. Ed. Engl.* **53**, 12756–60

21. Yu, L., Edalji, R., Harlan, J. E., Holzman, T. F., Lopez, A. P., Labkovsky, B., Hillen, H., Barghorn, S., Ebert, U., Richardson, P. L., Miesbauer, L., Solomon, L., Bartley, D., Walter, K., Johnson, R. W., Hajduk, P. J., and Olejniczak, E. T. (2009) Structural characterization of a soluble amyloid beta-peptide oligomer. *Biochemistry*. **48**, 1870–7

22. Ladiwala, A. R. a, Litt, J., Kane, R. S., Aucoin, D. S., Smith, S. O., Ranjan, S., Davis, J., Van Nostrand, W. E., and Tessier, P. M. (2012) Conformational differences between two amyloid β oligomers of similar size and dissimilar toxicity. *J. Biol. Chem.* **287**, 24765–73

23. Ono, K., Condron, M. M., and Teplow, D. B. (2009) Structure-neurotoxicity relationships of amyloid beta-protein oligomers. *Proc. Natl. Acad. Sci. U. S. A.* **106**, 14745–50

24. Luo, J., Wärmländer, S. K. T. S., Gräslund, A., and Abrahams, J. P. (2014) Alzheimer peptides aggregate into transient nanoglobules that nucleate fibrils. *Biochemistry*. **53**, 6302–8

25. Serra-Vidal, B., Pujadas, L., Rossi, D., Soriano, E., Madurga, S., and Carulla, N. (2014) Hydrogen/Deuterium Exchange-Protected Oligomers Populated during Aβ Fibril Formation Correlate with Neuronal Cell Death. *ACS Chem. Biol.* **9**, 2678–2685

26. Stroud, J. C., Liu, C., Teng, P. K., and Eisenberg, D. (2012) Toxic fibrillar oligomers of amyloid-β have cross-β structure. *Proc. Natl. Acad. Sci. U. S. A.* **109**, 7717–22

27. Jehle, S., Rajagopal, P., Bardiaux, B., Markovic, S., Kühne, R., Stout, J. R., Higman, V. A., Klevit, R. E., van Rossum, B.-J., and Oschkinat, H. (2010) Solid-state NMR and SAXS studies provide a structural basis for the activation of alphaB-crystallin oligomers. *Nat. Struct. Mol. Biol.* **17**, 1037–42

28. Corsale, C., Carrotta, R., Mangione, M. R., Vilasi, S., Provenzano, A., Cavallaro, G., Bulone, D., and San Biagio, P. L. (2012) Entrapment of Aβ(1-40) peptide in unstructured aggregates. *J. Phys. Condens. Matter*. **24**, 244103

29. Suzuki, Y., Brender, J. R., Soper, M. T., Krishnamoorthy, J., Zhou, Y., Ruotolo, B. T., Kotov, N. a, Ramamoorthy, A., and Marsh, E. N. G. (2013) Resolution of oligomeric species during the aggregation of Aβ1-40 using (19)F NMR. *Biochemistry*. **52**, 1903–12

30. Bertini, I., Gallo, G., Korsak, M., Luchinat, C., Mao, J., and Ravera, E. (2013) Formation kinetics and structural features of Beta-amyloid aggregates by sedimented solute NMR. *Chembiochem*. **14**, 1891–7

31. Bennett, A. E., Griffin, R. G., Ok, J. H., and Vega, S. (1992) Chemical shift correlation spectroscopy in rotating solids: Radio frequency-driven dipolar recoupling and longitudinal exchange. *J. Chem. Phys.* **96**, 8624

32. Raya, J., Bianco, A., Furrer, J., Briand, J.-P., Piotto, M., and Elbayed, K. (2002) Proton Dipolar Recoupling in Resin-Bound Peptides under High-Resolution Magic Angle Spinning. *J. Magn. Reson.* **157**, 43–51

33. Pandey, M. K., Vivekanandan, S., Yamamoto, K., Im, S., Waskell, L., and Ramamoorthy, A. (2014) Proton-detected 2D radio frequency driven recoupling solid-state NMR studies on micelle-associated cytochrome-b(5). *J. Magn. Reson.* **242**, 169–79

34. Ramamoorthy, A., and Xu, J. (2013) 2D 1 H/ 1 H RFDR and NOESY NMR Experiments on a Membrane-Bound Antimicrobial Peptide Under Magic Angle Spinning. *J. Phys. Chem. B*. **117**, 6693–6700

35. Aucoin, D., Camenares, D., Zhao, X., Jung, J., Sato, T., and Smith, S. O. (2009) High-resolution 1H MAS RFDR NMR of biological membranes. *J. Magn. Reson.* **197**, 77–86

36. Kotler, S. A., Sciacca, M. F. M., Brender, J. R., Chen, J., Yamamoto, K., Lee, D., and Ramamoorthy, A. (2013) Gangliosides Mediate a Two-Step Mechanism of Membrane Disruption by Beta-Amyloid: Initial Pore Formation Followed by Membrane Fragmentation. *Biophys. J.* **104**, 217A–217A

37. Bolognesi, B., Kumita, J. R., Barros, T. P., Esbjorner, E. K., Luheshi, L. M., Crowther, D. C., Wilson, M. R., Dobson, C. M., Favrin, G., and Yerbury, J. J. (2010) ANS binding reveals common features of cytotoxic amyloid species. *ACS Chem. Biol.* **5**, 735–40

38. Guerrero-Muñoz, M. J., Castillo-Carranza, D. L., Sengupta, U., White, M. a, and Kayed, R. (2013) Design of metastable β-sheet oligomers from natively unstructured peptide. *ACS Chem. Neurosci.* **4**, 1520–3

39. Narayanan, S., and Reif, B. (2005) Characterization of chemical exchange between soluble and aggregated states of beta-amyloid by solution-state NMR upon variation of salt conditions. *Biochemistry*. **44**, 1444–52

40. Huang, R., Vivekanandan, S., Brender, J. R., Abe, Y., Naito, A., and Ramamoorthy, A. (2012) NMR characterization of monomeric and oligomeric conformations of human calcitonin and its interaction with EGCG. *J. Mol. Biol.* **416**, 108–20

41. Hyung, S.-J., DeToma, A. S., Brender, J. R., Lee, S., Vivekanandan, S., Kochi, A., Choi, J.-S., Ramamoorthy, A., Ruotolo, B. T., and Lim, M. H. (2013) Insights into antiamyloidogenic properties of the green tea extract (-)-epigallocatechin-3-gallate toward metal-associated amyloid-β species. *Proc. Natl. Acad. Sci. U. S. A.* **110**, 3743–8

42. Fawzi, N. L., Ying, J., Ghirlando, R., Torchia, D. A., and Clore, G. M. (2011) Atomic-resolution dynamics on the surface of amyloid-β protofibrils probed by solution NMR. *Nature*. **480**, 268–272

43. Brender, J. R., Krishnamoorthy, J., Sciacca, M. F. M., Vivekanandan, S., D'Urso, L., Chen, J., La Rosa, C., and Ramamoorthy, A. (2015) Probing the Sources of the Apparent Irreproducibility of Amyloid Formation: Drastic Changes in Kinetics and a Switch in Mechanism Due to Micellelike Oligomer Formation at Critical Concentrations of IAPP. *J. Phys. Chem. B*. **119**, 2886–2896

44. Walsh, P., Neudecker, P., and Sharpe, S. (2010) Structural properties and dynamic behavior of nonfibrillar oligomers formed by PrP(106-126). *J. Am. Chem. Soc.* **132**, 7684–95

45. Rhoades, E., and Gafni, A. (2003) Micelle formation by a fragment of human islet amyloid polypeptide. *Biophys. J.* **84**, 3480–7

46. Carulla, N., Zhou, M., Arimon, M., Gairí, M., Giralt, E., Robinson, C. V, and Dobson, C. M. (2009) Experimental characterization of disordered and ordered aggregates populated during the process of amyloid fibril formation. *Proc. Natl. Acad. Sci. U. S. A.* **106**, 7828–33

47. Lopez del Amo, J. M., Fink, U., Dasari, M., Grelle, G., Wanker, E. E., Bieschke, J., and Reif, B. (2012) Structural properties of EGCG-induced, nontoxic Alzheimer's disease Aβ oligomers. *J. Mol. Biol.* **421**, 517–24

48. Ladiwala, A. R. a, Lin, J. C., Bale, S. S., Marcelino-Cruz, A. M., Bhattacharya, M., Dordick, J. S., and Tessier, P. M. (2010) Resveratrol selectively remodels soluble oligomers and fibrils of amyloid Abeta into off-pathway conformers. *J. Biol. Chem.* **285**, 24228–37

49. Lee, J., Culyba, E. K., Powers, E. T., and Kelly, J. W. (2011) Amyloid-β forms fibrils by nucleated conformational conversion of oligomers. *Nat. Chem. Biol.* **7**, 602–609

50. Serio, T. R. (2000) Nucleated Conformational Conversion and the Replication of Conformational Information by a Prion Determinant. *Science (80-.).* **289**, 1317–1321

51. Moore, B. D., Rangachari, V., Tay, W. M., Milkovic, N. M., and Rosenberry, T. L. (2009) Biophysical analyses of synthetic amyloid-beta(1-42) aggregates before and after covalent cross-linking. Implications for deducing the structure of endogenous amyloid-beta oligomers. *Biochemistry*. **48**, 11796–806

52. Hartley, D. M., Zhao, C., Speier, A. C., Woodard, G. A., Li, S., Li, Z., and Walz, T. (2008) Transglutaminase induces protofibril-like amyloid beta-protein assemblies that are protease-resistant and inhibit long-term potentiation. *J. Biol. Chem.* **283**, 16790–800

53. Townsend, M., Shankar, G. M., Mehta, T., Walsh, D. M., and Selkoe, D. J. (2006) Effects of secreted oligomers of amyloid beta-protein on hippocampal synaptic plasticity: a potent role for trimers. *J. Physiol.* **572**, 477–92

54. Reed, M. N., Hofmeister, J. J., Jungbauer, L., Welzel, A. T., Yu, C., Sherman, M. A., Lesné, S., LaDu, M. J., Walsh, D. M., Ashe, K. H., and Cleary, J. P. (2011) Cognitive effects of cell-derived and synthetically derived Aβ oligomers. *Neurobiol. Aging*. **32**, 1784–94

Chapter 4: Elucidating the Mechanism of Amyloid-β Aggregation Using Fast-Acquisition NMR Methods

The content of this chapter will be included in the following reference:

Anirban Ghosh[§], Samuel A. Kotler[§], Janarthanan Krishnamoorthy, Jeffrey R. Brender, Bernd Reif, Anirban Bhunia, and Ayyalusamy Ramamoorthy. Probing transient, non-native states in amyloid fiber elongation by solution NMR. (2015), *In preparation*.

[§]Authors will have contributed equally to this work.

4.1 Introduction

Studying the fibrillation process of amyloid proteins has long been and still is of great importance, both for the development of reliable and early-stage diagnostic methods and for the identification of compounds that interfere with the protein misfolding process. The extreme stability of amyloid fibers and the long time scale for aggregation indicates that amyloid formation is a thermodynamically favorable process with a high activation barrier under kinetic control (1). Amyloid fiber formation is often modeled as a nucleation dependent process, (2) kinetically similar to one-dimensional crystal growth (3,4). In its most basic form, the first steps of the kinetic model consist of sequential, reversible addition of monomeric proteins to form energetically unfavorable and, therefore, rare intermediates. In the classical nucleation dependent polymerization model, (2) this process continues until a nucleus is created from which further aggregation is favorable. Upon formation of nuclei, aggregation propagates rapidly and, ostensibly, leads to cellular dysfunction.

Because the intermediate species are transient and difficult to observe, the experimental evidence for the nucleation dependent polymerization model for amyloid formation largely rests on kinetic modeling rather than direct experimental measurements. However, many kinetic models are consistent with the available data, and the simplest model that fits the limited data available is not necessarily the most relevant. The task is made more difficult as typically only the total fiber concentration is measured through the amyloid specific dye Thioflavin T and the concentrations of other species are interpolated from the model. A similar result was obtained by following the dissolution of radiolabeled monomers from the ends of unlabeled fibers (5). The resulting kinetics were interpreted as a two-stage binding mechanism in which the fast reversible association of monomeric Aβ to fibers ("docking") is followed by a second, slower step, which was interpreted as a conformational transition of the incoming monomer on the fiber surface that results in essentially irreversible binding ("locking") (6,7). The dock-lock mechanism of fiber elongation therefore consists of two steps: fast non-specific reversible association with the fiber surface in a non-native conformation followed by the slower adoption of the native fiber conformation once bound (5,7). Direct measurements of the elongation rate from preexisting fibers by fluorescence microscopy have revealed a more complicated picture in which fiber formation proceeds in a stop-and-go manner with bursts of fast elongation often followed by quiescent periods in which fiber elongation proceeds slowly or not at all (8-11). The stop-and-go manner of fiber elongation suggests the peptide has docked but not locked, blocking the fiber end and preventing incoming monomeric peptide from attaching to that fiber (7).

Despite these advances, a molecular understanding of the docking and locking process has been absent. Computationally, the dock-lock hypothesis has been explored by molecular dynamics which suggests a rugged landscape for fiber elongation (12-16) with both productive

and non-productive binding modes (17). A structural understanding of this process at the atomic level has proven very difficult to achieve experimentally as the growing end of the fiber comprises only a small fraction of the total sample and the large size of the fibers make them difficult to observe with most biophysical techniques. Here, we use solution NMR of an Aβ40 sample seeded with amyloid fibers to indirectly observe the docked state, which is not directly observable by solution NMR through the influence of the exchange-averaged NMR signal of the directly observable Aβ40 free in solution. We find that docking primarily proceeds through two stretches of residues in the central and C-terminal regions of the peptide, F19-K28 and L34-G37, with the highest degree of interaction focused on a small stretch of residues (F19-E22) that have been implicated in familial AD by mutational analysis as strongly influencing the fiber elongation rate (5,18).

4.2 Results

The SOFAST-HMQC experiment offers a unique ability to monitor Aβ aggregation at atomic resolution without the time constraints typical of most 2D NMR experiments, allowing the kinetic processes of fibril assembly to be monitored with residue specificity. As a control, we first measured the rate of monomer loss in unseeded solutions of Aβ40 through sequentially acquired ^{1}H-^{15}N SOFAST-HMQC experiments. In the absence of a fibril seed, the signal remained invariant over 15 hours, without substantial changes in either intensity (Fig. 4.1, black circles) or changes in chemical shift in this time period (Fig. C.1). The absence of any significant changes indicates that freshly dissolved Aβ40 is, if not necessarily entirely monomeric in nature, at least conformationally stable on the time-scale of our experiments under these conditions and does not form new oligomers or otherwise aggregate to any detectable extent in the absence of fibers (19,20).

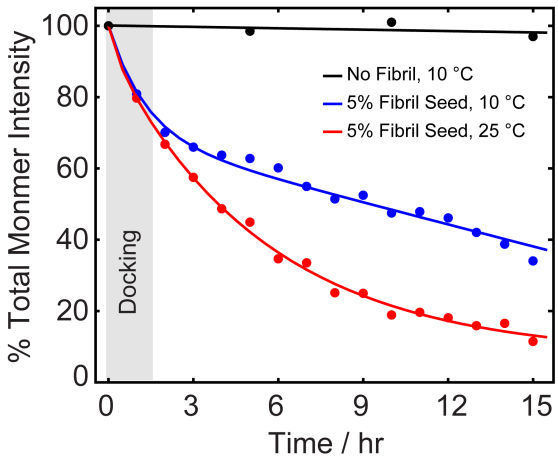

Figure 4.1 Aggregation of Aβ40 as monitored by real-time ^{1}H-^{15}N SOFAST HMQC.
Each point represents the total intensity of all monomer peaks with the peak center adjusted for each time-point. The sample without fiber present was fit to a line. The seeded experiments at 10° C and 25 °C were fit to double- and single- exponential curves, respectively. The two observable phases at 10 °C indicate two kinetically distinct processes. The grey bar indicates the time-scale in which the docking mechanism is dominant.

To initiate fiber growth in the sample, we seeded the reaction with 5 mol % preformed fibers prepared by incubating a 150 μM Aβ40 sample for 48 hours at 37 °C with constant agitation. The final result of this process is short, straight and largely unbranched amyloid fibers (Fig. 4.2B). Seeding the aggregation reaction with these fibers causes complex time-dependent changes in the spectra obtained from real-time 2D NMR experiments (Fig. 4.2A), suggesting an underlying dynamic process that is not present in the absence of fibers. The most prominent difference between the seeded and unseeded samples is a strong decrease in signal over time in the seeded samples (Fig. 4.1, blue and red lines). The most straightforward explanation is the signal loss simply represents the loss of monomeric peptide to a species that is invisible to NMR; however, this explanation is contradicted by the data. In general, large aggregates give rise to very broad signals that are undetectable in solution NMR unless a substantial amount of local conformational flexibility exists that averages out the dipole-dipole interactions and chemical shift anisotropy for particular residues (21). This flexibility does not exist in the fiber conformation as all residues are locked into a conformation that is tightly picked

against the fiber body except for nine residues at the N-terminus. If the peptide immediately adopts this rigid conformation after binding, the signal should decrease uniformly without broadening as only the signal from the remaining unbound peptide can be observed. Instead of a uniform decrease, there is a distinct variation along the peptide backbone at 10°C, which is initially slight but increases substantially as time progresses (Fig. 4.2A and C.2). This non-uniform intensity decrease can also be seen at 25°C even at the initial time point (Fig. C.3). The non-uniform decrease argues against such a single step binding mechanism, consistent with both previous kinetic experiments on fiber elongation in immobilized samples and the existence of two distinct kinetic phases in our real-time 2D NMR experiments at 10 °C (Fig. 4.1, blue line).

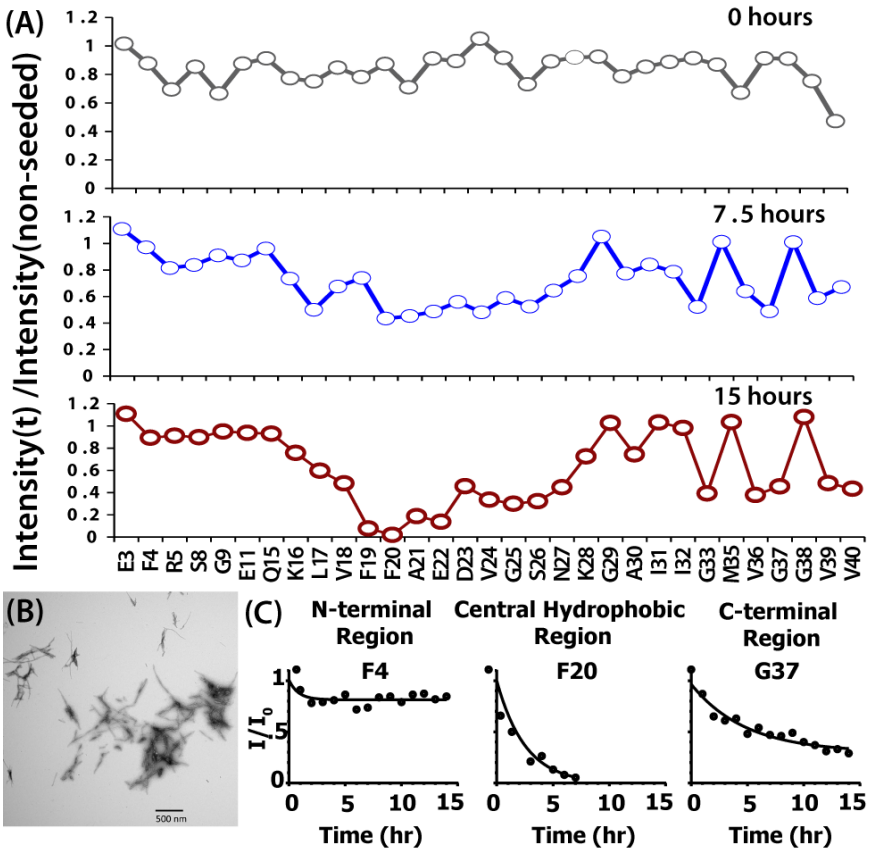

Figure 4.2 Real-time 2D NMR demonstrates residue-specificity of seeded Aβ40 aggregation.
(A) Time dependent variation of the SOFAST-HMQC signal of 80 μM freshly dissolved Aβ40 with 5 mol% fiber seeds along the peptide backbone during the fiber elongation reaction at 10 °C. Points represent the signal intensity of the peak maxima relative to the signal intensity in the absence of fiber seeds. The first time point (0 hr, top) represents the first spectra acquired immediately after the addition of

the fiber seeds. (B) Electron micrograph of a 150 μM Aβ40 sample incubated for 24 hours at 37°C with constant agitation. The amyloid fibers from this experiment were used as preformed amyloid seeds for the time dependent studies on aggregation. (C) Time traces for representative residues in the N-terminal, central hydrophobic, and C-terminal regions. Time trace for all residues can be found in the supporting information as Figs S2 (10 °C) and S3 (25 °C).

4.2.1 Soluble Aβ40 Makes Transient Non-Native Contacts with the Fiber Surface

Consideration of the real-time NMR experiments points to the Aβ monomer initially in dynamic association with the amyloid fiber. There are only a few contacts of the monomer on the fiber surface, resulting in weak reversible association on the millisecond timescale (18). Outside of the residues directly in contact with the fiber surface (Fig. 4.3, black cirlces), the remainder of the peptide in this model is conformationally flexible (20,22) and, therefore, resembles the largely unstructured, unbound peptide (23,24). In this tethered model (Fig. 4.3), the influence of the fiber on the spectra is most probably manifested indirectly through exchange processes between the unbound and bound forms. Depending on the timescale of exchange and frequency difference between the bound and unbound states, the peaks in HSQC spectra will either broaden due to intermediate exchange (Fig. 4.3B) or the peak position will shift due fast exchange (Fig. 4.e3A), with approximate exchange lifetimes τ_{ex} of ~1-10 ms or 1 μs-1 ms, respectively.

Using this model, it is possible to qualitatively explain the time evolution seen in the HSQC spectra. The macroscopic rate constants k_{on} and k_{off} are dependent on both the microscopic rate constants and the concentrations of the soluble peptide and the concentration of free fibril ends (fiber ends that are not blocked by a peptide bound in a non-native conformation that prevents further extension, i.e. docked but not locked in amyloid terminology). Unfortunately, the chemical shifts of the bound states (δ_{bound}) cannot be observed for most residues and are therefore unknown. The concentration of free fibril ends is also difficult to determine directly; however, a qualitative interpretation can be made using the tethered model described above. Since all the bound peptide in the fibril seed itself has presumably reached

equilibrium, the initial, nearly uniform, intensity decrease and chemical shift perturbation observed immediately after the addition of the fiber at 10°C largely represents the initial binding to the free fiber.(Fig. 4.3B). After the initial binding to the available fiber free ends, the system is now in equilibrium between the unbound peptide and docked peptide bound in a non-fibrillar conformation that prevents further extension of the fiber. No time-dependent changes are observed for the first 15 residues beyond the fast initial change. This is strong evidence that the N-terminal residues are not part of the non-fibrillar, docked binding state and do not make contact with the fiber. Time-dependent changes in the spectra are observed for the central residues from to K16 to K28. The time-dependence is partially a result of the locking step, which occurs due to irreversible binding to the fiber and a gradual shift towards a lower free monomer concentration and, consequently, a lower k_{on} and exchange rate. As a result, the exchange dynamics shift from the fast to the intermediate exchange regime giving rise to line broadening. This is most evident for a stretch of residues from F19-E22 (Fig. 4.2A and C.2). If the assumption of similar k_{on} values for different binding modes is made, these residues will have the lowest k_{off} values and, therefore, correspond to the most likely points of contact in the tethered model. A similar stretch of residues with a somewhat lesser degree of broadening over time can also be seen in the neighboring stretch of residues D23-N27 (Fig. 4.2A). The C-terminus from G29-V40 is primarily defined by several residues (G29, I30, I31, M35, G38) whose signal is not broadened and remain in fast exchange throughout the experiment with the implication that these residues are not in contact with the surface in the bound state conformational ensemble. Within the C-terminal region, however, there are other residues such as G33, V36, and G37 that do show a substantial degree of broadening at longer time points. The sharpness of the effect suggests the contacts in any bound state are limited to only a very small set of neighboring residues. Overall,

the data suggest the docked state conformational ensemble is primarily centered in K16-N27 with only transient contacts outside this range.

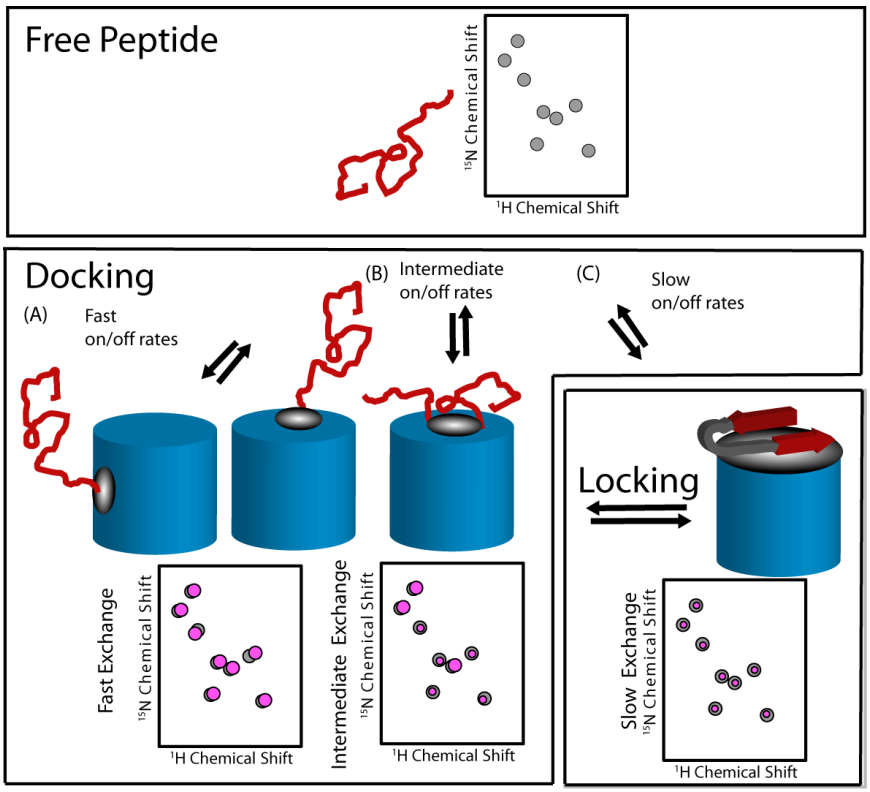

Figure 4.3 Cartoon model showing possible modes of interaction of soluble Aβ40 with Aβ40 fibers and the effect of the interaction on the NMR spectra.
(A) Weak association from the transient contact of a few residues with the fiber surface. Fast exchange is expected in this case with chemical shift perturbations at the contacting sites. Note that the peptide can potentially dock to either the growing ends (right) or sides (left) of the fiber. (B) Stronger association with slower on/off rates. Intermediate or slow exchange is expected with the signal decreasing for the contacting residues. Outside the contacting residues, the chain is either freely rotating or making transient contacts with the fiber. (C) Once bound ("docking") the peptide adopts the fiber conformation in a separate step ("locking"). No signal can be detected from the locked state directly due to the rigid nature of the fiber.

The time series at 25 °C replicates most of the features of the 10 °C sample with the complication that the apparent locking phase is much faster than observed at 10 °C and, as a result, the overall signal decreases much more rapidly. The docking and locking stages are no longer as kinetically distinct at 25 °C and the loss of peptide to irreversible binding can be seen

more prominently early on in the time series (Fig. C.3). Nevertheless, the key features of the 10 °C time series are replicated at 25 °C.

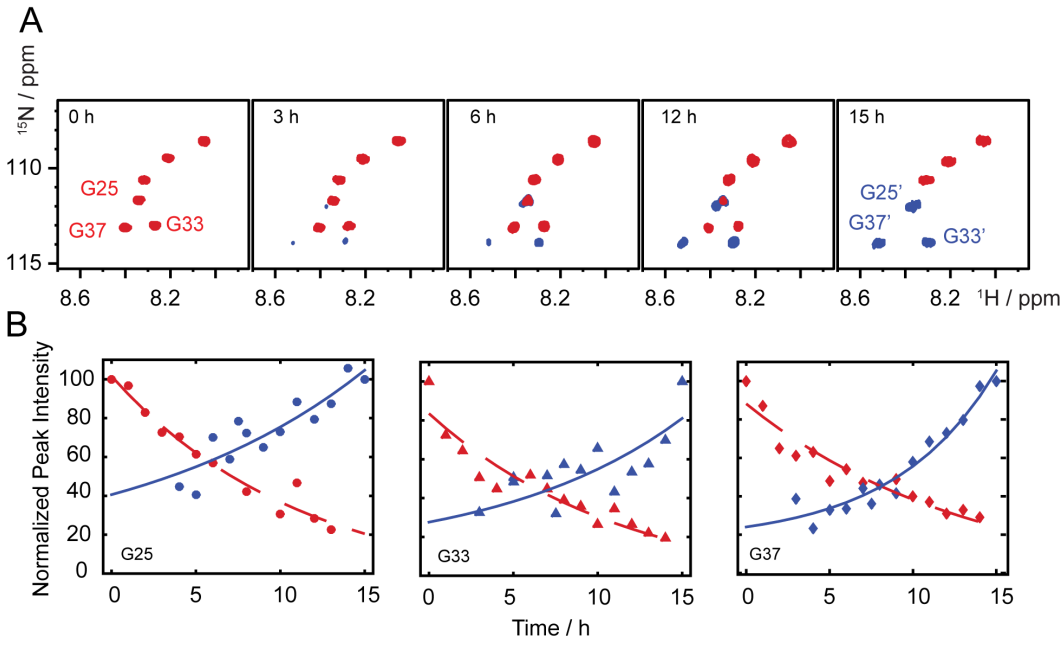

Figure 4.4 New peaks arising in HSQC spectra suggest slow exchange process in seeded Aβ40 aggregation.
(A) C-terminal residues in apparent slow exchange with the fiber surface. (B) Time evolution of the monomer (red) and apparent exchange peaks (blue) for the residues shown in (A) at 10 °C.

4.2.2 2D Real-Time NMR Reveals a Slow Exchange Process Occurring between Aβ40 Monomers and Fibers Linked to Dynamic Contacts at the C-terminus

Intriguingly, a new set of peaks reproducibly appears in the later stages of the time series at 10 °C. These peaks are not apparent in the samples incubated without fiber seeds indicating their production is dependent on, or at least catalyzed by, the fiber surface. Three of the new peaks could be assigned to glycine residues 25, 33, and 37 without 3D assignment as the buildup of these peaks nearly exactly matches the decrease in intensity of peaks of corresponding to the unbound form of these residues (Fig. 4.4 and Fig C.4); a strong indication these peaks are in slow exchange with each other. Over longer time periods, such slow exchange processes are gradually

observed for other residues as well (Fig. C.5). No new peaks are observed at 25 °C, likely due to an increase in the exchange rate at higher temperature. Given the density in other regions of the spectrum, it is difficult to correlate the appearance of new peaks to existing peaks in the unbound spectra using only the SOFAST-HMQC experiments. Nonetheless, some of the new peaks could be assigned from 3D HNCA and HNCACB experiments. Interestingly, the new peaks that are assigned are those near the C-terminus and, to a lesser extent the N-terminus, with none of the peaks from the central hydrophobic region appearing in the spectrum (Fig. C.6).

Because the peaks are in slow exchange, the new peaks must be derived from a species that can be directly detected by NMR. However, they cannot be the result of simple aggregation from the monomeric state, as such peaks are not detected in the absence of fibers. The new peaks could, therefore, result either from the formation of small soluble oligomers whose formation is catalyzed by the presence of fibers or by residues that have enough local flexibility in the fiber bound state to be directly detectable by NMR. To distinguish between these possibilities, we performed pulse field gradient NMR on the sample to characterize the size of the NMR detectable species as a function of time. No difference existed between the samples with or without fibers and no change in the hydrodynamic radius could be detected over time (Fig. C.7). To further establish that the changes seen in the NMR spectra originate from the monomer-fiber equilibria, we repeated real-time HSQC acquisition with intermittent sonication of the sample for 2 minutes after every 90 minutes of incubation. Sonication is expected to mechanically fragment unstable long fibers generating new fiber ends in the process, while leaving smaller oligomers less affected (25). The result of the sonication experiment is an acceleration of the time-dependent changes seen in the static samples (Fig. C.8).

Based on these results, the appearance of new peaks can be ascribed to fibril bound states. While being able to resolve peaks of an Aβ40 monomer bound to its amyloid form is unexpected, it is not unprecedented, as highly mobile residues have been directly observed for β_2-microglubin amyloid fibers in solution NMR (21,26,27). In this case, highly flexible residues at the N-terminus could be detected throughout the length of the fiber, despite the fiber's very large molecular weight. More generally, the flexible regions of a number of large biomolecular systems, including multidomain enzymes, molecular chaperones, and intact ribosomes, have been characterized by solution-state NMR spectroscopy. Although the size of such species can greatly exceed the usual limits for solution-state NMR methods, the motional narrowing resulting from local mobility can be sufficient to average almost completely the anisotropic interactions that normally dominate the transverse relaxation rates. Resonances from such states may then have linewidths comparable to those of free peptides in solution.

The new peaks must arise from residues with high flexibility in the bound state but with chemical shifts significantly different than the unbound peptide. Since the unbound peptide is predominantly unstructured, this difference must result from transient contacts at those sites with the fiber surface. The appearance of the new peaks is consistent with a two-site tethered state model with slow exchange of the entire peptide off the fiber surface and fast on/off contacts at another site. The chemical shifts of the new peaks are the time-averaged values of the fast on/off contacts. In this model, the central hydrophobic self-recognition sequence binds the fiber relatively tightly while the termini remain dynamic, making only transient contacts with the fiber surface. This result is consistent with the new peaks being only found at the dynamic N and C-termini and not from the more tightly bound residues in the center of the peptide (Fig C.6).

4.2.3 Longitudinal Relaxation Rates Support a Two-Site Binding Model

The effect of the fiber seed on the relaxation rate provides an alternative method of confirming the existence of transient fiber bound states. In the absence of fiber seeds, Aβ40 has a near uniform longitudinal relaxation rate (R1) of 1.89 ± 0.2 s^{-1} across the length of the peptide (Fig. 4.5) (19). For a molecule tumbling freely in solution, the longitudinal relaxation rate is correlated with the rotational correlation time of the molecule scaled by the internal motion occurring at each residue. The absence of a significant variation in R_1 values throughout the peptide sequence indicates the internal dynamics is largely similar throughout the peptide on the ps-ns time-scale, consistent with the rapid conformational interconversion typical of a largely unstructured peptide without a single well-defined tertiary or secondary structure.

The addition of a fiber seed causes a dramatic change in the R1 profile. The relaxation rates are no longer uniform, but instead show clear clusters of residues with significantly higher than average R1 values that are at least twice that of the remaining residues (Fig. 4.5). The enhanced R1 relaxation rates after the addition of fiber seeds is unusual, as it would seem to imply significantly enhanced internal motion in the bound state. However, this is based on the assumption that the overall molecular tumbling is isotropic, which is untrue for molecules bound to amyloid fibers. Because the fibers have a high degree of diamagnetic anisotropy, they spontaneously align in the spectrometer along the direction of the magnetic field (28,29). Transient contacts with the fiber therefore impart a small degree of alignment to the monomeric peptide. The enhanced relaxation rate reflects the effect of increase in dipolar interactions due to this small amount of alignment, (30) which average to zero under isotropic tumbling.

The R1 profile closely matches the pattern of residues with faster than average intensity decays in the NMR time course experiments (Fig. $.2A). The most prominent cluster with

enhanced R1 values is a four-residue stretch (F20, A21, D22, and E23) in the central region of the peptide immediately adjacent to another stretch (V24, G25, S26, and K28- the resonance for N27 could not be detected) also exhibiting enhanced relaxation values. Beyond the central region, another cluster of residues near the C-terminus (L34, M35, V36, and G37) also shows enhanced relaxation. Overall, the R1 profile is consistent with the binding modes suggested by the analysis of the apparent chemical exchanges rates (Fig. 4.3) and provides independent verification of the two-site binding model (central and C-terminus) suggested by these experiments.

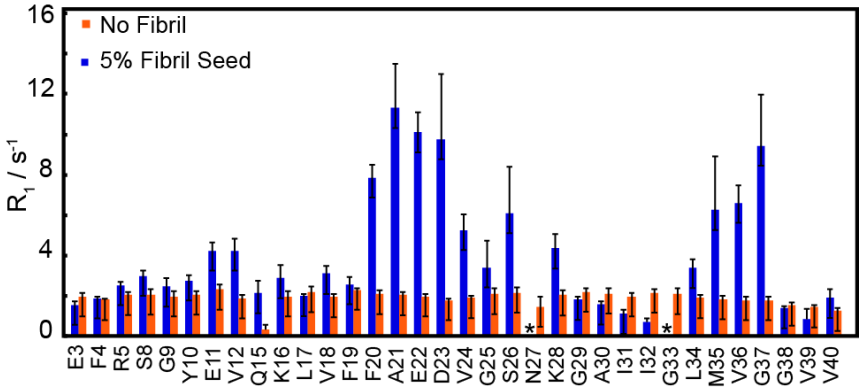

Figure 4.5 Variation in longitudinal relaxation rates in the presence and absence of amyloid fibers. Fiber seeds were added to a concentration of 5 mol % of the Aβ40 monomer.

4.2.4 Residual Dipolar Coupling Analysis Suggests Aβ40 Can Partly Bind Perpendicular to the Fiber Axis in a Non-Native Conformation

All of the experiments above provide information on the residues in apparent contact with the fiber in the bound state. The spontaneous alignment of fibers in a magnetic field can be exploited further to gain structural information beyond that obtainable from the time dependent HSQC experiments. The transient contacts with the fibers should manifest in transferred residual dipolar couplings (RDCs), which are in turn tied to the orientation of the amide bond with respect to the fiber axis (28,29). In theory, an exact orientation can be defined for each residue

with measurable RDCs. In practice, however, this requires an exact knowledge of the bound state structure, which is unobtainable for the system being studied here (31). A qualitative analysis of the measured RDC values is possible; however, using only the sign of the RDC to assign the approximate orientation of the amide bond. The gyromagnetic ratio of ^{15}N is negative and therefore a negative RDC is expected if the amide bond is oriented parallel to the fiber axis along the beta sheets in the magnetic field, while a positive RDC is expected if the amide bond is oriented perpendicular to the fiber axis (28,29). For the residues within the β-sheet regions that make up the fiber core (K16-A21 and A30-M35) (32), the presence of a significantly non-zero positive RDC therefore implies a non-fibrillar conformation. The majority of the RDCs that could be measured are in fact positive. Significantly, non-zero positive RDCs (D_{NH}> 0.5 Hz) could be detected for a stretch of residues from K28-I31 (Fig. 4.6) which are located near the loop region in the fiber conformation. The residues in this loop region are expected to have fluctuating conformations with some conformations in the ensemble oriented perpendicular to the fiber axis. Positive RDCs are, therefore, consistent, but not necessarily indicative of a bound state that resembles the fiber conformation. Yet, significantly non-zero RDCs are also found for F19 and L34, which are well within the fiber core (fig. 6). Only V24 that is located within the loop outside the fiber core has a significantly negative RDC value (Fig. 4.6), although smaller negative RDCs can be seen at the C-terminus from G38-V40. While the RDCs cannot be interpreted as evidence for a particular structure, they do suggest that the ensemble of bound states contains a significant fraction of states that do not resemble the fiber conformation (Fig. 4.3).

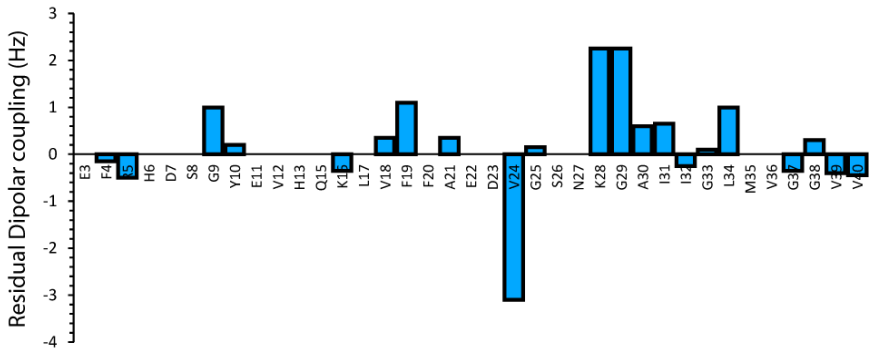

Figure 4.6 Residual dipolar couplings induced by the addition of amyloid fibers, which spontaneously align parallel to the magnetic field.
A positive dipolar coupling indicates an orientation of the N-H bond vector perpendicular to the fiber axis and a negative dipolar coupling indicates a parallel orientation.

4.3 Discussion

The most detailed examination of the binding of soluble Aβ to a fiber-like species at the molecular level to date was done by Fawzi et al, who used saturation transfer experiments to obtain quantitative estimates of binding to amyloid protofibers at the residue level (20,22,33,34). The highest affinity for the protofiber surface was found in two stretches on the monomer (K16–G25 and K28–G37) that roughly correspond to the residues forming β-sheets in the fiber model (20). The differences in site-specific affinity observed in the present can be attributed to the distinct structural differences that exist between the protofibers and mature amyloid fibers (35). Protofibers are intermediates created when high concentrations (>150 μM) of monomeric Aβ is incubated in vitro (20) which differ structurally from mature fibers in their supramolecular organization. In contrast to the long straight morphology of amyloid fibers (Fig. 4.2B), protofibers are short, worm-like aggregates of irregular shape with a lower amount of stable hydrogen bonded structure than mature amyloid fibers (36). Significantly, infrared spectroscopy suggests an antiparallel organization of the beta sheets rather than the parallel orientation found in amyloid fibers (37) with different contacts among the core than in amyloid fibers (35). NMR studies have also suggested the β-strands are shorter in protofibers than amyloid fibers (38) and

that the side-chains of protofibers are more dynamic (35). The difference in structure translates to a difference in properties between the two species. Protofibers exist in a stable equilibrium with monomeric Aβ (20) and the transition between protofibers and monomeric Aβ is readily reversed by dilution (39). In contrast, the equilibrium concentration of monomer with amyloid fibers is very low (<1 μM) and the thermodynamic equilibrium strongly favors fiber formation (1,40).

For actual amyloid fibers, molecular details of the association steps involved in fiber elongation have been largely absent. Paramagnetic relaxation enhancement experiments using a fibril seed labeled at either A2 or A30 suggest that association of the monomer with the N-terminus of the fiber during the docking stage is rare (41). Our experiments, which analyze the residue specificity of the monomer contacts in the docked state, offer a more detailed view of the docked state and highlight important differences between the docked state of the monomer in the fibers and protofibers. In protofibers, the KLVFFA sequence from residues 16-21 has the highest affinity for the protofiber surface (20,34). In actual fibers, the main recognition sequence of the docked state is shifted towards the C-terminus, centered on F19-E22 of the incoming monomeric peptide (Figs 4.2A and 4.5A). The shift is significant as the KLVFF sequence has been implicated in Aβ40 self-recognition and modified forms of the peptide sequence have been used for this reason as a motif in the design of peptide inhibitors targeting arresting fiber formation. This particular sequence was identified by finding the optimal binding sequence in a series of short peptides derived from the Aβ40 sequence (42). However, the KLVFF peptide is only moderately effective at suppressing both fiber formation and toxicity (43). A significant effect with short peptides is typically found only with a high excess of inhibitor. This finding is in contrast to the substantial effects seen at sub-stoichiometric levels with some longer peptides

(44) and antibodies (45) derived from the Aβ sequence; a difference which might be explained by a discrepancy between the optimal sequences for the locking and docking stages.

4.4 Materials and Methods

Recombinant ^{15}N-Aβ40 was purchased from rPeptide (Bogart, GA) and samples were prepared as described in ref 24. Unlabeled Aβ40 was purchased from Genscript USA, Inc. (Piscataway, NJ) and used to prepare fibril seeds under agitation at 37 ºC for 48 hours. All experiments were performed in 50 mM sodium chloride, 20 mM phosphate buffer, at pH 7.4. For Aβ40 samples prepared as fibril seeds, 0.01% NaN_3 was added to phosphate buffer solutions. Aβ40 monomer samples were prepared to a concentration of ~76 μM, and verified by UV/Vis measurements with a Thermo Scientific Nanodrop 2000 (extinction coefficient 1490 $M^{-1}cm^{-1}$). NMR experiments were performed on a Bruker Avance 600 MHz spectrometer equipped with a 5 mm cryogenic probe or on a Bruker Avance III 500 MHz NMR spectrometer equipped with a 5 mm SMART probe. Real-time 2D NMR experiments were performed using the SOFAST-HMQC technique and acquired consecutively for a minimum of 15 hours. Detailed methods are described in the Supporting Information.

4.5 Contributions

A.G., S.A.K., J.K., J.R.B., A.B., and A.R. performed NMR experiments and analyzed NMR results. B.R. expressed and purified uniformly 13C, 15N-labeled Aβ40. S.A.K., J.K., J.R.B., A.B., and A.R. designed the project and A.B. and A.R. directed the research.

4.6 References

1. O'Nuallain, B., Shivaprasad, S., Kheterpal, I., and Wetzel, R. (2005) Thermodynamics of A beta(1-40) amyloid fibril elongation. *Biochemistry* **44**, 12709-12718

2. Oosawa, F., and Asakura, S. (1975) *Thermodynamics of the polymerization of protein*, Academic Press, London ; New York

3. Gebauer, D., and Colfen, H. (2011) Prenucleation clusters and non-classical nucleation. *Nano Today* **6**, 564-584

4. Li, M. S., Klimov, D. K., Straub, J. E., and Thirumalai, D. (2008) Probing the mechanisms of fibril formation using lattice models. *J Chem Phys* **129**

5. Esler, W. P., Felix, A. M., Stimson, E. R., Lachenmann, M. J., Ghilardi, J. R., Lu, Y. A., Vinters, H. V., Mantyh, P. W., Lee, J. P., and Maggio, J. E. (2000) Activation barriers to structural transition determine deposition rates of Alzheimer's disease A beta amyloid. *J Struct Biol* **130**, 174-183

6. Esler, W. P., Stimson, E. R., Jennings, J. M., Vinters, H. V., Ghilardi, J. R., Lee, J. P., Mantyh, P. W., and Maggio, J. E. (2000) Alzheimer's disease amyloid propagation by a template-dependent dock-lock mechanism. *Biochemistry* **39**, 6288-6295

7. Massi, F., and Straub, J. E. (2001) Energy landscape theory for Alzheimer's amyloid beta-peptide fibril elongation. *Proteins* **42**, 217-229

8. Kellermayer, M. S. Z., Karsai, A., Benke, M., Soos, K., and Penke, B. (2008) Stepwise dynamics of epitaxially growing single amyloid fibrils. *Proc Natl Acad Sci USA* **105**, 141-144

9. Wordehoff, M. M., Bannach, O., Shaykhalishahi, H., Kulawik, A., Schiefer, S., Willbold, D., Hoyer, W., and Birkmann, E. (2015) Single Fibril Growth Kinetics of alpha-Synuclein. *J Mol Biol* **427**, 1428-1435

10. Ferkinghoff-Borg, J., Fonslet, J., Andersen, C. B., Krishna, S., Pigolotti, S., Yagi, H., Goto, Y., Otzen, D., and Jensen, M. H. (2010) Stop-and-go kinetics in amyloid fibrillation. *Phys Rev E* **82**

11. Patil, S. M., Mehta, A., Jha, S., and Alexandrescu, A. T. (2011) Heterogeneous amylin fibril growth mechanisms imaged by total internal reflection fluorescence microscopy. *Biochemistry* **50**, 2808-2819

12. Lee, C. F., Loken, J., Jean, L., and Vaux, D. J. (2009) Elongation dynamics of amyloid fibrils: A rugged energy landscape picture. *Phys Rev E* **80**

13. Nguyen, P. H., Li, M. S., Stock, G., Straub, J. E., and Thirumalai, D. (2007) Monomer adds to preformed structured oligomers of A beta-peptides by a two-stage dock-lock mechanism. *Proc Natl Acad Sci USA* **104**, 111-116

14. O'Brien, E. P., Okamoto, Y., Straub, J. E., Brooks, B. R., and Thirumalai, D. (2009) Thermodynamic Perspective on the Dock-Lock Growth Mechanism of Amyloid Fibrils. *J Phys Chem B* **113**, 14421-14430

15. Straub, J. E., and Thirumalai, D. (2010) Principles governing oligomer formation in amyloidogenic peptides. *Curr Opin Struc Biol* **20**, 187-195

16. Straub, J. E., and Thirumalai, D. (2011) Toward a Molecular Theory of Early and Late Events in Monomer to Amyloid Fibril Formation. *Annual Review of Physical Chemistry, Vol 62* **62**, 437-463

17. Gurry, T., and Stultz, C. M. (2014) Mechanism of amyloid-beta fibril elongation. *Biochemistry* **53**, 6981-6991

18. Cannon, M. J., Williams, A. D., Wetzel, R., and Myszka, D. G. (2004) Kinetic analysis of beta-amyloid fibril elongation. *Anal Biochem* **328**, 67-75

19. Yan, Y. L., and Wang, C. Y. (2006) A beta 42 is more rigid than A beta 40 at the C terminus: Implications for A beta aggregation and toxicity. *J Mol Biol* **364**, 853-862

20. Fawzi, N. L., Ying, J. F., Ghirlando, R., Torchia, D. A., and Clore, G. M. (2011) Atomic-resolution dynamics on the surface of amyloid-beta protofibrils probed by solution NMR. *Nature* **480**, 268-U161

21. Yoshimura, Y., Sakurai, K., Lee, Y. H., Ikegami, T., Chatani, E., Naiki, H., and Goto, Y. (2010) Direct observation of minimum-sized amyloid fibrils using solution NMR spectroscopy. *Protein Sci* **19**, 2347-2355

22. Fawzi, N. L., Ying, J., Torchia, D. A., and Clore, G. M. (2010) Kinetics of Amyloid beta Monomer-to-Oligomer Exchange by NMR Relaxation. *J Am Chem Soc* **132**, 9948-9951

23. Danielsson, J., Andersson, A., Jarvet, J., and Graslund, A. (2006) N-15 relaxation study of the amyloid beta-peptide: structural propensities and persistence length. *Magnetic Resonance in Chemistry* **44**, S114-S121

24. Vivekanandan, S., Brender, J. R., Lee, S. Y., and Ramamoorthy, A. (2011) A partially folded structure of amyloid-beta(1-40) in an aqueous environment. *Biochemical and biophysical research communications* **411**, 312-316

25. Huang, Y. Y., Knowles, T. P. J., and Terentjev, E. M. (2009) Strength of Nanotubes, Filaments, and Nanowires From Sonication-Induced Scission. *Adv Mater* **21**, 3945-+

26. Platt, G. W., Xue, W. F., Homans, S. W., and Radford, S. E. (2009) Probing Dynamics within Amyloid Fibrils Using a Novel Capping Method. *Angew Chem Int Edit* **48**, 5705-5707

27. Sillen, A., Leroy, A., Wieruszeski, J. M., Loyens, A., Beauvillain, J. C., Buee, L., Landrieu, I., and Lippens, G. (2005) Regions of tau implicated in the paired helical fragment core as defined by NMR. *Chembiochem* **6**, 1849-1856

28. Chen, Z. J., and Reif, B. (2004) Measurements of residual dipolar couplings in peptide inhibitors weakly aligned by transient binding to peptide amyloid fibrils. *Journal of biomolecular NMR* **29**, 525-530

29. Chen, Z. J., Krause, G., and Reif, B. (2005) Structure and orientation of peptide inhibitors bound to beta-amyloid fibrils. *J Mol Biol* **354**, 760-776

30. Wagner, G. (1995) The Importance of Being Floppy. *Nature structural biology* **2**, 255-257

31. Camilloni, C., and Vendruscolo, M. (2015) A Tensor-Free Method for the Structural and Dynamical Refinement of Proteins using Residual Dipolar Couplings. *J Phys Chem B* **119**, 653-661

32. Petkova, A. T., Yau, W. M., and Tycko, R. (2006) Experimental constraints on quaternary structure in Alzheimer's beta-amyloid fibrils. *Biochemistry* **45**, 498-512

33. Fawzi, N. L., Ying, J. F., Torchia, D. A., and Clore, G. M. (2012) Probing exchange kinetics and atomic resolution dynamics in high-molecular-weight complexes using dark-state exchange saturation transfer NMR spectroscopy. *Nat Protoc* **7**, 1523-1533

34. Fawzi, N. L., Libich, D. S., Ying, J. F., Tugarinov, V., and Clore, G. M. (2014) Characterizing Methyl-Bearing Side Chain Contacts and Dynamics Mediating Amyloid beta Protofibril Interactions Using C-13(methyl)-DEST and Lifetime Line Broadening. *Angew Chem Int Edit* **53**, 10345-10349

35. Scheidt, H. A., Morgado, I., and Huster, D. (2012) Solid-state NMR Reveals a Close Structural Relationship between Amyloid-beta Protofibrils and Oligomers. *J Biol Chem* **287**, 22822-22826

36. Kheterpal, I., Lashuel, H. A., Hartley, D. M., Wlaz, T., Lansbury, P. T., and Wetzel, R. (2003) A beta protofibrils possess a stable core structure resistant to hydrogen exchange. *Biochemistry* **42**, 14092-14098

37. Cerf, E., Sarroukh, R., Tamamizu-Kato, S., Breydo, L., Derclaye, S., Dufrene, Y. F., Narayanaswami, V., Goormaghtigh, E., Ruysschaert, J. M., and Raussens, V. (2009) Antiparallel beta-sheet: a signature structure of the oligomeric amyloid beta-peptide. *Biochem J* **421**, 415-423

38. Scheidt, H. A., Morgado, I., Rothemund, S., Huster, D., and Fandrich, M. (2011) Solid-State NMR Spectroscopic Investigation of A beta Protofibrils: Implication of a beta-Sheet Remodeling upon Maturation into Terminal Amyloid Fibrils. *Angew Chem Int Edit* **50**, 2837-2840

39. Suzuki, Y., Brender, J. R., Soper, M. T., Krishnamoorthy, J., Zhou, Y. L., Ruotolo, B. T., Kotov, N. A., Ramamoorthy, A., and Marsh, E. N. G. (2013) Resolution of Oligomeric

Species during the Aggregation of A beta(1-40) Using F-19 NMR. *Biochemistry* **52**, 1903-1912

40. Kotarek, J. A., Johnson, K. C., and Moss, M. A. (2008) Quartz crystal microbalance analysis of growth kinetics for aggregation intermediates of the amyloid-beta protein. *Anal Biochem* **378**, 15-24

41. Yamaguchi, T., Matsuzaki, K., and Hoshino, M. (2013) Interaction between soluble A beta-(1-40) monomer and A beta-(1-42) fibrils probed by paramagnetic relaxation enhancement. *Febs Lett* **587**, 620-624

42. Tjernberg, L. O., Naslund, J., Lindqvist, F., Johansson, J., Karlstrom, A. R., Thyberg, J., Terenius, L., and Nordstedt, C. (1996) Arrest of beta-amyloid fibril formation by a pentapeptide ligand. *J Biol Chem* **271**, 8545-8548

43. Ghanta, J., Shen, C. L., Kiessling, L. L., and Murphy, R. M. (1996) A strategy for designing inhibitors of beta-amyloid toxicity. *J Biol Chem* **271**, 29525-29528

44. Mustafi, S. M., Garai, K., Crick, S. L., Baban, B., and Frieden, C. (2010) Substoichiometric inhibition of A beta(1-40) aggregation by a tandem A beta(40-1-Gly8-1-40) peptide. *Biochem Bioph Res Co* **397**, 509-512

45. Ladiwala, A. R. A., Bhattacharya, M., Perchiacca, J. M., Cao, P., Raleigh, D. P., Abedini, A., Schmidt, A. M., Varkey, J., Langen, R., and Tessier, P. M. (2012) Rational design of potent domain antibody inhibitors of amyloid fibril assembly. *Proc Natl Acad Sci USA* **109**, 19965-19970

Chapter 5: Conclusions and Future Outlook

5.1 General Conclusions

In this dissertation, we have explored the mechanism of Aβ aggregation in various environments and their influence on the potential pathway(s) aggregation may proceed. Prior studies demonstrated the role of membrane composition in modulation of Aβ aggregation, and hypothesized the specific role of gangliosides being a culprit of a toxic aggregation pathway (1, 2). Nevertheless, the full role of how gangliosides may contribute mechanistically to this toxic aggregation remained unclear. More generally, many questions remained about how Aβ aggregation proceeds in solution at high resolution. Using a combination of biophysical approaches, namely NMR spectroscopy, we have provided new mechanistic insights into Aβ misfolding that are fundamental to understanding Alzheimer's disease pathogenesis.

Experimental results in Chapter 2 expand on previous investigations of Aβ aggregation in the presence of ganglioside-containing membranes by revealing their role in the membrane disruption process. We found that ganglioside-containing membranes facilitated a two-step mechanism of membrane disruption by which Aβ (i) formed ion-permeable pores and (ii) caused membrane fragmentation in a fiber-dependent and ganglioside-dependent manner. Pore formation had previously been observed for Aβ (3–5); however, our study demonstrated Aβ's ability to cause membrane fragmentation and its dependence lipid composition, namely gangliosides. Additionally, this study accounts for many facets of Aβ toxicity through membrane disruption that were previously poorly explained. First, it sheds light on the mechanism by which

large aggregates of Aβ, which present difficulty in rationalizing their ability to form pores unless disassembled into smaller aggregates (energetically unfavorable), could elicit cytotoxicity. Second, Aβ aggregation is often accompanied by large-scale morphological changes in the membrane that would not be expected or observable by the insertion of small oligomeric pores. Rather, large-scale morphological changes point to physical disruption of membranes.

While Chapter 2 demonstrated a potential mechanism by which Aβ may elicit neurotoxicity, the problem of aggregation remains the ultimate culprit of Aβ pathogenesis and the likely agent to target for development of AD therapeutics. More specifically, it highlights the knowledge lacking in structural morphologies of oligomeric intermediates; the "central dogma" of the amyloid problem (6). The inability to reconcile the morphological features of oligomeric Aβ assemblies lies in the shortcomings, thus far, of high-resolution tools for studying oligomeric structures as well as ongoing fibrillization. In Chapters 3 and 4, we explored promising advances in this regard by developing a method capable of obtaining high-resolution structural information of oligomers *in situ* and implementing new approaches in real-time 2D NMR for amyloid misfolding, respectively.

Few structural models of Aβ oligomers exist (7–10), and this is largely due to their transient nature and heterogeneous structures, making oligomers of a specific conformation difficult to isolate and structural characterize. However, given that heterogeneity is so apparent in amyloid aggregation pathways, it seems that isolation of particular structures would only provide a narrow picture of the overall aggregation scheme. This becomes more evident when considering most of the models that do exist bear a close resemblance to the fiber end-product (7, 11–13), while evidence from lower-resolution techniques (like CD) suggests some, but not all, of the most toxic oligomers have a structure that more closely resembles the Aβ monomer than the

Aβ fiber (14, 15). In Chapter 3, we use MAS NMR spectroscopy on a solution sample of Aβ containing a heterogeneous mixture of oligomers and fibers. Through slow MAS spinning speeds and the use of ^{1}H-^{1}H dipolar interactions, we spectrally filter any signal that might come from the insoluble fibers. By using the ^{1}H/^{1}H RFDR technique, we were able to reveal a dynamic and disordered structure comprised of turns and twists for intermediate sized (5-10 nm) oligomers without purification. In a more general sense, our results demonstrate the value of the RFDR-based 2D ^{1}H/^{1}H experiment in obtaining high-resolution information on supramolecular assemblies not easily amenable to analysis by other biophysical techniques, including solution NMR and other solid-state NMR experiments.

The RFDR experiments offer new avenues to study oligomer structure, but in order to gain mechanistic insight into the process of their assembly will require advancements in pulses sequences with shorter acquisition times. Work in Chapter 4 demonstrates application of recently developed fast acquisition methods of 2D solution NMR pulse sequences towards a more detailed mechanistic understanding of Aβ fiber elongation. A proposed model for a "dock and lock" mechanism of fiber elongation had been proposed previously (16); however, site-specific details of the association steps involved in fiber elongation have been largely absent. Paramagnetic relaxation enhancement experiments using a fibril seed labeled at either A2 or A30 suggest that association of the monomer with the N-terminus of the fiber during the docking stage is rare (17). Our experiments, which analyze the residue specificity of the monomer contacts in the docked state (the initial transient association of monomer to fiber), offer a more detailed view and highlight important differences between the docked state of the monomer in the fibers and protofibers. The central hydrophobic region of monomers (i.e. the sequence KLVFFA from residues 16-21) has the highest affinity for the protofiber surface (18). However,

in mature fibers, the main recognition sequence of the docked state is shifted towards the C-terminus, centered on residues 19-22 (with sequence FFAE) of the incoming monomeric peptide (Figs 4.2 and 4.5). This shift is important, as the KLVFF sequence has been implicated as a site of Aβ40 self-recognition and may result from structural differences between protofibrillar and fibrillar states. Additionally, point mutations between residues F20-E22 give rise to early-onset Alzheimer's disease and usually result in altered Aβ aggregation pathways and fibril structure (19–21). Real-time 2D NMR or similar experiments would need to be performed to provide molecular description of Aβ mutants associated with familial AD.

Thus, the body of work presented in this dissertation implicates the role of Aβ in Alzheimer's disease as a result of the overall of scheme of aggregation, as opposed to an individual toxic species. The heterogeneity of this assembly process emphasizes the difficulty in fully elucidating the specific nature of Aβ's toxicity and further contributes to the uncertainty of pathogenic mechanisms of AD. Nevertheless, the identification of site-specific interactions of Aβ self-assembly demonstrates the advantage of using NMR to establish the sequence of events in a protein aggregation reaction. Today, NMR is arguably the most powerful and well-suited method for doing so as it provides methods to identify the kinetics of aggregation, structures of different aggregate species, or structural transitions taking place during (mis)folding all at the atomic level. While solution- and solid-state NMR have distinct limitations, when combined they offer the ability to attack Aβ aggregation starting from monomeric (solution NMR) or fibrillar (solid-state NMR) species. Herein, the use of a combined solution/solid-state technique demonstrated the possibility for new avenues to probe such aggregation processes altogether; i.e. an approach to directly probe intermediate aggregation without perturbative methods, such as chemical- or photo-crosslinking, freezing, amino acid substitution, or any other type of protein

engineering to stabilize the oligomers. With such insights, NMR is advancing to become an important tool for the study of Aβ aggregation as well as other aggregating proteins implicated in diseases like Parkinson's or Huntington's. Furthermore, as therapeutics for amyloid-related diseases are still inadequate, NMR shows the potential to unveil the interactions of aggregating proteins with drugs.

5.2 Future Outlook

NMR studies of Aβ, and other amyloidogenic proteins, offers continued progress in understanding the molecular basis of amyloid-related diseases. Currently, there are no therapeutics to prevent Alzheimer's disease; however, progress in the area of drug development for amyloidoses, such as transthyretin amyloidosis (22, 23), provides confidence that anti-amyloid drug targets are viable therapeutics for other amyloid-related diseases. The difficulty, however, with diseases such as Alzheimer's and Parkinson's diseases is likely due to the conformational plasticity of intrinsically disordered proteins as drug targets. NMR's ability to probe the (mis)folding landscape would help identify such targets, and potentially establish the universality of the mechanisms of such processes uncovered herein.

An intriguing result from our studies discussed in Chapter 2 of membrane-mediated modifications of Aβ aggregation is the ability of gangliosides to facilitate a specific aggregation pathway. Currently, the only membrane bound models of Aβ that exist are high-resolution structures of Aβ monomers bound to detergent micelles and computer simulations of channels or oligomers constructed from fragments of the Aβ fiber (24–26). The computer simulations of Aβ channels have been invaluable in identifying molecular features of potential Aβ pore structures, yet more structural data is necessary to further refine computational models and to collectively understand all forms of membrane disruption. It is apparent that membranes have a two-fold

effect on Aβ: (i) membranes can greatly accelerate the rate of fibrillization and (ii) Aβ can directly disrupt plasma and possibly organelle membranes. The cell membrane therefore contributes to Aβ toxicity as both a site for the accumulation/nucleation of toxic oligomers and as a target for their cytotoxic effect. Consequently, it is imperative to better understand how environmental factors within the cell membrane (such as the lipid composition) contribute to structural polymorphisms of Aβ oligomers. Such data will help us understand both how membrane disruption occurs and possibly if certain cell types are more sensitive to Aβ toxicity due to an altered lipid composition, generating a more toxic conformation.

The potential of the $^{1}H/^{1}H$ RFDR approach presented in Chapter 3 offers new avenues for the study of human-derived samples of amyloid aggregates. A study from Tycko and co-workers reported structures of Aβ fibril structures derived from post-mortem brain tissue (27). While the work from Lu et al was a major breakthrough for AD reserach, high-resolution characterization of such samples still required seeded growth of synthetic $^{13}C,^{15}N$-labeled Aβ40 peptide. The sensitivity of the ^{1}H nucleus limits the need for large sample quantities typical of many NMR experiments. Furthermore, ^{1}H-^{1}H through-space correlations are routinely used for determining protein structure and dynamics (28–30). Here, we were unable to solve a distinct structure of an Aβ oligomer species due to its highly disordered nature limiting the number of measurable distant constraints. Our experiments did, however, reveal the ability to achieve atomic resolution and perhaps indicates that as a future structure-determination method may necessitate isotopic labelling of samples or development of pulse sequences with improved sensitivity.

A deeper related question is how such Aβ aggregates self-associate to form heterogeneous intermediates, yet distinct polymorphs of amyloid fibrils. The real-time 2D NMR methods implemented for the study in Chapter 4 demonstrated to some degree the hierarchrical

nature of Aβ fiber elongation. Studies in our laboratory are presently ongoing to expand on the ability of the Aβ42 alloform to cross-seed aggregation, and vice versa. Yet, if there is dependence on a particular polymorphic structure to seed Aβ aggregation, then such studies can also be extended to observe how human brain-derived samples facilitate Aβ self-assembly. The study by Lu et al found that Aβ fibrils derived from different AD patients were structurally distinct (27). Given the inherent polymorphism of Aβ fibrils, this raises a number of intriguing questions about distinct pathways of Aβ assembly. Is the initial fibril formation stochastic, and then the same form predominantly replicated? Does a particularly polymorphic structure persist because of stronger seeding capabilities? Does particular polymorphic structure evade breakdown by protein quality control machinery and/or appropripate clearance? Do patients with different clinical histories give rise to similar mechanisms of self-assembly?

Answers to such questions are likely only to be elucidated by further studies of larger patient populations. The NMR methods used here provide a valuable suite of tools to generate insight into the mechanism of Aβ self-assembly and the aggregation of amyloids, broadly. Beyond the above applications, the toxic nature of Aβ has yet to be established as causative in AD and this may be due to failure, thus far, in our inability to develop therapeutics capable of preventing Aβ aggregation *in vivo*. Our inability to do so could directly result from our lack of understanding of the intermediate states leading to fibril formation or aggregates that propagate unfavorable Aβ aggregation. In this respect, better understanding the link between environmental factors (such as lipid composition, metal ions, etc.) and their resultant effects on initial misfolding, nucleation of fibril formation, and/or propagation of fibril polymorphs are likely a key aspect to understanding Alzheimer's disease and other amyloid-related diseases.

5.3 References

1. Matsuzaki, K., Kato, K., and Yanagisawa, K. (2010) Abeta polymerization through interaction with membrane gangliosides. *Biochim. Biophys. Acta*. **1801**, 868–77

2. Kakio, A., Nishimoto, S., Yanagisawa, K., Kozutsumi, Y., and Matsuzaki, K. (2002) Interactions of amyloid beta-protein with various gangliosides in raft-like membranes: importance of GM1 ganglioside-bound form as an endogenous seed for Alzheimer amyloid. *Biochemistry*. **41**, 7385–7390

3. Arispe, N., Pollard, H. B., and Rojas, E. (1993) Giant multilevel cation channels formed by Alzheimer disease amyloid beta-protein [A beta P-(1-40)] in bilayer membranes. *Proc Natl Acad Sci U S A*. **90**, 10573–10577

4. Lal, R., Lin, H., and Quist, A. (2007) Amyloid beta ion channel: 3D structure and relevance to amyloid channel paradigm. *Biochim. Biophys. Acta - Biomembr.* **1768**, 1966–1975

5. Capone, R., Jang, H., Kotler, S. A., Kagan, B. L., Nussinov, R., and Lal, R. (2012) Probing structural features of Alzheimer's amyloid-β pores in bilayers using site-specific amino acid substitutions. *Biochemistry*. **51**, 776–85

6. Benilova, I., Karran, E., and De Strooper, B. (2012) The toxic Aβ oligomer and Alzheimer's disease: an emperor in need of clothes. *Nat. Neurosci.* **15**, 349–57

7. Chimon, S., Shaibat, M. A., Jones, C. R., Calero, D. C., Aizezi, B., and Ishii, Y. (2007) Evidence of fibril-like β-sheet structures in a neurotoxic amyloid intermediate of Alzheimer's β-amyloid. *Nat. Struct. Mol. Biol.* **14**, 1157–64

8. Ahmed, M., Davis, J., Aucoin, D., Sato, T., Ahuja, S., Aimoto, S., Elliott, J. I., Van Nostrand, W. E., and Smith, S. O. (2010) Structural conversion of neurotoxic amyloid-beta(1-42) oligomers to fibrils. *Nat. Struct. Mol. Biol.* **17**, 561–567

9. Scheidt, H. a, Morgado, I., Rothemund, S., Huster, D., and Fändrich, M. (2011) Solid-state NMR spectroscopic investigation of Aβ protofibrils: implication of a β-sheet remodeling upon maturation into terminal amyloid fibrils. *Angew. Chem. Int. Ed. Engl.* **50**, 2837–40

10. Yu, L., Edalji, R., Harlan, J. E., Holzman, T. F., Lopez, A. P., Labkovsky, B., Hillen, H., Barghorn, S., Ebert, U., Richardson, P. L., Miesbauer, L., Solomon, L., Bartley, D., Walter, K., Johnson, R. W., Hajduk, P. J., and Olejniczak, E. T. (2009) Structural characterization of a soluble amyloid beta-peptide oligomer. *Biochemistry*. **48**, 1870–7

11. Scheidt, H. a, Morgado, I., and Huster, D. (2012) Solid-state NMR reveals a close structural relationship between amyloid-β protofibrils and oligomers. *J. Biol. Chem.* **287**, 22822–6

12. Tay, W. M., Huang, D., Rosenberry, T. L., and Paravastu, A. K. (2013) The Alzheimer's amyloid-β(1-42) peptide forms off-pathway oligomers and fibrils that are distinguished structurally by intermolecular organization. *J. Mol. Biol.* **425**, 2494–508

13. Lendel, C., Bjerring, M., Dubnovitsky, A., Kelly, R. T., Filippov, A., Antzutkin, O. N., Nielsen, N. C., and Härd, T. (2014) A Hexameric Peptide Barrel as Building Block of Amyloid-β Protofibrils. *Angew. Chem. Int. Ed. Engl.* **53**, 12756–60

14. Ono, K., Condron, M. M., and Teplow, D. B. (2009) Structure-neurotoxicity relationships of amyloid beta-protein oligomers. *Proc. Natl. Acad. Sci. U. S. A.* **106**, 14745–50

15. Ladiwala, A. R. a, Litt, J., Kane, R. S., Aucoin, D. S., Smith, S. O., Ranjan, S., Davis, J., Van Nostrand, W. E., and Tessier, P. M. (2012) Conformational differences between two amyloid β oligomers of similar size and dissimilar toxicity. *J. Biol. Chem.* **287**, 24765–73

16. Esler, W. P., Stimson, E. R., Jennings, J. M., Vinters, H. V., Ghilardi, J. R., Lee, J. P., Mantyh, P. W., and Maggio, J. E. (2000) Alzheimer's disease amyloid propagation by a template-dependent dock- lock mechanism. *Biochemistry*. **39**, 6288–6295

17. Yamaguchi, T., Matsuzaki, K., and Hoshino, M. (2013) Interaction between soluble Aβ-(1-40) monomer and Aβ-(1-42) fibrils probed by paramagnetic relaxation enhancement. *FEBS Lett.* **587**, 620–624

18. Fawzi, N. L., Ying, J., Ghirlando, R., Torchia, D. A., and Clore, G. M. (2011) Atomic-resolution dynamics on the surface of amyloid-β protofibrils probed by solution NMR. *Nature*. **480**, 268–272

19. Tycko, R., Sciarretta, K. L., Orgel, J. P. R. O., and Meredith, S. C. (2009) Evidence for novel beta-sheet structures in Iowa mutant beta-amyloid fibrils. *Biochemistry*. **48**, 6072–84

20. Lee, J., Culyba, E. K., Powers, E. T., and Kelly, J. W. (2011) Amyloid-beta forms fibrils by nucleated conformational conversion of oligomers. *Nat Chem Biol*. **7**, 602–609

21. Yates, E. A., Cucco, E. M., Legleiter, J., Hall, C., Box, P. O., Virginia, W., and States, U. (2011) Point Mutations in Aβ Induce Polymorphic Aggregates at Liquid/Solid Interfaces

22. Razavi, H., Palaninathan, S. K., Powers, E. T., Wiseman, R. L., Purkey, H. E., Mohamedmohaideen, N. N., Deechongkit, S., Chiang, K. P., Dendle, M. T. A., Sacchettini, J. C., and Kelly, J. W. (2003) Benzoxazoles as transthyretin amyloid fibril inhibitors: synthesis, evaluation, and mechanism of action. *Angew. Chem. Int. Ed. Engl.* **42**, 2758–61

23. Coelho, T., Maia, L. F., Martins da Silva, A., Waddington Cruz, M., Plante-Bordeneuve, V., Lozeron, P., Suhr, O. B., Campistol, J. M., Conceicao, I. M., Schmidt, H. H.-J., Trigo, P., Kelly, J. W., Labaudiniere, R., Chan, J., Packman, J., Wilson, A., and Grogan, D. R. (2012) Tafamidis for transthyretin familial amyloid polyneuropathy: A randomized, controlled trial. *Neurology*. **79**, 785–792

24. Jang, H., Connelly, L., Arce, F. T., Ramachandran, S., Lal, R., Kagan, B. L., and Nussinov, R. (2013) Alzheimer's disease: which type of amyloid-preventing drug agents to employ? *Phys. Chem. Chem. Phys.* 10.1039/c3cp00017f

25. Jang, H., Zheng, J., Lal, R., and Nussinov, R. (2008) New structures help the modeling of toxic amyloidbeta ion channels. *Trends Biochem. Sci.* **33**, 91–100

26. Jarvet, J., Danielsson, J., Damberg, P., Oleszczuk, M., and Gräslund, A. (2007) Positioning of the Alzheimer Abeta(1-40) peptide in SDS micelles using NMR and paramagnetic probes. *J. Biomol. NMR*. **39**, 63–72

27. Lu, J.-X., Qiang, W., Yau, W.-M., Schwieters, C. D., Meredith, S. C., and Tycko, R. (2013) Molecular structure of β-amyloid fibrils in Alzheimer's disease brain tissue. *Cell*. **154**, 1257–68

28. Riek, R., Güntert, P., Döbeli, H., Wipf, B., and Wüthrich, K. (2001) NMR studies in aqueous solution fail to identify significant conformational differences between the monomeric forms of two Alzheimer peptides with widely different plaque-competence, Aβ(1-40) ox and Aβ(1-42) ox. *Eur. J. Biochem.* **268**, 5930–5936

29. Riek, R., Hornemann, S., Wider, G., Glockshuber, R., and Wüthrich, K. (1997) NMR characterization of the full-length recombinant murine prion protein, mPrP(23-231). *FEBS Lett.* **413**, 282–8

30. Wälti, M. A., Orts, J., Vögeli, B., Campioni, S., and Riek, R. (2015) Solution NMR Studies of Recombinant Aβ(1-42): From the Presence of a Micellar Entity to Residual β-Sheet Structure in the Soluble Species. *Chembiochem*. 10.1002/cbic.201402595

Appendix A. Supporting Information for Chapter 2

A.1. Additional Experimental Methods:

A.1.1. Materials:

Aβ40 (97% purity) was purchased from Anaspec (Fremont, CA). 1-palmitoyl-2- oleoyl-*sn*-glycero-3-phosphocholine (POPC), 1-palmitoyl-2-oleoyl-*sn*-glycero-3-phospho-L-serine sodium salt (POPS), total ganglioside extract (Brain, Porcine-Ammonium Salt), and total brain lipid extract were purchased from Avanti Polar lipids Inc. (Alabaster, AL). Ferric chloride hexahydrate, ammonium thiocyanate, and Fura-2 pentapotassium salt were purchased from Sigma-Aldrich (St. Louis, MO). 6-Carboxyfluorescein was purchased from Fluka.

A.1.2. Model membrane preparation.

Large unilamellar vesicles (LUV) of POPC/POPS 7/3, POPC/POPS/ganglioside 5.5/3/1.5, and total lipid brain extract (TLBE) were prepared from a chloroform solution of lipids in the desired ratio. The solution was gently dried under nitrogen flow and then placed under a high vacuum overnight to further evaporate any residual solvent. The obtained lipid film was rehydrated with a buffer solution (10 mM phosphate buffer solution, pH 7.4, 100 mM NaCl), to yield a final concentration of 4 mg/ml, and dispersed by vigorous stirring. The resulting solution was extruded 23 times through a 100 nm polycarbonate Nucleopore membrane filter (Whatman) mounted on a mini-extruder in order to obtain LUV with an average diameter of 100 nm.

To prepare dye-filled LUV, the dry lipid film was hydrated with a buffer solution containing 6-carboxyfluorescein (10 mM phosphate buffer solution, 70 mM 6-carboxyfluorescein, 100 mM NaCl, pH 7.4) or 100 μM Fura 2 pentapotassium salt (10 mM Hepes buffer solution, 200 μM EGTA, 100 mM NaCl, pH 7.4) to a final concentration of 10 mg/ml, which was followed by the procedures described above. Removal of any non-encapsulated 6-carboxyfluorescein or Fura 2 pentapotassium salt was performed by running the extruded LUV solution through a Sephadex G50 gel exclusion column (Sigma-Aldrich) and collecting the first colored band detectable under visible or UV light which contained the separated dye-containing vesicles. The final lipid concentrations were measured using the Stewart assay. All solutions were freshly prepared before each experiment.

A.1.3. Dye leakage assay.

Membrane leakage experiments were carried out using 6- carboxyfluorescein-filled LUV composed of POPC/POPS 7/3, POPC/POPS/gangliosides 5.5/3/1.5 and total brain extract. Membrane leakage was detected by measuring the increase in fluorescence 6-carboxyfluorescein resulting from its dilution and subsequent dequenching following membrane leakage. Samples were prepared by first diluting the dye-filled vesicles solution with buffer solution (10 mM phosphate buffer solution, 100 mM NaCl, pH 7.4) to a final concentration of 0.2 mg/ml. The presence of 100 mM NaCl in the buffer ensured that the osmotic pressure exerted on the membrane bilayer by the dye itself had no effect on dye release from the vesicles. The NaCl concentration was optimized by varying the NaCl concentration in the buffer outside the LUVs until baseline leakage in the absence of peptide was negligible over several days. To initiate membrane disruption, 1 or 2 μl of the peptide stock solution was added to 100 μl of the LUV solution to obtain a final peptide concentration of 5 or 10 μM , respectively. Experiments

were carried out in Corning 96 well non-binding surface plates. Time traces were recorded using Biotek Synergy 2 plate reader using a 2 nm bandpass filters at 494 nm excitation and 520 nm emission at room temperature, shaking samples for 10 seconds before each read. The fraction of dye released was calculated by:

$$\text{Fraction of dye released} = (I - I_0)/(I_{100} - I_0)$$

where I is the emission intensity of the sample, I_0 is the emission intensity obtained in theabsence of peptide (baseline control) and I_{100} is the emission intensity obtained after adding 1 µl of Triton X-100, a detergent which acted as a positive control to give 100% leakage.

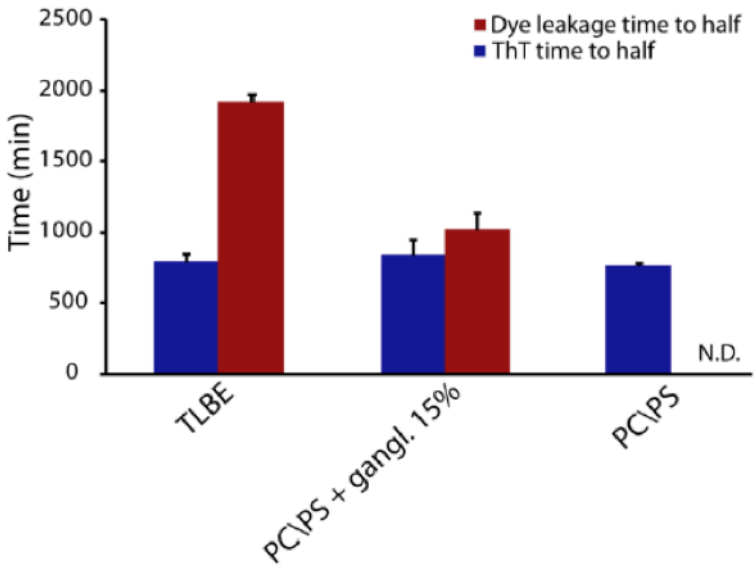

Figure A.1 Timescales of dye leakage and fiber formation.
Comparison between $t_{1/2}$, the time for the intensity to reach one half the final value, for 0.2 mg/ml total brain extract (TLBE), POPC/POPS/Ganglioside (5.5/3/1.5), and POPC/POPS (7/3) LUVs in the dye leakage and Thioflavin T assays.

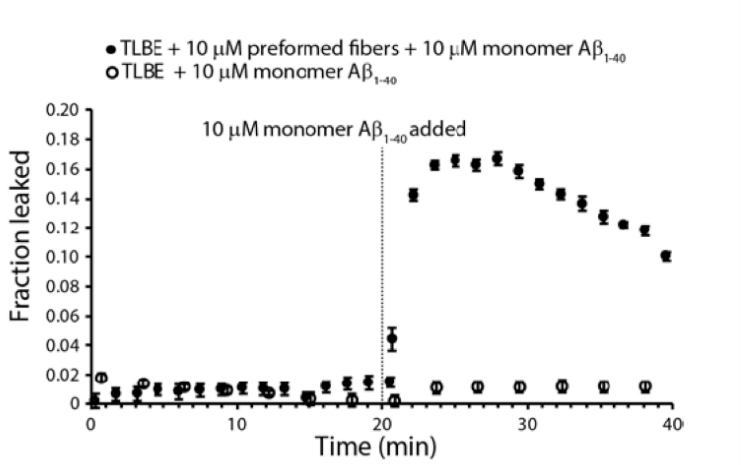

Figure A.2 Membrane disruption induced by seeded fiber growth of Aβ40 measured by the 6-carboxyfluorescein dye leakage assay.
Release of 6-carboxyfluorescein induced by the seeded growth of Aβ40 from 0.2 mg/ml total brain extract (TLBE) LUVs. Neither freshly dissolvedAβ40 (10 μM) or performed Aβ40 fibers (10 μM) caused dye release within the timescale of the experiment. Addition of freshly dissolved Aβ40 to preformed fibers (indicated by the dashed line) caused immediate membrane disruption. Experiments were performed at room temperature in 10 mM phosphate buffer, 100 mM NaCl, pH 7.4; results are the average of three measurements.

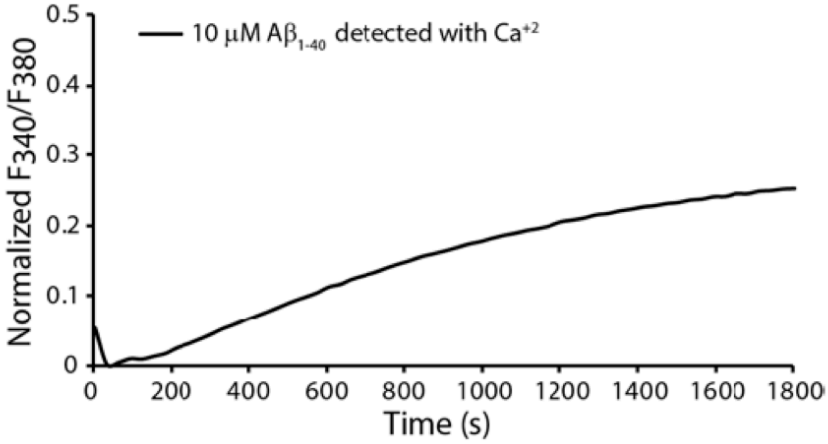

Figure A.3 Kinetics of calcium influx into LUVs after the addition of freshly dissolved Aβ40.
Calcium ion influx detected by Fura 2 encapsulated in 0.2 mg/ml total lipid brain extract LUVs following the simultaneous addition of Ca+2 and 10 μM Aβ40.

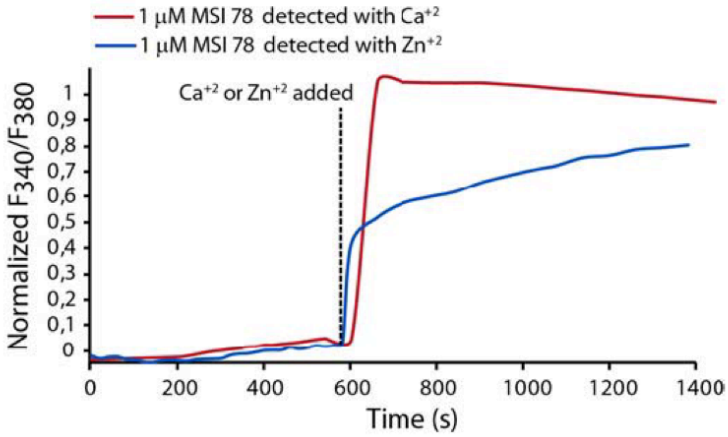

Figure A.4 Fura 2 is sensitive to membrane disruption by both Zn^{2+} and Ca^{2+}.
Influx of calcium (red line) and zinc (blue line) ions induced by 1 μM MSI-78 on 0.2 mg/ml total brain extract LUVs. Freshly dissolved MSI-78 was added to each sample at time zero, Ca^{2+} or Zn^{2+} was added at 600 seconds as indicated by the dashed line.

Appendix B. Supporting Information for Chapter 3

B.1. Supplementary Figures

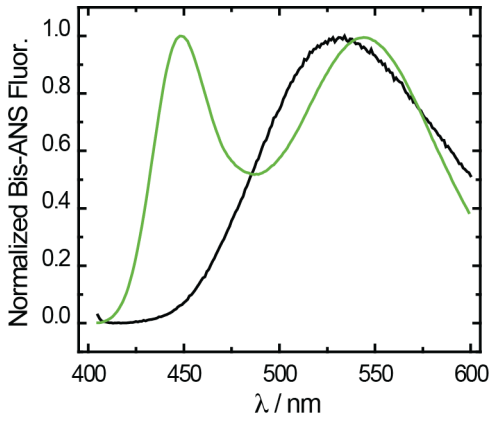

Figure B.1 Characterizing the aggregated $A\beta_{1\text{-}40}$ sample.
The bis-ANS fluorescence assay was used to compare normalized bis-ANS fluorescence in solution (black) to its emission spectrum upon binding isolated $A\beta_{1\text{-}40}$ fibrils (green).

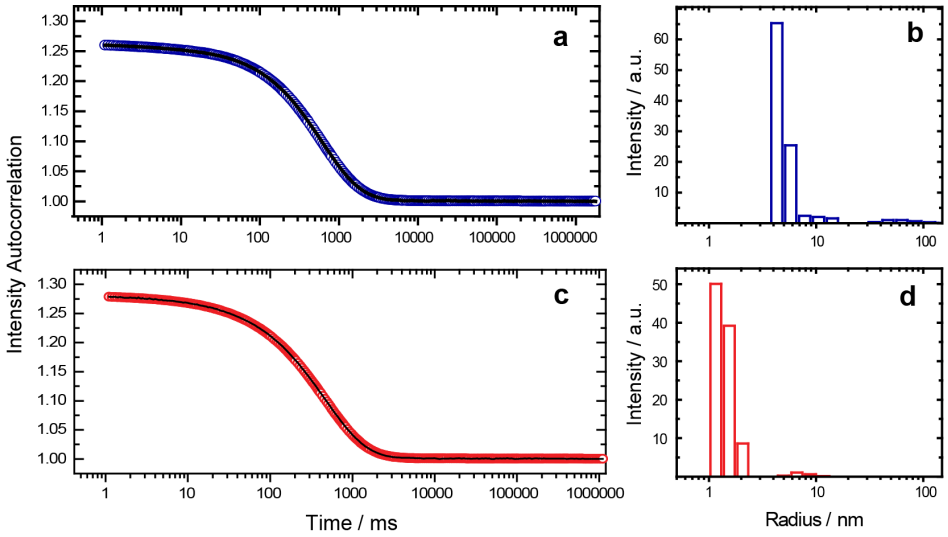

Figure B.2 DLS studies on the spin-X-isolated oligomer and freshly dissolved samples of $A\beta_{1\text{-}40}$. (a, b) The autocorrelation (a, blue circles) with a regularization fit and the corresponding distribution (b) of hydronamic radii obtained from the fitted autocorrelation of the spin-X isolated oligomer. DLS studies on the freshly dissolved $A\beta_{1\text{-}40}$ sample (c, d) showing that the initial population of $A\beta_{1\text{-}40}$ is primarily monomeric with some low order oligomers (dimers or trimers). This is apparent through a regularization fit of the autocorrelation (c) yielding a distribution of hydronamic radii (d) of the freshly dissolved $A\beta_{1\text{-}40}$ sample.

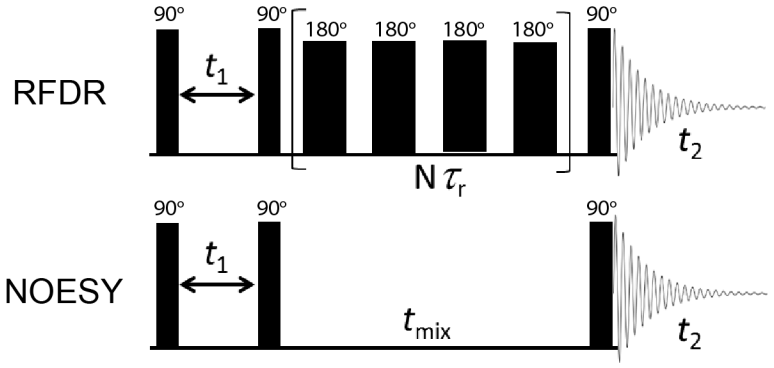

Figure B.3 The two-dimensional RFDR-based (top) and NOESY (bottom) ^{1}H/^{1}H chemical shift correlation experiments used in this study.

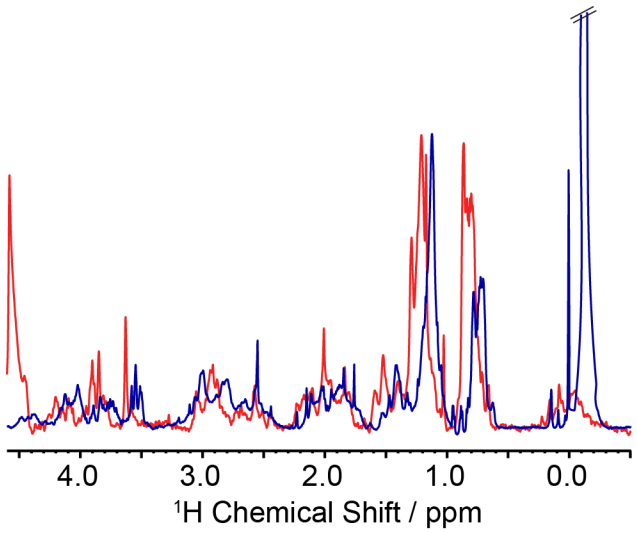

Figure B.4 The aggregated $A\beta_{1\text{-}40}$ sample shows strong up-field shifts.
An overlay of the 1D ^{1}H MAS NMR spectra of freshly dissolved $A\beta_{1\text{-}40}$ (red) and the unfiltered, disordered $A\beta_{1\text{-}40}$ oligomer (blue) acquired at 37 °C under 2.7 kHz MAS in 100% D_2O, 10 mM sodium phosphate buffer, pH 7.4.

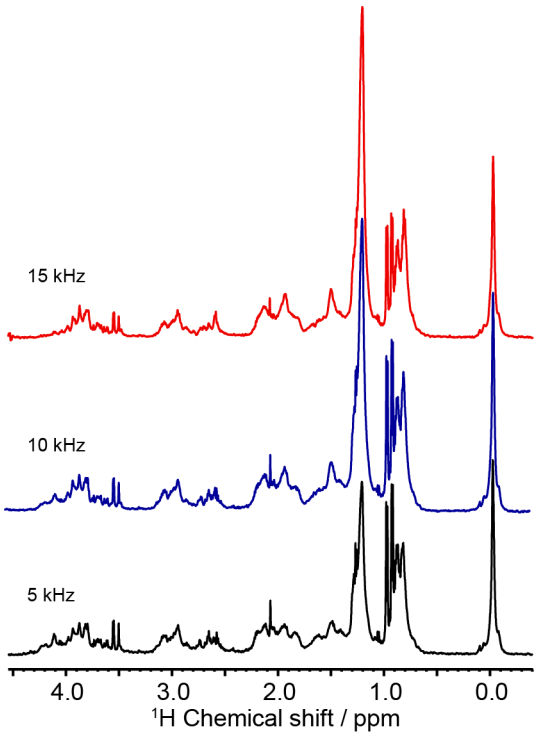

Figure B.5 1D ^{1}H MAS spectra acquired under increasing MAS rates on the filtered disordered $A\beta_{1-40}$ oligomer.
Spectra were acquired at 600 MHz in 100% D2O, 10 mM phosphate buffer, pH 7.4 at 25 ºC. the filtered oligomer sample was lyophilized and re-hydrated to double its initial concentration, making for a total Aβ40 concentration of ~35 μM.

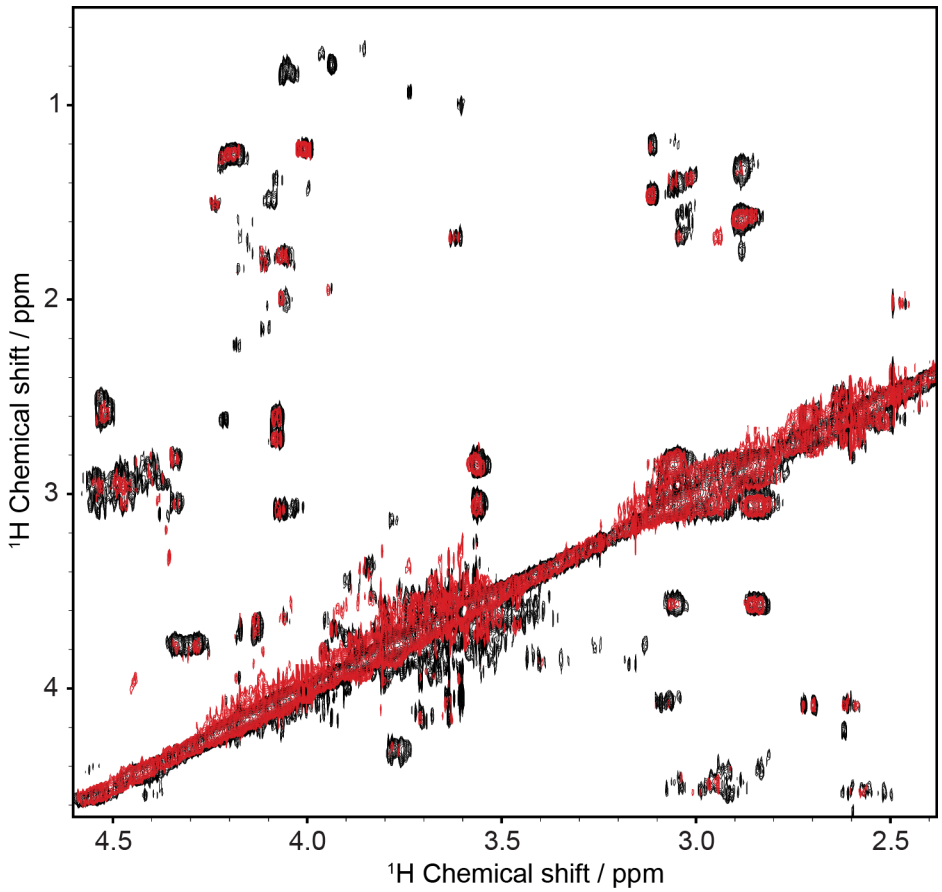

Figure B.6 An overlay of the aliphatic and alpha proton regions of RFDR-based 2D $^{1}H/^{1}H$ spectra acquired using mixing times of 20 ms (red) and 50 ms (black) on the aggregated $A\beta_{1-40}$ sample.
The spectra were acquired at 37 °C with an MAS rate of 2.7 kHz in 100% D_2O, 10 mM phosphate buffer, pH 7.4. The slow MAS rate used here serves to insufficiently average the dipole-dipole interactions of the disordered oligomer such that the RFDR pulse sequence can be used to recouple its "residual" dipolar couplings under MAS conditions. The fact that a well-resolved RFDR-based 2D $^{1}H/^{1}H$ chemical shift correlation spectrum is obtained strongly suggests that this soluble, oligomer species is sufficiently large for the usage of such recoupling methods. Additionally, the low MAS rates insufficiently averages the ^{1}H-^{1}H dipolar couplings of the fibrillar species present in the aggregated $A\beta_{1-40}$ sample. Thus, the RFDR-based 2D $^{1}H/^{1}H$ methodology effectively acts as a filter for intermediate aggregates of $A\beta_{1-40}$. These spectra were assigned by using the 2D $^{1}H/^{1}H$ TOCSY spectrum of the filtered oligomer under both static and MAS conditions (see figures S4 and S7). Assignments of the two TOCSY spectra were guided by a previously assigned spectrum in the following study: Vivekanandan et al. BBRC, 2011, 411, 312-16.

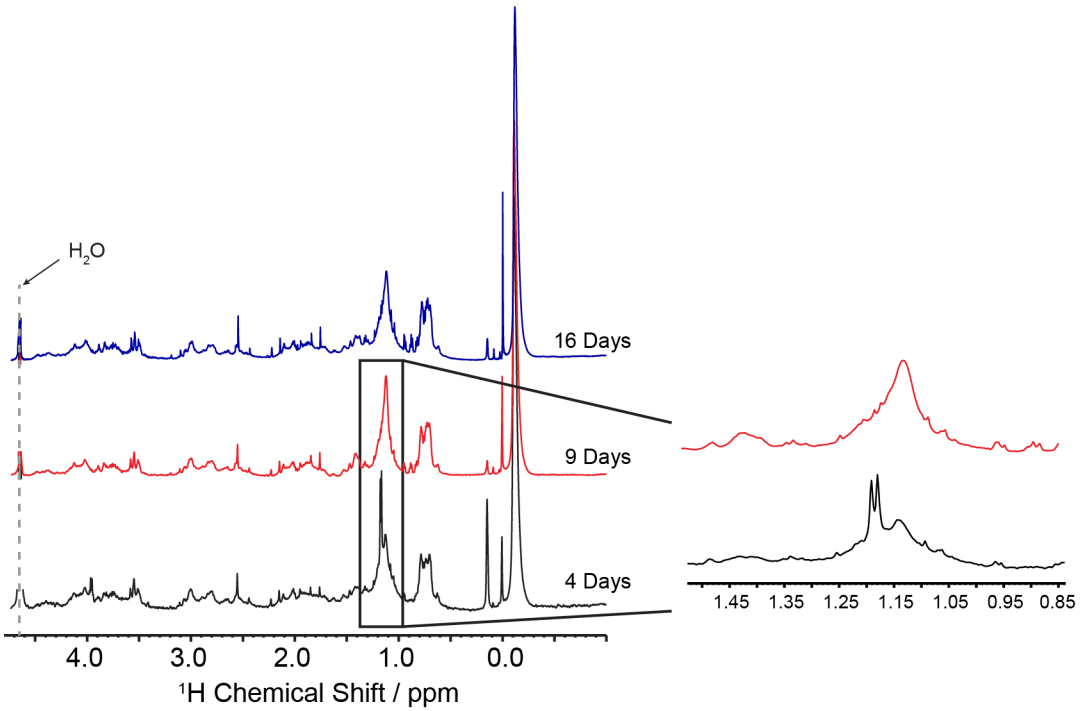

Figure B.7 Time-course 1D ^{1}H MAS NMR spectra of the aggregated A$\beta_{1\text{-}40}$ sample, containing the disordered oligomer.

Little difference is observed in the 1D ^{1}H spectral profiles over the same timeframe for which the RFDR-based 2D ^{1}H/^{1}H experiments were performed, indicating the disordered oligomer is stable over this time period. The initial time point of 4 days marks the completion of sample preparation period described in the experimental procedures and the starting point for all subsequent measurements performed on the disordered A$\beta_{1\text{-}40}$ oligomer. While few changes are seen over this 16-day period, between 4 days and 9 days there are several distinct changes occurring. The oligomer peaks ca. 0.15 ppm undergoes a drastic loss of signal between 4 and 9 days. Additionally, the doublet ca. 1.2 ppm is broadened beyond detection. Collectively, this would suggest 1) a heterogeneous mixture of A$\beta_{1\text{-}40}$ oligomer species present at 4 days and 2) that the disordered oligomer(s) is growing in size over the course of 16 days.

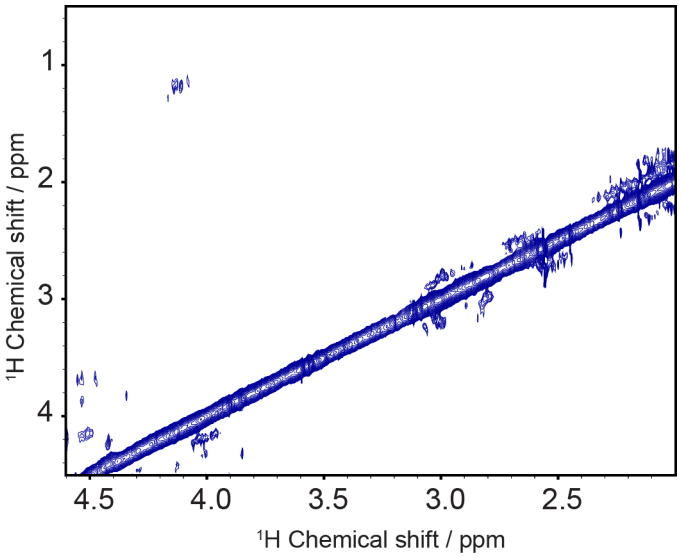

Figure B.8 Two-dimensional ^{1}H/^{1}H NOESY experiments under 2.7 kHz MAS on the mixed fiber and oligomer sample of $A\beta_{1-40}$.
The spectrum was acquired with a 50 ms mixing time at 600 MHz in 100% D_2O, 10 mM sodium phosphate buffer, pH 7.4, at 37 °C, and corresponds to the same sample used in Fig. 2 of the main text.

Appendix C. Supporting Information for Chapter 4

C.1. Materials and Methods

C.1.1. Preparation of Aβ samples:

Unlabeled samples of $A\beta_{1-40}$ were purchased from Genscript U.S.A., Inc (Piscataway, NJ). Uniformly ^{15}N-labeled $A\beta_{1-40}$ samples were purchased from rPeptide (Bogart, GA). To remove preformed aggregates, the purified peptide was dissolved in 1% ammonium hydroxide (v/v) at a concentration of 1 mg/ml followed by removal of the solvent by lyophilization for 24 hours in aliquots of 0.1 mg. The aliqouted peptide was then stored at -20 ^{O}C and only used once.

Preparation of a primarily monomeric $A\beta_{1-40}$ sample was performed as described previously (1). Briefly, 0.1 mg of the lyophilized peptide was first dissolved in 3 µl of DMSO and sonicated until the peptide was solubilized. The peptide solution was then hydrated in H_2O (or 10% D_2O for NMR measurements), buffered in 20 mM phosphate (pH 7.4), 50 mM NaCl and diluted to final peptide concentration of 76 µM (0.1 mg in 300 µl). The peptide concentration was confirmed by UV absorbance at 280 nm (ε_{280} = 1490 M^{-1} cm^{-1})

For seeded NMR experiments, a fibrillar $A\beta_{1-40}$ sample was prepared as described previously (2). The peptide was dissolved directly into a solution of 50 mM NaCl, 20 mM phosphate buffer with pH 7.4, 0.01% NaN_3 and the peptide concentration was adjusted to 150 µM (confirmed by UV absorbance). The sample was then kept at 37 °C with shaking for 48 hrs; conditions that produce a predominantly fibril sample of $A\beta_{1-40}$.

C.1.2. Solution NMR spectroscopy:

Solution NMR experiments were performed on a Bruker Avance 600 MHz spectrometer equipped with a 5 mm cryogenic probe or on a Bruker Avance III 500 MHz NMR spectrometer equipped with a 5 mm SMART probe. NMR experiments were performed at 10 °C, 25 °C, or 37 °C. Prior to adding a fibril seed to the NMR tube containing monomeric $A\beta_{1-40}$, a band-Selective Optimized-Flip-Angle Short-Transient HMQC spectrum was acquired to compare differences immediately before and after titration of fibrillar Aβ. Assignments of the monomer spectra were taken from previously assigned spectra found in the literature (3).

To monitor $A\beta_{1-40}$ aggregation with atomic resolution, real-time 2D NMR experiments were performed by consecutively acquiring ^{1}H-^{15}N SOFAST-HMQC spectra, with each spectrum collected over ~20 min. For seeded real-time HSQC experiments, $A\beta_{1-40}$ fibril seeds were added to monomer solutions at concentrations of 5% and up to 30% of the total peptide concentration. At a 1:10 monomer to fiber ratio and 10 °C, real-time HSQC could be used to track the time-course depletion of monomer HSQC peaks in a site-specific manner. HSQC peak intensities of individual residues were plotted and fit to a single exponential equation. Real-time HSQC experiments were carried out and analyzed in similar fashion at both 25 °C and 37 °C.

Diffusion coefficients were obtained from DOSY (diffusion ordered spectroscopy) NMR experiments (4) for the free $A\beta_{1-40}$ monomer and in the presence of fibril seeds at different time points. All the experiments were performed using Bruker Avance 500 MHz NMR spectrometer equipped at 283 K. A series of one-dimensional ^{1}H NMR spectra were recorded with incremented values of the gradient amplitude from 2% to 95% keeping 12 ppm spectral width, 96 scans and 4 dummy scans. Before Fourier transformation, an exponential window function of 2 Hz line broadening was applied followed by zeroth and first order phase as well as baseline

correction was done manually. Diffusion coefficients were calculated from the following Stejskal–Tanner equation (5)

$$I=I_o \exp\left[-Dg^2\delta^2\gamma^2\left(\nabla-\frac{\delta}{3}\right)\right] \quad \text{.....(1)}$$

where I is the signal intensities at each gradient strength and I_o is the signal intensity in the absence of gradient pulse. D the diffusion coefficient, g is the gradient strength amplitude, δ is the duration of the gradient pulse, γ is the gyromagnetic ratio of ^1H, and ∇ is the diffusion time.

C.1.3. Transmission electron microscopy:

Fibrillar samples of $A\beta_{1\text{-}40}$ for transmission electron microscopy (TEM) analysis were deposited on continuous films on copper rhodium 100 mesh grids (Electron Microscopy Services, EMS, Hartfield, PA). Prior to adding samples, the grids were charged using a glow discharger for 15 s at 30 mA negative discharge. Fibrillar samples at a concentration of 150 μM were adsorbed to the grids for 2 minutes prior to rinsing with a 10 μL drop of freshly filtered 2% uranyl acetate (EMS) for 15 s before blotting excess stain. Samples were analyzed using a Philips CM-100 microscope operating at 80 kV.

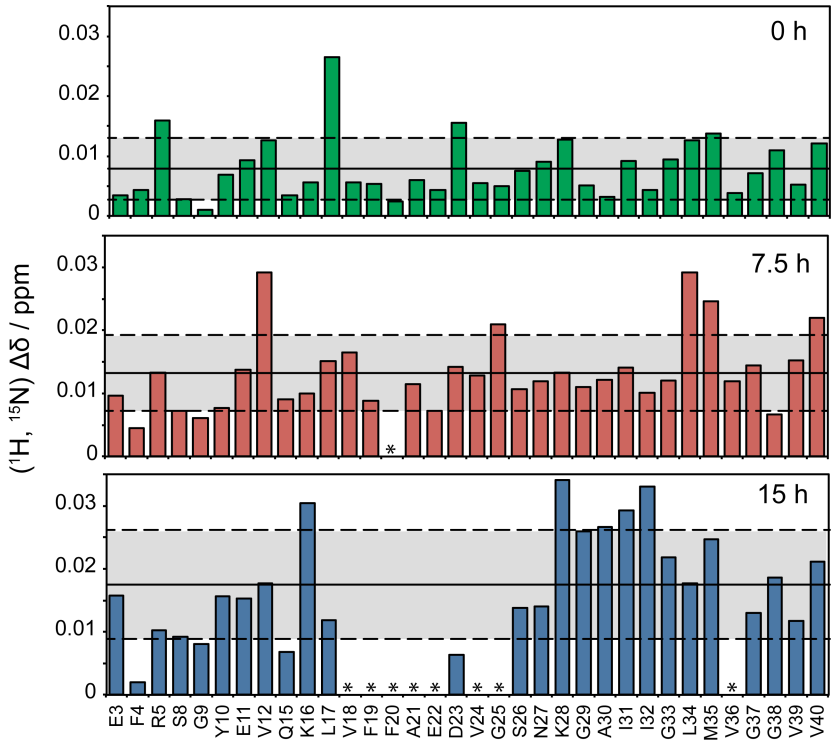

Figure C.1 Chemical shift perturbations of $A\beta_{1\text{-}40}$ over time following titration of $A\beta_{1\text{-}40}$ fibers.
The chemical shift perturbation was taken as the difference between the time point before and after fiber addition using the following equation:

$$\Delta\delta = \sqrt{(\Delta\delta N \times 0.2)^2 + (\Delta\delta H)^2}$$

Solid lines are the average chemical shift perturbations and dotted lines are the average plus/minus one standard deviation.

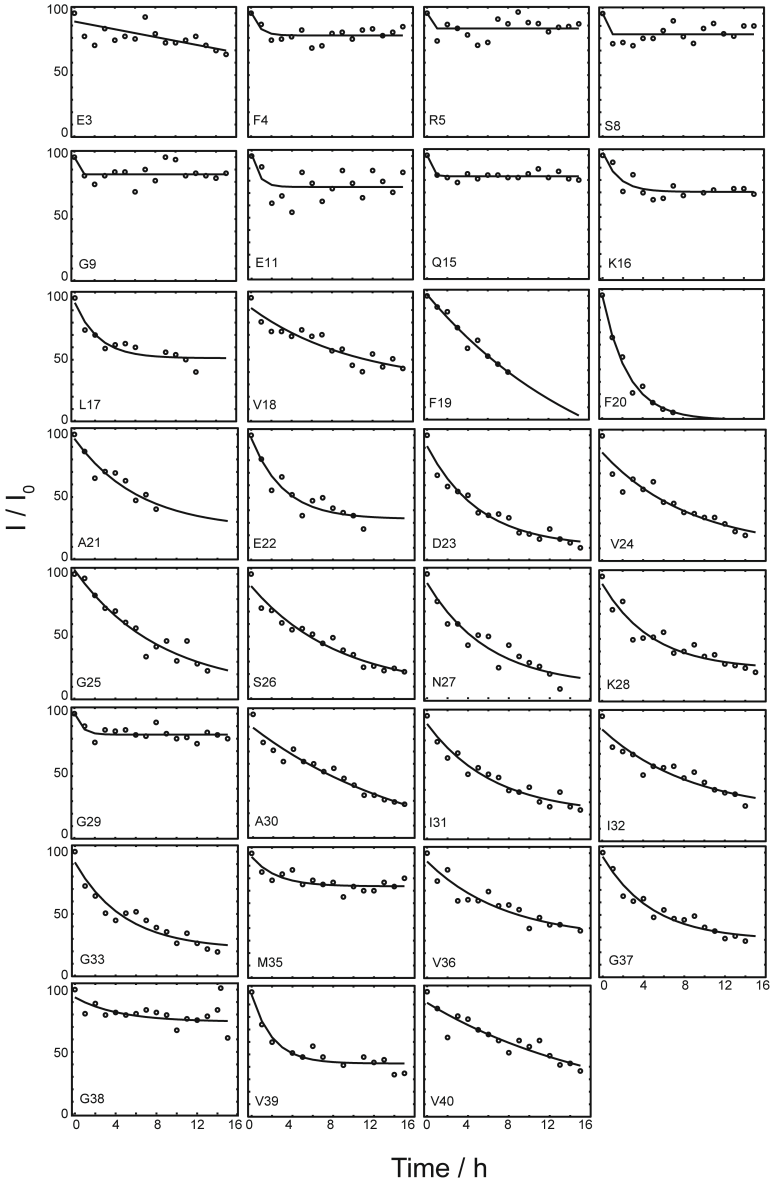

Figure C.2 Time-course intensity changes of HSQC peaks of a seeded Ab40 sample at 10 ºC.
All data are fit to a single exponential function. The seed concentration is 7% of the total $A\beta_{1\text{-}40}$ concentration.

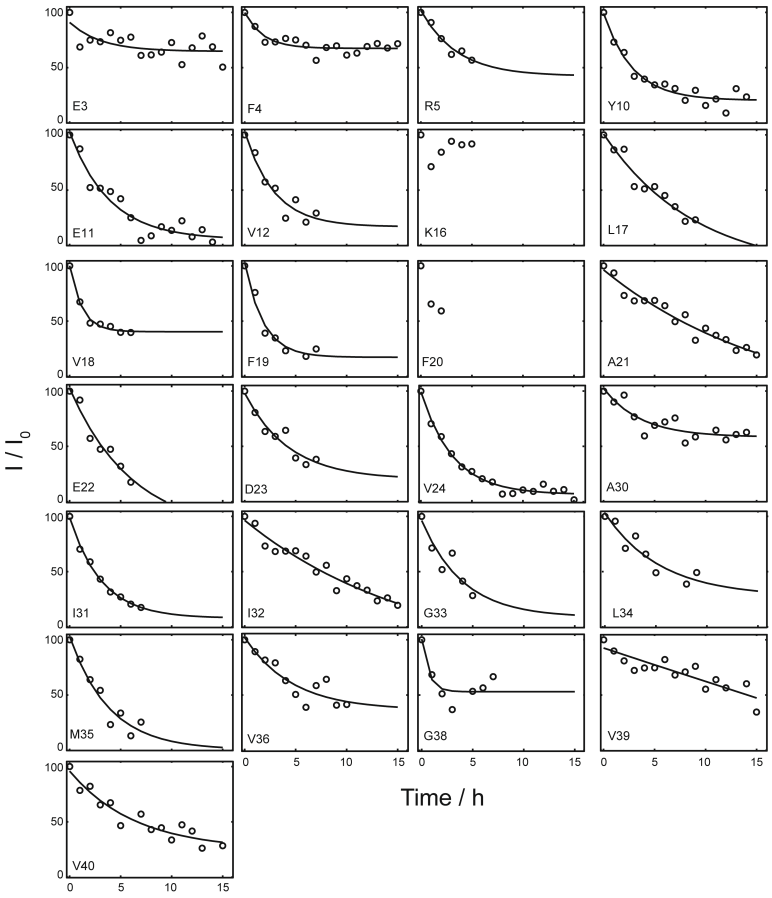

Figure C.3 Time-course intensity changes of HSQC peaks of a seeded $A\beta_{1\text{-}40}$ sample at 25 ºC.
All data are to a single exponential function. The seed concentration is 7% of the total Aβ40 concentration.

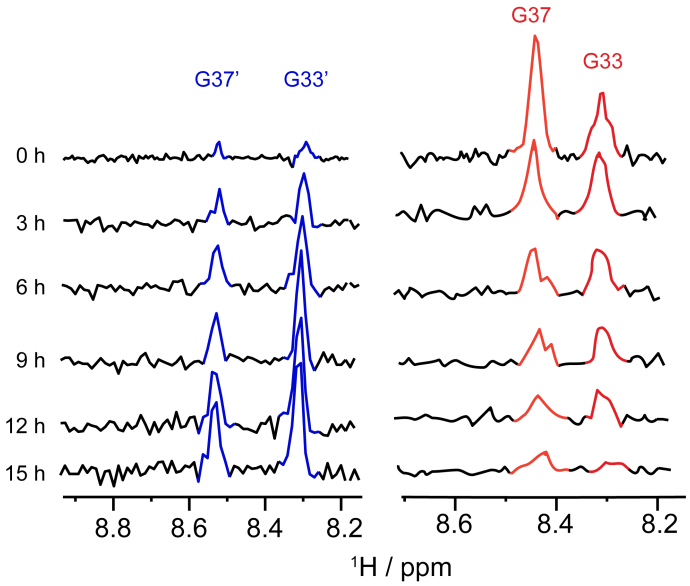

Figure C.4 One-dimensional ^{1}H slices taken from the glycine region of the real-time HSQC measurements.
The corresponding decay and build-up these HSQC peaks strongly suggests that the new peaks come from residues G33 and G37.

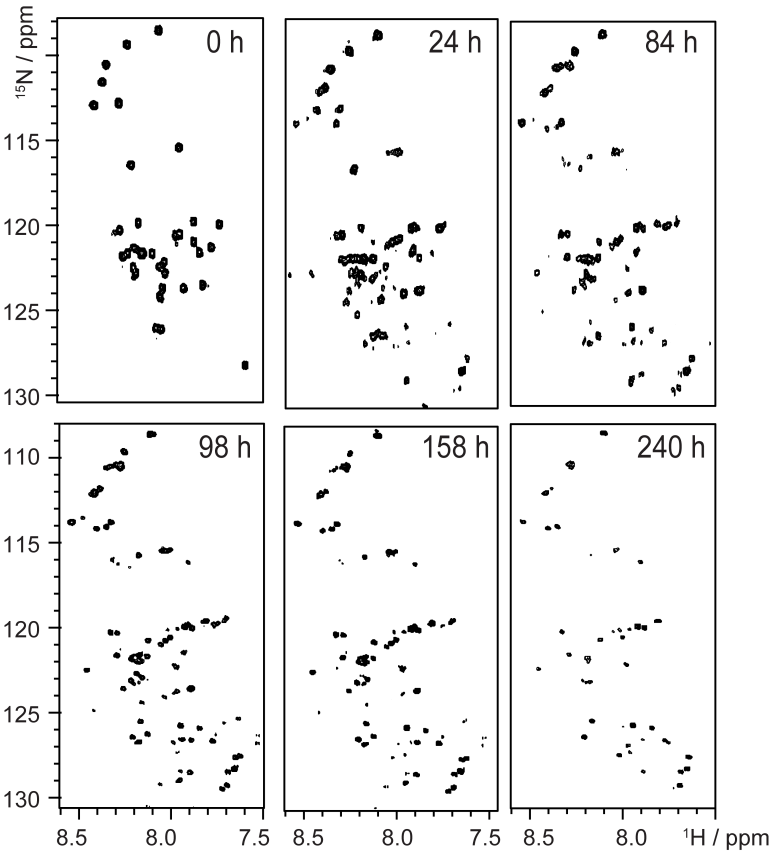

Figure C.5 Real-time HSQC experiments over an extended time period show that the most of the $A\beta_{1\text{-}40}$ monomer is pushed towards a fibril-bound state.
This is evidenced by the fact that almost all HSQC peaks end are distinct from that of the monomer at 0 hrs. The concentration of fiber seed was increased up to 30% of the total Aβ40 concentration. All experiments were acquired at 10 ºC.

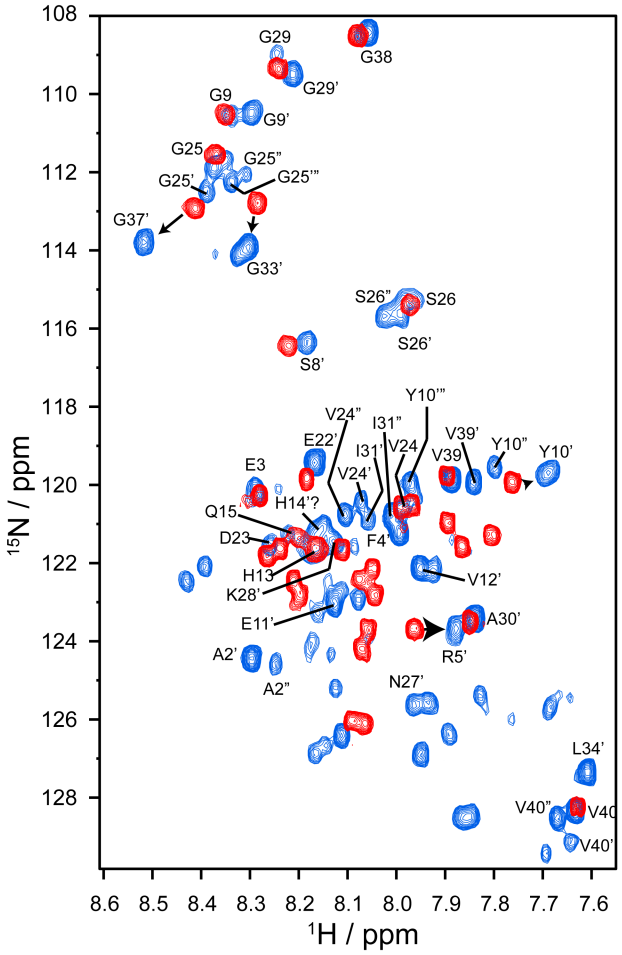

Figure C.6 Assigned ^{1}H-^{15}N HSQC spectrum of the seeded $A\beta_{1-40}$ sample at a late stage of the aggregation process.
3D HNCA and HN(CA)CB spectra were acquired on a 800 MHz spectrometer at 10 ºC. A partial assignment was possible of the new peaks arising from the slow exchange of fibril with monomer. New peaks are indicacted with a prime or double prime.

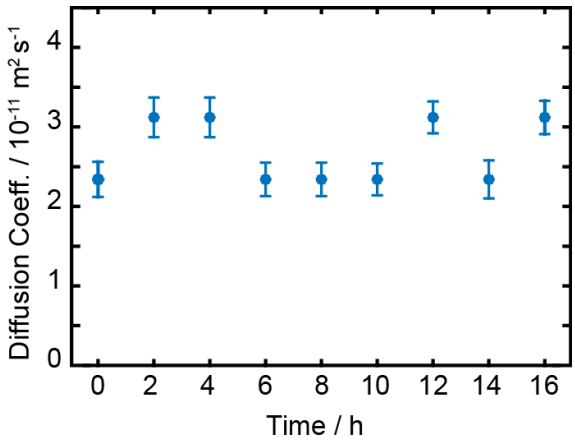

Figure C.7 Time-course Diffusion Order SpectroscopY (DOSY) experiments performed on $A\beta_{1-40}$ in the presence of a 10% fiber seed.
The insignificant change in diffusion coefficient over the course of 15 hrs demonstrates that no new oligomer species forms in the presence the fiber seed, pointing to monomeric $A\beta_{1-40}$ interacting with the fibers directly.

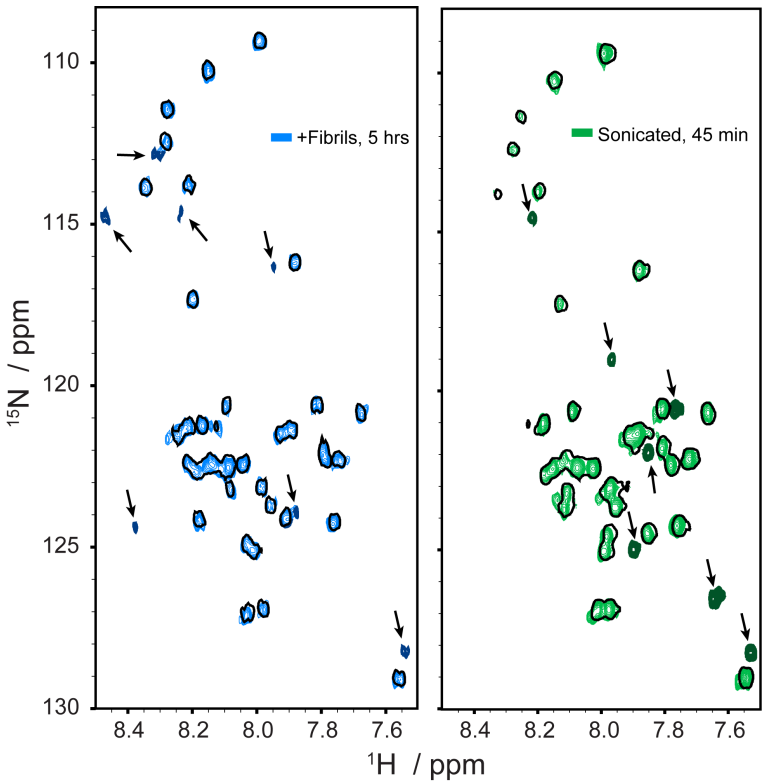

Figure C.8 Sonication accelerates the formation of new peaks arising from the slow exchange between free and fiber-bound forms of monomeric $A\beta_{1\text{-}40}$.
In samples that were not subjected to sonication following addition of a 10% fiber seed (Left panel), new peaks typically took 3-5 hours to appear in ^{1}H-^{15}N HSQC spectra (blue spectrum). Conversely, in samples that were subjected to sonication, new peaks appeared after 45 min (green spectrum, right). Sonication serves to break up fibers and increase the total surface area of accessible fiber ends, suggesting that new peaks arise from monomeric $A\beta_{1\text{-}40}$ binding at the exposed fiber ends. In both panels, spectra before addition of fiber seeds are represented as single black contour lines.

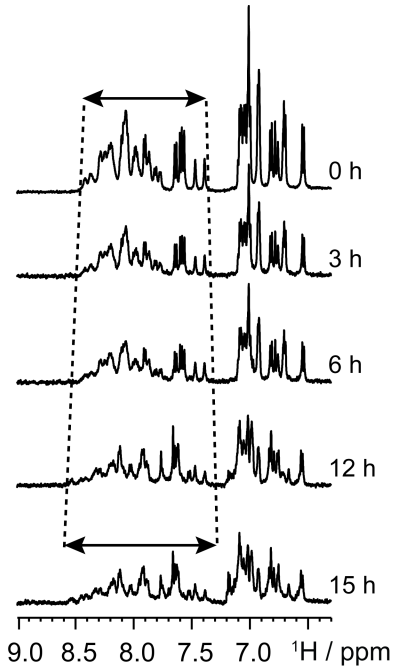

Figure C.9 Time-course 1D ^{1}H spectra of seeded A$\beta_{1\text{-}40}$ aggregation.
Increasing spectral dispersion of the amide region in the 1D ^{1}H spectra points the visible A$\beta_{1\text{-}40}$ species taking on secondary structure. Additionally, the line broadening suggests the A$\beta_{1\text{-}40}$ monomer is in chemical exchange with the fibrillar A$\beta_{1\text{-}40}$ species.

1. Vivekanandan, S., Brender, J. R., Lee, S. Y., and Ramamoorthy, A. (2011) A partially folded structure of amyloid-beta(1-40) in an aqueous environment. *Biochem. Biophys. Res. Commun.* **411**, 312–6

2. Kotler, S. A., Brender, J. R., Vivekanandan, S., Suzuki, Y., Yamamoto, K., Monette, M., Krishnamoorthy, J., Walsh, P., Cauble, M., Holl, M. M. B., Marsh, E. N. G., and Ramamoorthy, A. (2015) High-resolution NMR characterization of low abundance oligomers of amyloid-β without purification. *Sci. Rep.* **5**, 11811

3. Fawzi, N. L., Ying, J., Ghirlando, R., Torchia, D. A., and Clore, G. M. (2011) Atomic-resolution dynamics on the surface of amyloid-β protofibrils probed by solution NMR. *Nature*. **480**, 268–272

4. Tanner, J. E. (1970) Use of the Stimulated Echo in NMR Diffusion Studies. *J. Chem. Phys.* **52**, 2523

5. Stejskal, E. O., and Tanner, J. E. (1965) Spin Diffusion Measurements: Spin Echoes in the Presence of a Time-Dependent Field Gradient. *J. Chem. Phys.* **42**, 288